ABSTRACT

Title of Dissertation: DEVELOPMENT OF A GENERAL-PURPOSE STEADY-STATE SIMULATION FRAMEWORK FOR VAPOR COMPRESSION SYSTEMS

Ransisi Huang
Doctor of Philosophy, 2020

Dissertation directed by: Reinhard Radermacher, Professor
Department of Mechanical Engineering

The vapor compression system is the dominating technology in heat pumping, air conditioning and refrigeration. Vapor compression is associated with significant energy consumption and high global warming potential. Steady-state simulation of vapor compression system is a crucial numerical technology that helps to assess and mitigate the energy and environmental impact of these systems. This dissertation aims to advance the steady-state modeling and simulation technologies for vapor compression systems toward higher level of flexibility, computational efficiency, and robustness, improving designs and reducing time to market.

First, the dissertation proposes a generalized solution methodology for the steady-state analysis of arbitrary systems. A tripartite-graph based tearing algorithm is proposed to generically formulate the residual equations. The methodology was extensively validated by five test systems with capacities from 10 to 100 kW. The maximum

simulation energy imbalance was 0.91%, and the maximum system performance deviation was 8.94%. The methodology was also applied to analyze two advanced vapor compression systems, presenting strong capability to contribute to the acceleration of their R&D stage.

Second, the dissertation develops an approximation-assisted modeling methodology to speed up the steady-state system simulation. Three approximation-assisted heat exchanger models were compared in terms of accuracy and computational efficiency. Kriging metamodel presented the highest accuracy among the three. For heat exchanger performance approximation, its overall ΔP and Δh mean absolute error (MAE) were 4.46% and 0.9%, respectively. For system simulations, the maximum COP and capacity errors with Kriging metamodel were 2.54% and 1.45%, respectively. System simulation was sped up by 10X - 600X, depending on the test conditions.

Third, the dissertation proposes two convergence improvement approaches on the basis of nonlinear equation fundamentals, and assessed them on a standard vapor compression system as a first step, allowing for later application to more complex cycles. The assessment results show that the initial point with large Jacobian condition number presented low convergence probability. The results also indicate a correlation between component nonlinearity and simulation convergence. It was found that by changing the characterization methods in the heat exchanger models, 47 out of 51 originally non-converged cases were able to reach convergence.

DEVELOPMENT OF A GENERAL-PURPOSE STEADY-STATE SIMULATION FRAMEWORK FOR VAPOR COMPRESSION SYSTEMS

by

Ransisi Huang

Dissertation submitted to the Faculty of the Graduate School of the
University of Maryland, College Park, in partial fulfillment
of the requirements for the degree of
Doctor of Philosophy
2020

Advisory Committee:
Professor Reinhard Radermacher, Chair
Associate Professor Jacob Bedrossian, Dean's Representative
Associate Professor Katrina Groth
Professor Jungho Kim
Professor Jelena Srebric
Research Scientist Vikrant Aute

Dedication

To my parents,

Thank you for raising me up to more than I can be.

Acknowledgements

I would like to express my sincere gratitude to my supervisor, Dr. Reinhard Radermacher, for providing me the opportunity to learn, work and research in a leading research center. I would also like to offer my earnest gratitude to my research advisor, Dr. Vikrant Aute. His professionalism and technical rigorousness, his expertise on a variety of domains, especially simulation, software architecture and applied mathematics, have been an unfailing source of guidance and support, without which this work could hardly have been completed. I owe my deep gratitude to my other committee members: Dr. Jacob Bedrossian, Dr. Katrina Groth, Dr. Jungho Kim, and Dr. Jelena Srebric, who have shared their valuable time and advice to support my doctoral training.

I am genuinely grateful to Dr. Jiazhen Ling, for his willingness to participate in countless discussions with me that have shaped up ideas and paths forward. His hunger for knowledge, broad spectrum of knowledge, and conscientious working attitude have influenced me in a variety of aspects. My appreciation also goes to Dr. Yunho Hwang, for his beneficial comments in the CEEE meetings and numerous dryruns. A special thank-you note goes to the CEEE sponsors for their feedback that honed my presentation skills in the consortium meetings.

I would like to thank Dr. Zhenning Li for being a reliable colleague/friend who has offered me generous help, especially during my start-up on C#, VapCyc, among other MOC-related skills. I also thank Dongyu Chen and Dr. Yiyuan Qiao for their hospitality, as proven by the numerous hot-pot and game nights they have hosted. Other colleagues/friends who have helped and supported me along the journey are: Dr. Mohamed Beshr, Dr. Daniel Bacellar, Dr. Rohit Dhumane, James (Jimmy) Tancabel,

Lingzhe Wang, Dr. Arne Speerforck, Jan Schwidtal, Dr. Roberta Mancini, Lukas Rominger, Tanjebul Alam, Lalith Dharmalingam, Rajath Subbappa, Mary Baugher, Nicole Kirkner, among all the CEEE faculties, students, and alumni who have created an intellectual and motivating atmosphere throughout my graduate life. I also extend my gratitude to Xue Song, Shaoli Lin and my previous roommates, with whom I have enjoyed my days in the lives of Maryland.

My greatest and deepest gratefulness goes to my parents and my family. Three of my four grandparents passed away while I was pursuing my studies, but their love is eternal. What I have achieved today would never have been possible without the unconditioned love and encouragement from my family.

Table of Contents

List of Tables

List of Figures

Nomenclature

Acronyms

AA	Approximation-assisted
CHX	Coaxial heat exchanger
COP	Coefficient of performance
CHK	Check valve
EWT	Entering water temperature
EXV	Expansion valve
GWP	Global warming potential
HVAC&R	Heating, ventilation, air-conditioning and refrigeration
HX	Heat exchanger
HTC	Heat transfer coefficient
LWT	Leaving water temperature
MAE	Mean absolute error
MAX	Maximum absolute error
OC	Outdoor coil
PHX	Plate heat exchanger
RH	Relative humidity
RPM	Round per minute
SC	Subcooling
SDT	Saturated discharge temperature
SH	Superheat
SHR	Sensible heat ratio
SIT	Saturated injection temperature
SST	Saturated suction temperature
TFHX	Tube-fin heat exchanger
VC	Vapor compression
VRF	Variable refrigerant flow

English letters

D	Input domain for heat exchanger approximation

h	Enthalpy
h_{lv}	Evaporation heat
L	Length
J	Jacobian matrix
$\dot{m}$ /mfr	Mass flow rate
$\tilde{\dot{m}}$	Dummy mass flow rate
P	Pressure
Q	Capacity
R	Result library for heat exchanger approximation
s	Entropy
S	Sample library for heat exchanger approximation
T	Temperature
U	Overall heat transfer coefficient
vap%	Vapor coil percentage
$\dot{V}$	Volumetric flow rate
w	Natural neighbor weight
W	Power consumption
x	quality
X	Input state

Greek letters

κ	Condition number
δ	Error or deviation
ω	Humidity ratio
Δ_E	Simulation energy imbalance
Δh	Enthalpy change
ΔP	Pressure drop
ΔT	Temperature difference

Subscripts

amb	ambient

c	Condenser
comp	Compressor
db	Dry-bulb
dis, dew	Discharge dew point
e	Evaporator
eco	Economizer
in	Inlet
l	Lower bound
liq	Liquid
o/out	Outlet
ref	Refrigerant
sat	Saturation
sec	Secondary fluid
suc, dew	Suction dew point
tp	Two phase
u	Upper bound
valv	Expansion valve
vap	Vapor phase
wb	Wet-bulb
x,y	Component ID, port ID
x,y,z	Component ID, fluid group ID, port ID

1. Introduction

1.1. Background and motivation

A vapor compression (VC) system (Figure 1.1) is used to pump heat from a space at lower temperature to a space at higher temperature. This technology is widely used in heating, ventilation, air-conditioning and refrigeration (HVAC&R) systems for applications such as space temperature control for human comfort, food storage among other purposes. These heat pumping processes consume a significant amount of the primary energy and are associated with high global warming potential (GWP). According to the latest residential and commercial building energy consumption surveys by U.S. Energy Information Administration [1, 2], heating, cooling, ventilation and refrigeration account for 54% of the energy use in commercial buildings, and 55% in residual buildings.

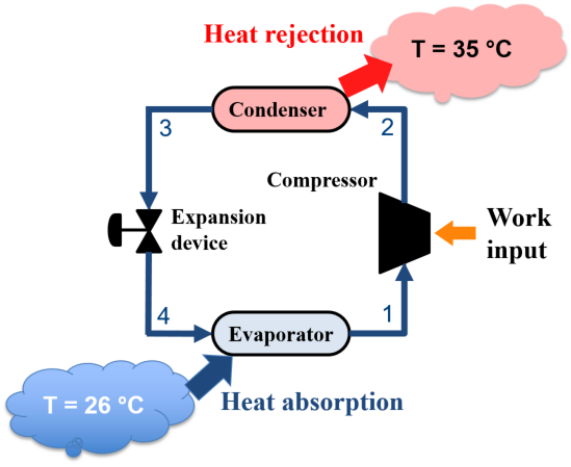

Figure 1.1 Standard vapor compression system

In 2015, the Paris Agreement [3] set out a global framework to limit global warming to below 2 °C. Therefore, reducing the energy consumption and the global warming impact of these vapor compression systems is of utmost concern. This may be achieved

through the following options: (i) improved components such as novel compressors or novel heat exchangers, (ii) advanced system configurations such as two-stage systems, (iii) advanced control such as the use of variable speed drives, and (iv) the use of environmentally friendly refrigerants such as lower-GWP refrigerants and/or natural refrigerants. Assessing the efficacy and the environmental impact associated with these options requires a robust modeling framework capable of simulation and optimization of these systems/components.

Steady-state VC system simulation is a crucial and efficient numerical analysis tool that provides details regarding the system performance at a set of design points as well as at off-design conditions [4]. It is used by HVAC&R engineers and researchers for early concept verification, component/system design optimization, and system performance rating. It can save time and cost from the otherwise more expensive experiments, and also help identify the most effective opportunities for improving the energy and environmental performance of the system. Therefore, reliable steady-state VC system simulation technologies is a critical infrastructure of HVAC&R industry and research community.

1.2. Literature review of steady-state simulation of vapor compression systems

1.2.1. Modeling and representation approaches of the components

In the steady-state VC system simulation, the heat exchanger (HX), compressor, and expansion valve are usually considered as the primary components, while the auxiliary components include the pipe, flash tank, and so on. Generally, there are three approaches to model or represent the component performance for a given set of geometric and

operating conditions: physics-based approach, black box (or data-driven) approach and hybrid approach.

The physics-based approach requires detailed geometric information of the component, and simulates the component performance based on thermodynamic laws and fundamental heat and mass transfer relations. An example is the finite-volume HX model [5, 6, 7], in which the HX is divided into finite number of control volumes (or segments). This approach can be very accurate and offers best insight into the HX component behavior, but meanwhile can be time-consuming.

The black-box approach approximates the component performance by formulating an input-output relation using simulation or test data. Certain mathematical techniques are required to obtain such a relation, such as artificial neural networks (ANN) and statistical regression. For example, Li *et al.* [8] proposed a response surface methodology based neural network approach for condenser performance representation. Another example of the black-box approach is the 10-coefficient compressor polynomial model [9]. The compressor performance, such as mass flow rate and power, are directly mapped to the dew point and suction point saturation temperatures, based on either superheat or return gas temperature. The regression coefficients are usually provided by respective compressor manufacturers. The black-box approach has low computational cost but offers no underlying physical insights. In addition, by definition, it cannot be used for extrapolation.

The hybrid approach takes advantage of the previous methods by grouping the physical and geometric information of the component into characteristic parameters, which are determined empirically based on a training data set. Ding *et al*. [10] proposed

a hybrid evaporator model in which the model parameters are approximated by linear and nonlinear least-squares method. The efficiency-based compressor model also falls into the hybrid approach. It is based on the first law of thermodynamics. The irreversibility associated with the compression process and imperfection induced by the manufacturing processes are characterized by isentropic efficiency, volumetric efficiency and mechanical efficiency. These efficiencies can be given by fixed values or operating condition-dependent equations.

In summary, the three approaches offer unique tradeoffs among computational cost, accuracy, and the degree of physical insight. There is no one-cut rule or criterion regarding the selection of these component modeling approaches in the steady-state simulation of vapor compression systems. The selection is usually based on the priority and judgment of the engineers or researchers undertaking the system simulation.

1.2.2.System solution technique overview

The goal of the modeling of vapor compression systems, in a mathematical perspective, is to solve unknown variables based on a set of equations. The unknown variables in the steady-state vapor compression system simulation are usually fluid-related thermodynamic states [11]. We then rely on a process that adjusts these variables until all the mass, momentum and energy balance equations and the design criteria are satisfied. This process is called the solution technique (or solution scheme). Generally, there are two types of the solution techniques in the open literature [4]: 1) successive approach, 2) simultaneous approach.

The successive approach involves an iteration procedure of multiple nested loops where one system variable is iterated to convergence before moving on to the next. The

iteration convergence criteria could be: i) system design parameters, such as condenser outlet subcooling, suction superheat, and system charge; ii) system balance resulting from the fact that the thermodynamic cycle of the system is a closed loop.

Domanski & Didion [12], and Fischer & Rice [13] were among the first to propose the successive approach. Figure 1.2 shows Domanski & Didion's scheme. The high side pressure was first adjusted to find the value with which the mass flow balance would exist, and then the low side pressure was adjusted until the enthalpy balance was satisfied between the evaporator inlet and condenser outlet. Lastly, the system mass balance was checked, otherwise, the superheat value was adjusted and the whole calculation was repeated from the beginning. Figure 1.3 shows Fischer & Rice's calculation procedure, which was organized into the high side section and low side section. The high-side section iterated on the condensing temperature. The convergence criterion was either specified subcooling or the system mass flow balance, depending on whether the expansion device was specified. The low-side section iterated on the evaporating temperature and the convergence criterion was specified superheat.

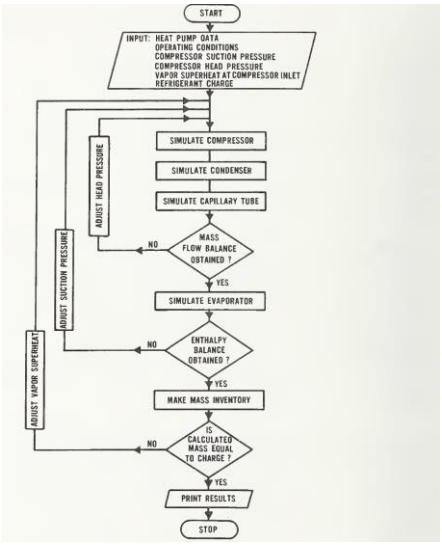

Figure 1.2 Domanski & Didion's successive scheme for simulating VC systems [12]

In the successive approach, there is a clear relation between each variable and convergence criterion. Thus, this approach has obvious physical meaning and good calculation stability [14]. However, this approach has arelatively low calculation speed due to the presence of multiple iteration layers. It also offers low flexibility because it requires customized iteration procedure for different system configurations.

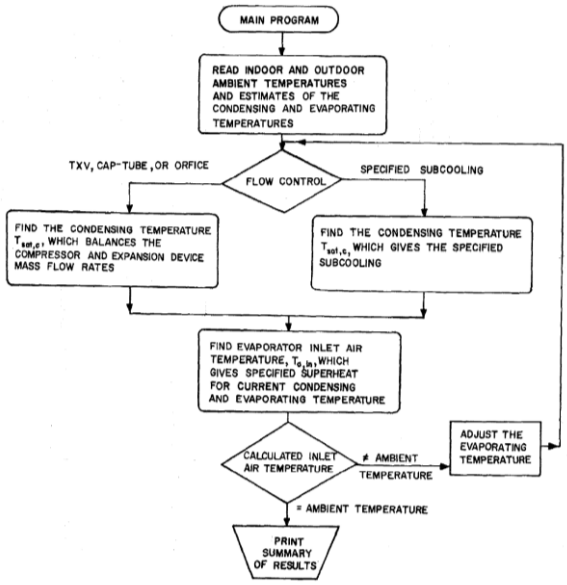

Figure 1.3 Fischer & Rice's successive scheme for simulating VC systems [13]

Over the last three decades, this approach has been adapted to different applications including transcritical CO_2 heat pump, geothermal heat pump, heat pump with desuperheater, two-stage heat pump and variable refrigerant flow system. Table 1.1 shows a summary of VC system simulations in which the successive approach was applied. As can be seen, most of the application were confined to the simple four-component configuration.

Table 1.1 Summary of VC system simulation work based on the successive approach

Researchers, year	**System layout**	**Convergence criteria**
Fischer & Rice, 1983 [13]	Air-to-air heat pump	- Specified subcooling or balance between compressor and expansion device mass flow rates (Referred as mass flow balance for the rest of the table) - Specified superheat
Domanski & Didion, 1983 [12]	Air-to-air heat pump with a capillary tube	- Mass flow balance - Enthalpy balance: $h_{cond,o} = h_{evap,in}$ - Specified system charge
Domanski & McLinden, 1992 [15]	Theoretical cycle and household refrigerator cycle	- Specified effective temperature differences of the HXs - Specified suction temperature
De Lemos & Zaparoli, 1996 [16]	Household refrigerator cycle	- Mass flow balance - System energy balance - Specified system charge
Browne & Bansal, 1998 [17]	Centrifugal liquid chiller	- Specified subcooling and superheat - Balance between initial and calculated refrigeration capacity - Cycle energy balance
Robinson & Groll, 2000 [18]	Air-to-air CO2 based air conditioning device	- Specified superheat - Specified system capacity
Jin & Spitler, 2002 [19]	Water-to-water heat pump	- Balance between initial and calculated HX capacities

Researchers, year	System layout	Convergence criteria
Zhao et al. 2003 [20]	Geothermal heat pump	- Mass flow balance - Temperature balance: $T_{evap,in} = T_{valve,o}$ - Specified system charge
Sarkar et al. 2006 [21]	Trans-critical CO2 heat pump	- Specified superheat - Specified gas cooler outlet temperature
Blanco et al. 2012 [22]	Water-to-water heat pump with a desuperheater	- Specified system charge - Balance between the initial and calculated suction states
Heo et al. 2012 [23]	Two-stage flash tank cycle	- Mass flow balance - Balance between initial and calculated evaporator outlet pressure - Balance between initial and calculated evaporator outlet enthalpy
Santa & Garbai 2015 [24]	Water-to-water heat pump	- Mass flow balance - Enthalpy balance: $h_{cond,o} = h_{evap,in}$
Zsembinszki et al. 2016 [25]	Simple four-component cycle	- Specified subcooling - Specified superheat
Sun et al. 2017 [26]	VRF multi-split systems	- High side mass balance - Low side mass balance - Mass flow balance - Specified superheat

The simultaneous approach involves formulating a system of coupled nonlinear equations that represent the steady state of the system. As opposed to the successive approach, which finds the solutions in a sequential manner, this approach resorts to numerical convergence techniques such as the multi-variable nonlinear equation solver or the non-linear optimization procedure to simultaneously iterate and solve for multiple variables. By doing so, the simultaneous approach is inherently more flexible than the successive approach in response to the change in system configurations. Table 1.2 shows a summary of simulation work that was based on the simultaneous approach, which, as

opposed to the successive approach, were not confined to the simple four-component configuration.

Typical examples of the simultaneous approach are the junction solver by Richardson [27] and the fluid network model developed by Shao et al. [28]. The fluid network model applies node-branch matrix to systematically describe the inter-component connections, so that it could deal with complex systems that have multiple condensers and evaporators with uncertainty of the refrigerant flow direction. The junction solver used Junction Component Port matrix to describe the component connectivity. It assumes the pressure and enthalpy at each junction as unknown variables, and uses junction mass flow balance and junction energy balance to form the system conservation equations.

The drawback of the simultaneous approach is a large number of unknown variables, and thus it presents challenge for the convergence techniques, especially when the configuration gets complicated.

Table 1.2 Summary of VC system simulation work based on the simultaneous approach

Solution technique	**Capability**	**Unknown variables**	**Residual equations**	**Global convergence technique**
Herbas et al. 1993 [29]	Simple VC cycle	T_{dis} T_{cond} T_{evap}	Three non-linear equations derived from 27 equations	Newton-Raphson method
Rossi, 1997 (ACMODEL) [30]	Simple VC cycle	P_{suc} h_{suc} P_{dis}	Specified system charge Pressure balance Enthalpy balance	Modified Newton's method
Hwang & Radermacher, 1998 [31]	Transcritical CO2 cycle	P_{evap} P_{cond} T_{water} at evaporator inlet T_{water} at gas cooler outlet	Refrigerant- and water-side capacity balance HX area balance between calculated and given values	Newton-Raphson method
Corberan et al. 2000 [32]	Simple VC cycle	P and h in each inlet and outlet point	Balance between component equations Specified system charge or subcooling	Powell's Hybrid method
Richardson, 2006 (Junction Solver) [27]	Simple cycle, suction line HX	P at each junction h at each junction	Junction mass flow balance Junction energy balance Specified system charge	Newton-Raphson or Broyden method
Shao et al. 2008 (Fluid Network Model) [28]	Systems with several condensers and evaporators;	P at each node h at each node	Node mass balance Node energy balance Loop pressure balance	Newton-SOR

Solution technique	**Capability**	**Unknown variables**	**Residual equations**	**Global convergence technique**
	Uncertainty of refrigerant flow	Relative mass flow rate of each branch	System mass balance	
Winkler, 2009 (Enthalpy Marching Solver) [33]	Simple cycle, cascade cycle, two-stage flash tank cycle	Formulated distinctly based on system layout	Formulated distinctly based on system layout	Newton-Raphson method Broyden method Hybrid method
Beshr et al. 2016 (Multi Fluid Solver) [34]	Simple cycle, cascade cycle, multi-fluid cycle	Formulated based on system layout	Formulated based on system layout	Newton-Raphson method Broyden method Hybrid method
Ruz et al. 2017 [35]	Simple VC cycle	System operating points and component operating parameters	Eight component interaction equations	Interior-point nonlinear optimization method

1.2.3.Steady-state analysis of complex systems

1.2.3.1.Variable refrigerant flow systems

Variable Refrigerant Flow (VRF) system is a widely applied air conditioning technology for residential or commercial buildings. It has independent units that distribute cooling and heating capacities to separate rooms. Compared to the traditional air conditioning systems, VRF system presents high level of flexibility and high COP in part load conditions.

Shao et al. 2008 [28] developed a two-phase fluid network model to describe refrigeration and heat pump systems with several condensers and evaporators in the structure of Figure 1.4. Figure 1.5 shows the node-branch incidence matrix that represents the connections in such systems. The unknown variables were state vectors that included the node enthalpy, node pressure, and the relative mass flow rate of each branch. The nonlinear equations were the energy and mass conservation at each node, pressure balance of each loop, and system-level mass conservation. By using the concept of factual and fictitious branches, this model was able to simulate VRF system in different operating modes.

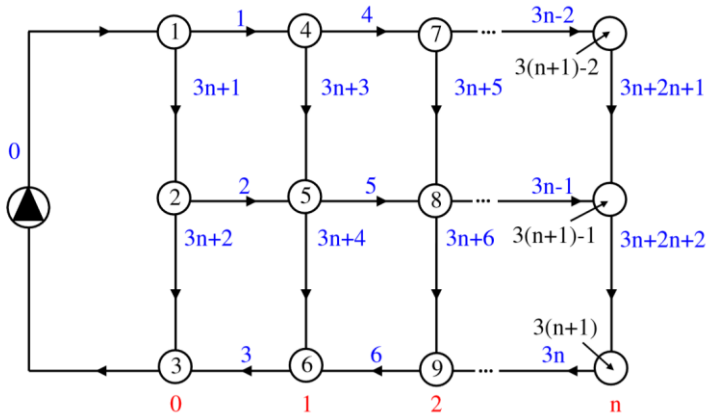

Figure 1.4 Two-phase fluid network model of a refrigeration and heat pump system [28]

$$\mathbf{A} = \begin{bmatrix} -1 & 1 & 0 & 0 & \dots & a_{1,j} & \dots & 0 \\ 0 & 0 & 1 & 0 & \dots & a_{2,j} & \dots & 0 \\ 1 & 0 & 0 & -1 & \dots & a_{3,j} & \dots & 0 \\ 0 & -1 & 0 & 0 & \dots & a_{4,j} & \dots & 0 \\ \vdots & \vdots & \vdots & \vdots & \ddots & \vdots & \vdots & \vdots \\ a_{i,0} & a_{i,1} & a_{i,2} & a_{i,3} & \dots & a_{i,j} & \dots & a_{i,N_B} \\ \vdots & \vdots & \vdots & \vdots & \vdots & \vdots & \ddots & \vdots \\ 0 & 0 & 0 & 0 & \dots & a_{N_N,j} & \dots & -1 \end{bmatrix},$$

where

$$a_{i,j} = \begin{cases} 1 & \text{node i is inlet of branch j;} \\ -1 & \text{node i is outlet of branch j;} \\ 0 & \text{else.} \end{cases}$$

Figure 1.5 Node-branch incidence matrix proposed for two-phase fluid network model [28]

Sun et al. [26] argued that the node-branch incidence matrix developed by Shao et al. [28] would need to be rebuilt when the system operating condition was changed. And they proposed a more general model based on graph theory description method for VRF multi-split systems (Figure 1.6). They employed adjacency matrices (Figure 1.7) to represent the system directed graph, and used the diagonal matrix (Figure 1.7) to describe the operating number of the indoor units. Figure 1.8 shows the adjacency matrixes representing the VRF system in cooling mode and heating mode, which are simply the transpose of each other. By multiplying the adjacent matrix and the diagonal matrix, the general description matrix of VRF systems could be obtained with any number of indoor units under various operating conditions. However, the authors did not demonstrate how to extend this approach to other systems.

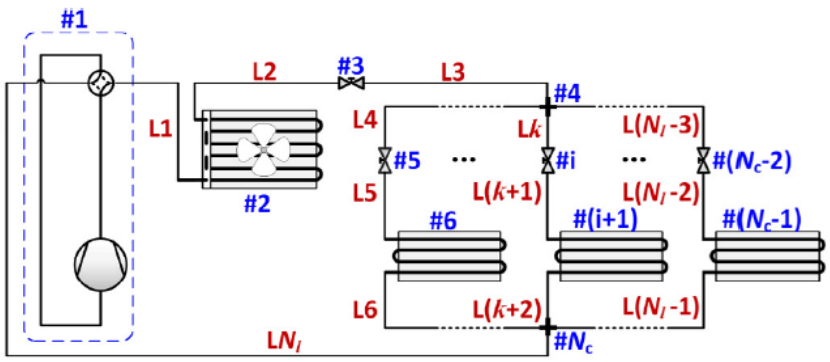

Figure 1.6 Simplified diagram of a VRF system [26]

$$c_{i,j}=\begin{cases} k & \text{when No. \# } i \text{ is connected to No. \# } j \text{ by line} \\ 0 & \text{else} \end{cases}$$

$$N=\mathrm{diag}(n_1, n_2, n_3 \cdots n_i, n_{i+1} \cdots n_{N_c-2}, n_{N_c-1}, n_{N_c})$$

$$\begin{cases} n_i = 1 & \text{for operating component} \\ n_i = 0 & \text{for non-operating component} \end{cases}$$

Figure 1.7 Adjacency matrix (left) and diagonal matrix (right) developed by Sun et al. [26]

$$C=\begin{array}{c} \begin{matrix} Vj & \#1 & \#2 & \#3 & \#4 & \cdots & \#i & \#i+1 & \cdots & \#N_c-2 & \#N_c-1 & \#N_c & Vi \end{matrix} \\ \begin{bmatrix} 0 & 1 & 0 & 0 & & 0 & 0 & & 0 & 0 & 0 & \#1 \\ 0 & 0 & 2 & 0 & & 0 & 0 & & 0 & 0 & 0 & \#2 \\ 0 & 0 & 0 & 3 & & 0 & 0 & & 0 & 0 & 0 & \#3 \\ 0 & 0 & 0 & 0 & & k & 0 & & N_l-3 & 0 & 0 & \#4 \\ & & & & & & \cdots & & & & & \cdots \\ 0 & 0 & 0 & 0 & \vdots & 0 & k+1 & \vdots & 0 & 0 & 0 & \#i \\ 0 & 0 & 0 & 0 & & 0 & 0 & & 0 & 0 & k+2 & \#i+1 \\ & & & & & & \cdots & & & & & \cdots \\ 0 & 0 & 0 & 0 & & 0 & 0 & & 0 & N_l-2 & 0 & \#N_c-2 \\ 0 & 0 & 0 & 0 & & 0 & 0 & & 0 & 0 & N_l-1 & \#N_c-1 \\ N_l & 0 & 0 & 0 & & 0 & 0 & & 0 & 0 & 0 & \#N_c \end{bmatrix} \end{array}$$

$$H=C^T=\begin{array}{c} \begin{matrix} Vj & \#1 & \#2 & \#3 & \#4 & \cdots & \#i & \#i+1 & \cdots & \#N_c-2 & \#N_c-1 & \#N_c & Vi \end{matrix} \\ \begin{bmatrix} 0 & 0 & 0 & 0 & & 0 & 0 & & 0 & 0 & N_l & \#1 \\ 1 & 0 & 0 & 0 & & 0 & 0 & & 0 & 0 & 0 & \#2 \\ 0 & 2 & 0 & 0 & & 0 & 0 & & 0 & 0 & 0 & \#3 \\ 0 & 0 & 3 & 0 & & 0 & 0 & & 0 & 0 & 0 & \#4 \\ & & & & & & \cdots & & & & & \cdots \\ 0 & 0 & 0 & k & \vdots & 0 & 0 & \vdots & 0 & 0 & 0 & \#i \\ 0 & 0 & 0 & 0 & & k+1 & 0 & & 0 & 0 & 0 & \#i+ \\ & & & & & & \cdots & & & & & \cdots \\ 0 & 0 & 0 & N_l-3 & & 0 & 0 & & 0 & 0 & 0 & \#N_c- \\ 0 & 0 & 0 & 0 & & 0 & 0 & & N_l-2 & 0 & 0 & \#N_c- \\ 0 & 0 & 0 & 0 & & 0 & k+2 & & 0 & N_l-1 & 0 & \#N \end{bmatrix} \end{array}$$

Figure 1.8 Adjacency matrixes for a VRF system in cooling (left) and heating mode (right) [26]

1.2.3.2. Two-stage compression systems

Two-stage compression system is one of the most effective approaches to improve the performance of air source heat pump under low ambient temperature [36]. It has demonstrated reliable and improved performance when the temperature difference between the heat sink and heat source are high. These systems may employ various

intermediate configurations, such as liquid injection (or direct injection), flash tank vapor injection, economizer vapor injection, ejector injection, etc.

Torrella et al. [37] proposed a general analysis methodology that encompasses six configurations of two-stage vapor compression systems. They defined a subcooling parameter and a desuperheating parameter to characterize the subcooling process (refrigerant temperature/enthalpy decrease between the condenser outlet and the evaporator inlet, supposing an isenthalpic expansion process) and desuperheating process (refrigerant temperature/enthalpy decrease between the discharge of the low compression stage and the suction of the high compression stage), respectively. They also established a generic COP expression based on the two parameters.

Adopting the concept of the subcooling parameter from [37], Jiang et al. [38] extended their analysis method to a more general model for two-stage compression systems. Jiang's model applied the concept of an input domain to distinguish different configurations, used a sequential algorithm to obtain the analytical initial solution of the intermediate pressure. In a later publication [39], they applied the general model to investigate the effect of different parameters on the optimum injection pressure.However, Both Torrela and Jiang's approach could only be used for thermodynamic analysis of two-stage systems, with first-order or simplified component models.

1.2.3.3. Component-based method

There has been abundant work [27, 30, 33, 40, 41] dedicated to the component-based (also referred to as modular) approach to simulating heat pump systems. This approach can be extended to handle arbitrary system configurations since the solver only requires the knowledge on how the component models are connected [4]. The ACMODEL

developed by Rossi [30] was one of the early attempts of modular simulation tool for vapor compression system evaluation and design. However, the numerical methods in ACMODEL were limited to basic system configurations only.

Richardson [27] developed a component-based steady-state simulation tool called VapCyc for vapor compression systems, in which the component models and the system solver were distinctly separate modules. The component model predicts the steady state performance of the individual component under given input conditions. The solver formulates the conservation equations based on the system configuration, communicates with the component models, and solves the system conservation equation sets for the steady state system performance. It was in this framework where he developed the junction solver to construct the conservation equations. The junction solver was, as mentioned in section 1.2.2, subjected to low calculation stability, because it had to solve large number of unknown variables (2 per junction).

To overcome this drawback, Winkler et al. [4] developed an enthalpy marching solver in the same component-based simulation framework of VapCyc. It greatly reduced the set of unknown variables and system conservation equations by considering the fact that enthalpies within the cycle are not completely independent. The reduced system equations were called the residual equations. They showed that the enthalpy marching solver was superior to the junction solver in both the calculation stability and efficiency, solving 97% of the test cases [4]. However, while it gained the stability and efficiency, the enthalpy marching solver sacrificed flexibility. The system residual equations had to be distinctly handled for different configurations (e.g. parallel components, suction line HX).

Following the enthalpy marching method, Beshr [34] developed an enhanced system solver. It included a method to formulate the system unknown variables and residual equations, based on the number and type of components, and refrigerant flows split and merge in the system. It kept the number of unknown variables low, and meanwhile offered certain level of flexibility. It could handle systems with multiple air and refrigerant paths. However, the rules cannot be generalized to arbitrary configurations.

There are more software packages that are based on component-based approach in the commercial or public domain, such as IMST-ART [32], CYCLE_D [42], and HPDM [41]. They offer simulation programs that can adapt to various component details, but limited publications can be found about the evolution of numerical solution techniques adopted in these programs. Table 1.3 summarizes and compares the work on component-based simulation.

Table 1.3 Summary of component-based methods and simulation tools for steady-state analysis of VC systems

Source	**Main contribution**	**Limitation**
Ross, [30]	ACMODEL - An early modular simulation tool for system performance evaluation and fault diagnostics	Limited to simple system configurations
Corberan, [32]	IMST-ART - A commercial software for system simulation and design	* Not enough publications to evaluate the limitation
NIST, [42]	CYCLE_D - A public package for system simulation	* Not enough publications to evaluate the limitation
ORNL, [41]	HPDM	* Not enough publications to evaluate the limitation

Source	Main contribution	Limitation
	- A public simulation tool for design and analysis of a wide variety of system configuations	
Richardson, 2006 [27]	Junction solver - Generic construction of residual equations	Low calculation stability - Large number of unknown variables
Winkler, 2009 [33]	Enthalpy marching Solver - Greatly reduced the number of variables	Low flexibility - Distinct equation formulation for different configurations
Beshr, 2016 [34]	Enhanced enthalpy marching solver - Contains a set of rules to formulate system equations	The rules cannot be generalized to arbitrary configurations

Another option of steady-state simulation is conducting the simulation with the objected-oriented equation-based modeling paradigm, such as Dymola [43]. It offers the highest level of flexibility in terms of system configurations and component details. However, the computational cost associated with the dynamic simulation is significant. Also, initialization of the differential and algebraic equations in such paradigm presents a major barrier to the users lacking sufficient insight about the systems they are modeling.

1.3. Summary

The vapor compression (VC) system is the dominating technology in providing cooling or heating for residential, commercial, and industrial applications, and thus has a significant energy and environmental impact. Steady-state VC system simulation is an indispensable technology widely employed by HVAC&R engineers and researchers for system concept verification, component and system design optimization, and system performance rating. The current status of the steady-state VC system simulation is summarized as follows.

a. There are generally three approaches for component modeling and representation: physics-based approach, hybrid approach, and black-box approach. The three approaches present unique tradeoffs among computational cost, accuracy, and the level of physical insight.
b. There are two main categories of system solution techniques: successive and simultaneous approaches. The successive approach lacks flexibility to the system configuration. The simultaneous approach has better flexibility but lacks robustness due to the large number of unknown variables.
c. VC system modeling are still in a configuration-specific manner in the open literature. Researchers develop their own methodologies for particular systems (e.g. VRF system and the two-stage system) in interest based on either successive or simultaneous approach.
d. The current steady-state simulation tools in the commercial and the public domain are all limited to either simple or predefined system configurations. The option of equation-based modeling paradigm allows for high flexibility in system configuration. However, obtaining steady-state solution with such paradigm is time-consuming and requires significant effort by the users.
e. There is very limited research that focuses on the robustness or calculation stability of steady-state VC system simulation. Winkler et al. [4] investigated the stability and speed of three different algorithms, with different convergence criteria. They found that the enthalpy marching solver was the most robust scheme, and that the solution schemes were much more robust when subcooling was specified instead of the charge. However, there still lacks clear understanding on the convergence failure in

the steady-state system simulation, and effective measures for convergence improvement

1.4. Research gaps, objectives, and dissertation organization

Based on the literature review, the current status of the steady-state VC system simulation still presents many research opportunities. Therefore, the overall goal of this dissertation is to advance the steady-state VC system modeling and simulation technologies toward higher level of flexibility, computational efficiency, and robustness. The technique roadmap of the dissertation is summarized in Figure 1.9. As shown, the dissertation consists of the following three objectives.

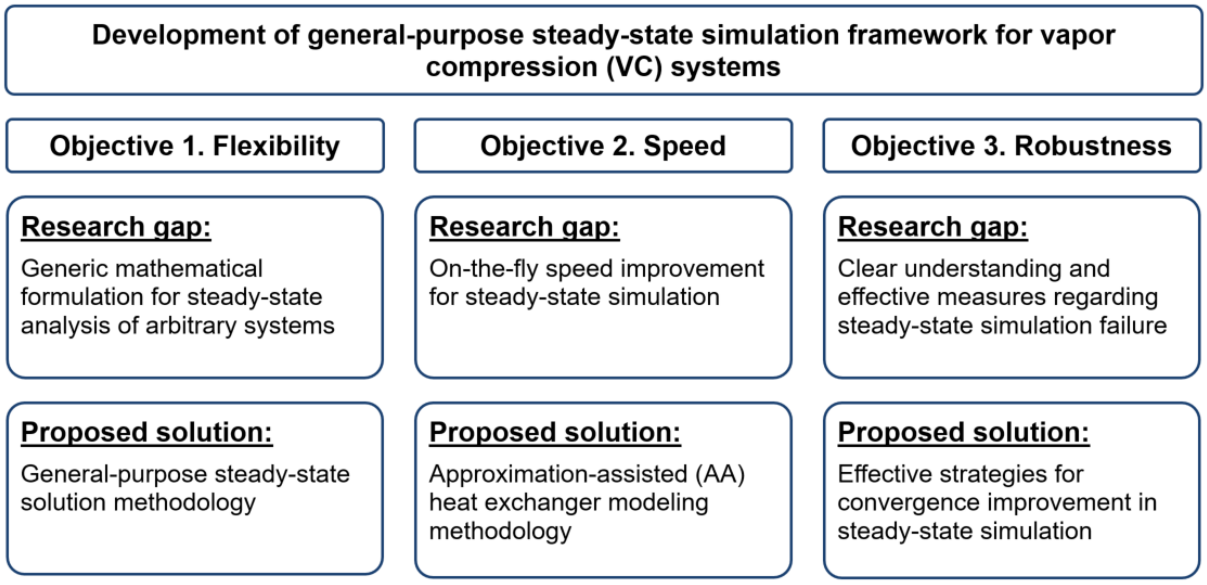

Figure 1.9 Dissertation technical roadmap

1. Flexibility: there is not yet a general-purpose steady-state simulation tool for arbitrary VC systems. Therefore, the first research objective is to develop a generalized representation and solution methodology for steady-state analysis of VC systems with

arbitrary configurations. The solution methodology aims to address the following three critical questions underlying general-purpose steady-state modeling.

- Given a set of component connections, how to systematically determine the system flow directions
- Given the flow directions, how to identify the unknown variables and system of equations
- Given the system of equations, how to deterministically reduce its dimensionality

2. Computational efficiency: there is a lack of effective and on-the-fly speed improvement technique for steady-state VC system simulation. Therefore, the second dissertation objective is to develop an approximation-assisted component modeling methodology. This objective aims to

- Propose and compare different approximation-assisted heat exchanger modeling methods to speed up steady-state system simulation
- Provide quantitative analysis of the proposed approximation methods on the speed improvement and accuracy degradation at both component and the system level

3. Robustness: there lacks sufficient understanding on the convergence failures of steady-state VC system simulation, and there is no relevant measures for convergence improvement. Therefore, the third dissertation objective is to develop effective strategies to improve the steady-state simulation convergence of a standard vapor compression system. This objective aims to

- Propose and assess convergence improvement approaches on the basis of the nonlinear equation fundamentals

- Characterize the numerical behaviors of the primary components and the system, and to understand the factors underlying the convergence failure

In the dissertation, Chapter two describes the structure of the simulation framework, and presents the newly developed representation and solution methodology. Chapter three presents the validation of the methodology for a wide variety of system configurations. Chapter four presents an extended demonstration on advanced vapor compression systems that are still in their early R&D stage. In Chapter five, three approximation-assisted component models were developed, and compared in terms of computational time and accuracy. Chapter six proposed two convergence improvement strategies, and presented the investigation results on the factors that influence the simulation convergence.

2. General-purpose component-based simulation framework

In a component-based simulation environment, there are two main parts: component models and the system solver. The component model predicts the steady-state performance of the individual component under given input conditions. The system solver formulates the system-level conservation equations, communicates with the component models and solves the system-level equation set by numerical methods such as Newton-Raphson and quasi-Newton methods for the steady-state system performance. The component models must implement the component model standard in order to participate in the simulation environment and to communicate with the system solver. The standard, which is a standardized component model template, was first established by Richardson [27], later updated by Beshr [34] to support components that have multiple refrigerant and air paths. The component standard employed in the current framework inherited most of the concepts from the previous standards, and made necessary enrichment to accommodate for a more general-purpose end.

This Chapter starts out with the basic definitions for component-based simulation, followed by a description of the generalized representation approach for the vapor compression systems. Then, a description of the component model standard for the current simulation framework was presented. Last but not the least, three fundamental methods of the general-purpose system solver were outlined: determination of the flow direction map, generic formulation of the system of equations, and the tearing algorithm based on the tripartite graph method.

2.1. Definitions

2.1.1. Port and junction

A port is an inlet or an outlet for a working fluid in a component. In the component-based simulation environment, the port is also the mechanism through which the component model communicates with the system solver [33]. Through the use of the ports, the system solver can provide the component model with the input parameters necessary for the model execution, and the component model can return the results of the successful execution to the system solver.

A junction is a virtual point where multiple ports of the same working fluid from two or more components are connected. A junction does not store or generate the flow, and thus the working fluid must observe the balance of mass flow rate and energy as it passes through the junction. Moreover, the pressure level of the ports connected to one junction must be the same.

2.1.2. Fluid group and fluid loop

A fluid loop is the complete path for a set of working fluid in a system. A fluid loop may be either closed or open. A system may consist of multiple fluid loops. E.g., Figure 2.1 shows a system with five fluid loops, three of which are closed loops and two are open loops.

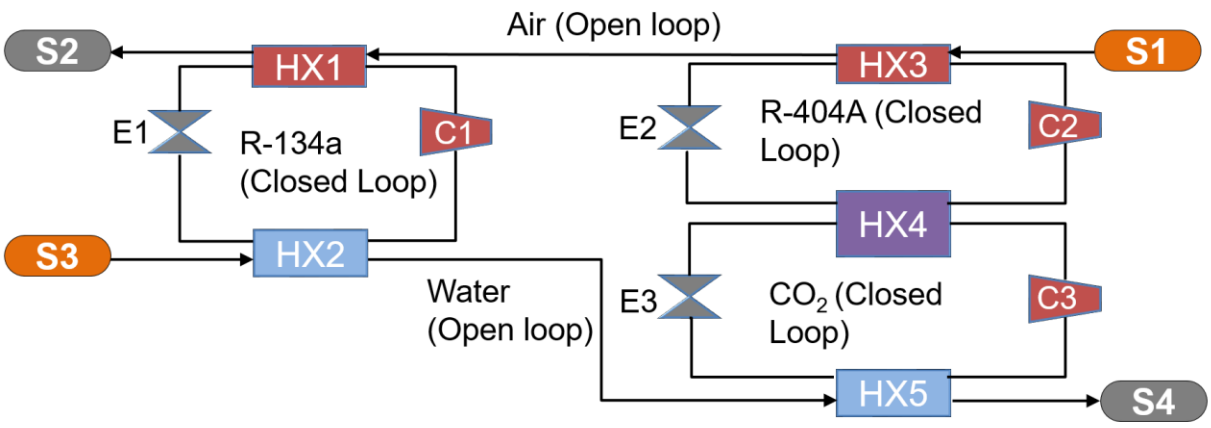

Figure 2.1 Example of a system with multiple fluid loops

Different from the concept of the fluid loop, a fluid group is the path for a set of working fluid in a component. A component may be associated with multiple fluid groups. E.g., HX1 in the five-fluid loop system in Figure 2.1 is associated with two working fluids (R134a and air), and thus it has two fluid groups. Similarly, HX2 – HX5 also have two fluid groups. On the other hand, C1 – C3 as well as E1 – E3 are associated with one refrigerant, and thus they have one fluid group only.

2.1.3.Source and sink

A source and a sink can represent the start and the end of an open fluid loop. E.g. in the system in Figure 2.1, S1 and S2 are the source and the sink for the air open loop, and S3 and S4 are the source and the sink for the water open loop, respectively.

2.1.4.Component boundary condition

The component boundary condition determines the set of input and output parameters of a component model that can be accessed by the system solver. As shown in Table 2.1, a component model may implement either mass flow-based or pressure-based boundary condition type for the component-system communication. Component models using mass

flow-based boundary condition include the friction-based components such as the heat exchanger and the pipe, while compressors and expansion devices are typical pressure-based boundary condition components.

Table 2.1 Component model boundary condition type

Boundary condition type	Model input parameters	Model output parameters	Example
Mass flow based	Inlet pressure (P_{in}), inlet enthalpy (h_{in}), inlet mass flow rate ($\dot{m}_{in}$)	Outlet pressure (P_{out}), outlet enthalpy (h_{out}), Outlet mass flow rate ($\dot{m}_{out}$)	Heat exchanger and pipe
Pressure based	Inlet pressure (P_{in}), inlet enthalpy (h_{in}), outlet pressure (P_{out})	Outlet enthalpy (h_{out}), inlet and outlet mass flow rate ($\dot{m}_{in}$, $\dot{m}_{out}$)	Compressor and expansion device

2.2. Generalized representation of vapor compression systems

The current simulation framework categorizes the component behaviors into three types: heat and mass transfer components, flow control devices, and source/sink components. The heat and mass transfer components compute the component performance based on physics or performance data for a given set of geometric and operating inputs. Most vapor compression system devices, e.g. compressor, HX, pipe fall into this category. Flow control devices regulate the flow of the working fluid in the component. One example is the four-way valve in a heat pump system. Sink and source components are explained in Section 2.1.3.

With the above-mentioned categorization, we can assume that any vapor compression system with arbitrary configurations and layouts can be represented by a network of these

components, and it may consist of multiple fluid loops. Furthermore, the component implementations obey the following convention in the current simulation framework:

i) All components (except for the sources and sinks) in the system must implement either pressure-based or mass flow-based boundary condition type (Table 2.1).

ii) There must be at least one flow-driving device (compressor, pump, or other device that is responsible for generating all the mass flow) in a closed loop.

Based on the conventions above, the current simulation framework can further reduce any vapor compression system into 10 base configurations that determine the way in which the components are connected. The base configurations are shown in Table 2.2. No. 1 to 4 are configurations with any two components in series. No. 5 to 7 are splitting configurations with two parallel components. No. 8 to 10 are merging configurations with two parallel components. It should be noted that splitting or merging configurations with more than two components can be regarded as derivation of the base configurations, and thus for brevity, they are not shown in the table.

Table 2.2 Ten base configurations in vapor compression systems

No.	Base configuration	No.	Base configuration
1	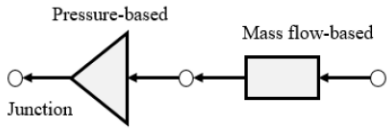	2	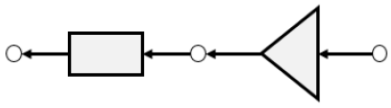
3	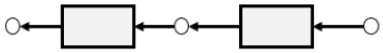	4	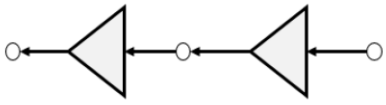
5	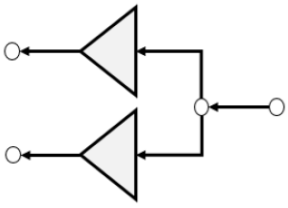	6	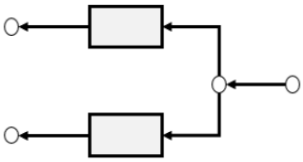

No.	Base configuration	No.	Base configuration
7	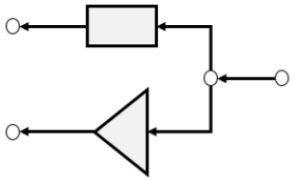	8	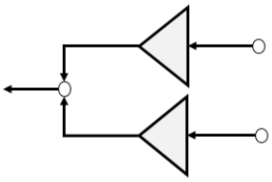
9	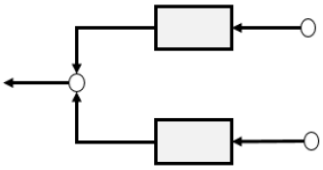	10	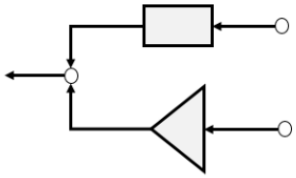

2.3. Component model standard

The component model standard is the key infrastructure that helps manage all the components in a component-based simulation environment. In such an environment, the detailed equations governing each component model are not exposed to the system solver. Each component model is regarded by the system solver as a "black box" with a set of input and output boundary parameters. Thus, the current simulation framework includes a standardized structure for all the participating component models that provides a "communication protocol" between the system solver and the component models.

2.3.1.Standardized data structures

The component model standard dictates the following set of hierarchical data structures for a heat and mass transfer component:

- Fluid Group
  - Working fluid
  - Charge
  - Heat capacity

- Work
- Power consumption
- Port States
    - State properties: pressure, temperature, enthalpy, quality, etc.
    - Mass flow rate
- Port Mapping Table
    - Nominal inlet and outlet port IDs

At the top of the hierarchy is a Fluid Group, whose concept is described in Section 2.1.2. It is used to represent the path, states and performance of one set of working fluid in a component.

Port Mapping Table is the data structure that represents the path of the working fluid in one fluid group. It specifies which port(s) are the inlet and which are the outlet under the nominal operating condition. If the flow in the component is reversed in another operating condition, the inlet and the outlet ports will be switched.

Port States is the data structure that represents the states at different ports. It includes both the state properties and the mass flow rate. The performance of the Fluid Group includes charge, heat capacity, work, and power consumption. They are required to evaluate the performance of each fluid loop and the entire system.

For a flow control device component, the only standardized data structure required is the Port Mapping Table. For a source/sink component, the only data structure required is Port State.

2.3.2.Component lifetime

The structure of the component model standard contains seven key blocks, each of which may comprise of one or more stages. These seven blocks are component initialization, save/load, user interface, property routine setup, model execution, and component termination. Their descriptions are listed in Table 2.3.

Table 2.3 Structure of the component model standard

Block	Stage	Description
Component initialization	Initialize	Creates/initializes Fluid Groups, boundary condition type, folder paths, etc.
Load/Save	Load	Loads the component parameters from an external file.
	Save	Saves the component parameters to an external file.
User interface	Edit parameters	Displays a graphical user interface to faciliatate the users to change the component parameters.
Property routine setup	Set property routine	Sets the information to the component about the property folder paths and library type that required for the property state calculation in the model execution.
Model execution	Begin simulation	Allows for necessary pre-processing of the component simulation.
	Run	Executes the physics- or performance data-based component model.
	End simultion	Allows for necessary post-processing based on how the component simulation ended.
Component termination	terminate	Unloads the component from the program.

Over the span of a system simulation, the above mentioned stages are invoked by the system solver in a fixed sequence. And the sequence of the component stage during the system simulation is referred to as the component lifetime, as shown in Figure 2.2.

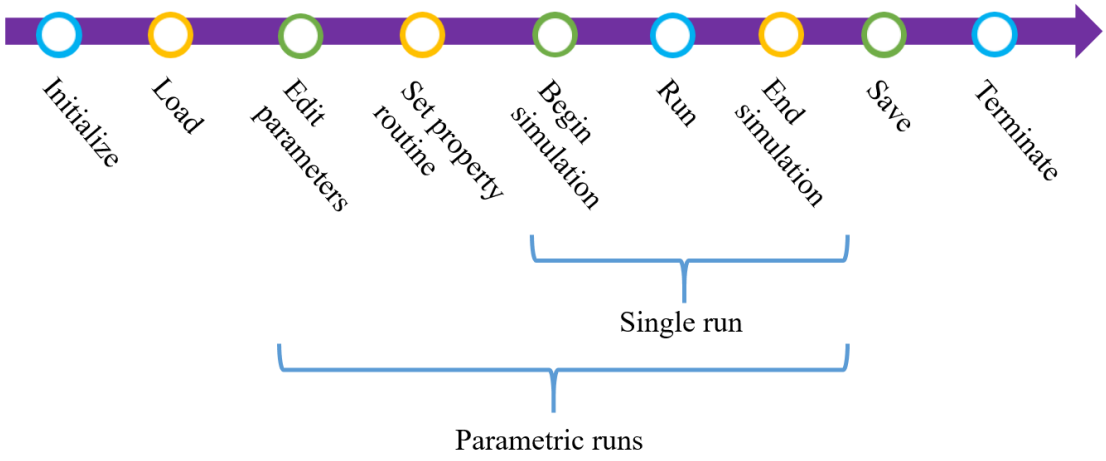

Figure 2.2 Component lifetime over the span of system simulation

Component initialization is always the first stage in a component lifetime. Then, the geometric and physical parameters of the component may be either loaded from an existing file, or edited through a graphical user interface. Next, the system solver sets the property library information to the component, before it goes through the model execution, which comprises of Begin simulation, Run and end Simulation. During the Run stage, the system solver propagates the component inlet states to the PortStates data structure, runs the model code, and then accesses the Fluid Group data structure for outlet states and component performance data. The component parameters may be saved to an external file, before the component gets terminated. It should be noted that the events from Edit Parameters to End Simulation may happen multiple times in the case of parametric runs.

2.4. General-purpose system solver outline

The system solver receives the input information of the components and component connections from the user. Then it conducts the following main blocks:

i) Processing of the system configuration information. In this block, the system solver generates the junction table of the system configuration, and organizes the components into separate fluid loops.

ii) Determination of the flow direction map. This block will be elaborated in Section 2.4.1.

iii) Mathematical formulation. This is elaborated is Section 2.4.2 and 2.4.3.

iv) Component executions and residual evaluation. In this block, the system of equations generated by block iii is delegated to an iteration procedure. The component models executions are iterated until the system state points satisfy all the residual equations.

v) Post-processing and results output.

2.4.1.Flow direction map determination

The flow direction map is the traveling route of the working fluids in a system. The determination of flow direction map based on the system configuration is one of the major distinctions from the previous vapor compression system simulation tools [33] [34].

2.4.1.1.Implementation of physical ports

The previous simulation tools [27, 33] all implemented the logical ports: the flow direction is implied by the evenness/oddness of the port number. The advantage of the logical ports is that the flow direction is directly resulted from the component connections. The disadvantage is that the user has to provide different sets of component connections for a system with multiple operation modes. For example, a basic reversible heat pump system has two operating modes (cooling and heating mode). The Variable

Refrigerant Flow system with simultaneous heating and cooling may have five to seven operation modes. Therefore, the implementation of logical ports significantly reduces the flexibility of the simulation tool to handle complex systems.

Thus, in this framework, physical ports were implemented: the port number no longer implies the flow direction at the current port. It only represents its sequence in a list of ports in a component fluid group. Therefore, the first key method in this simulation framework is to determine the flow direction at each port given a set of component connections.

We use the mass flow sign to represent the flow direction of the port. The negative sign represents that the fluid is flowing out of the port, and positive if it is flowing into the port. The only information of which we are certain is the directions for ports that belong to the compressors, sources and sinks (we will refer to these ports as the *irreversible ports*). The flow directions at the rest of the ports are determined by the mass flow sign propagation.

2.4.1.2. Mass flow sign propagation

Mass flow sign propagation within a component is facilitated by the data structure of Fluid Group and Port Mapping Table. The mass flow sign will only be propagated within the same fluid group of a component. And the port mapping table of the relevant fluid group will be queried upon mass flow sign propagation.

For a junction, there are two principles governing the mass flow sign propagation. The first junction principle is given by

$$\left|\sum_{i=1}^{N} y_i\right| < N \tag{1}$$

where N is the number of ports associated with the junction, and y is the integer (1 or -1) representing the flow direction at each port. Eq. (1) means that, because a junction does not store or generate the flow, the ports of the same junction cannot be all inlets ($y = 1$) or all outlets ($y = -1$). E.g. for a two-port junction, if one port is known to be an outlet, the other must be an inlet, and vice versa. For a three-port junction, if two of them are known to be outlets, then the 3rd port must an inlet (as shown in Figure 2.3 (a)), and vice versa. On the other hand, as shown in Figure 2.3 (b), if two of them are one inlet and one outlet, the direction at the 3rd port is *ambiguous*. As shown in Figure 2.3 (c), if only one port has a determined flow direction, the directions at the other two ports are also *ambiguous*.

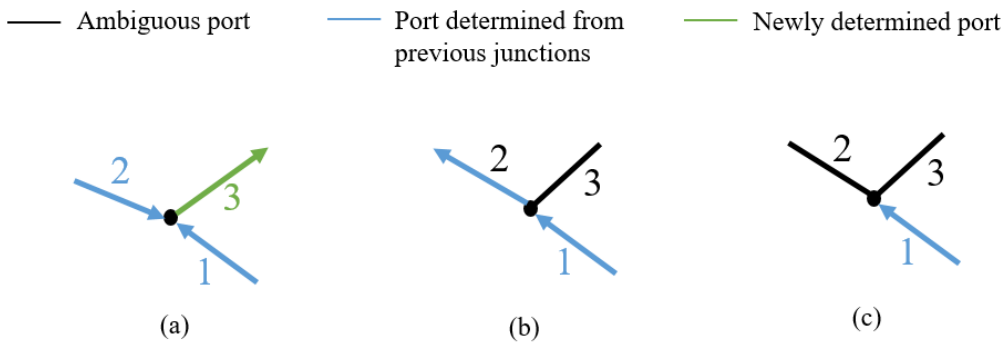

Figure 2.3 Illustration of the first principle with a three-port junction

This principle alone cannot solve the flow direction map. For systems with multiple splits and merges, applying this principle alone easily ends up with many ambiguous ports. Thus, we introduce the concept of the *full flow components* to further facilitate the mass flow sign propagation. The full flow components of each fluid loop are the components that see the total mass flow rate of the current loop. We assign dummy flow

rates to their ports such that they equally share the flow rate of the current loop. For example, in most cases, the compressors and the sources serve as the full flow components in a closed fluid loop and an open fluid loop, respectively.

Therefore, we have the second principle to apply to the mass flow sign propagation on a junction: for an N-port junction, if there are n ports (n<N) that satisfy

$$\begin{aligned} &y_1 = y_2 = \ldots = y_n, \\ &\sum_{i=1}^{n} \tilde{\dot{m}}_i = 1 \end{aligned} \tag{2}$$

where y is the flow direction integer and $\tilde{\dot{m}}$ is the dummy flow rate, then the rest of the ports share the same mass flow sign, which must be the opposite to the mass flow sign of those n ports. Their dummy flow rate is $\frac{1}{N-n}$.

As an example, Figure 2.4 shows a five-port junction, with two ports (port 1 and 4) determined from the previous junctions. The flow directions of the rest of the ports (port 2, 3, and 5) are ambiguous according to the first principle, because there exists multiple combinations of these ports that satisfy Eq.(1). However, according to the second principle, because port 1 and 4 satisfy Eq.(2), the flow directions of port 2, 3, and 5 must be opposite to port 1 and 4.

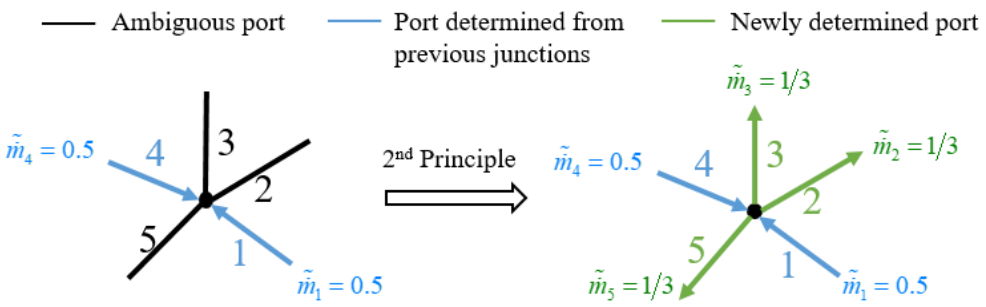

Figure 2.4 Illustration of the second principle with a five-port junction

2.4.1.3. Flow direction map determination flowchart

Figure 2.5 shows the flowchart to determine the flow direction map per fluid loop. For each loop, the mass flow sign propagation starts out with obtaining the mass flow signs at the irreversible ports, and assigning the dummy flow rates to the full flow components. Then the mass flow sign propagation proceeds using the information of the components' state tables and the two junction principles. During the mass flow propagation, if there exists ports with inconsistent signs, the method would terminate and report such ports.

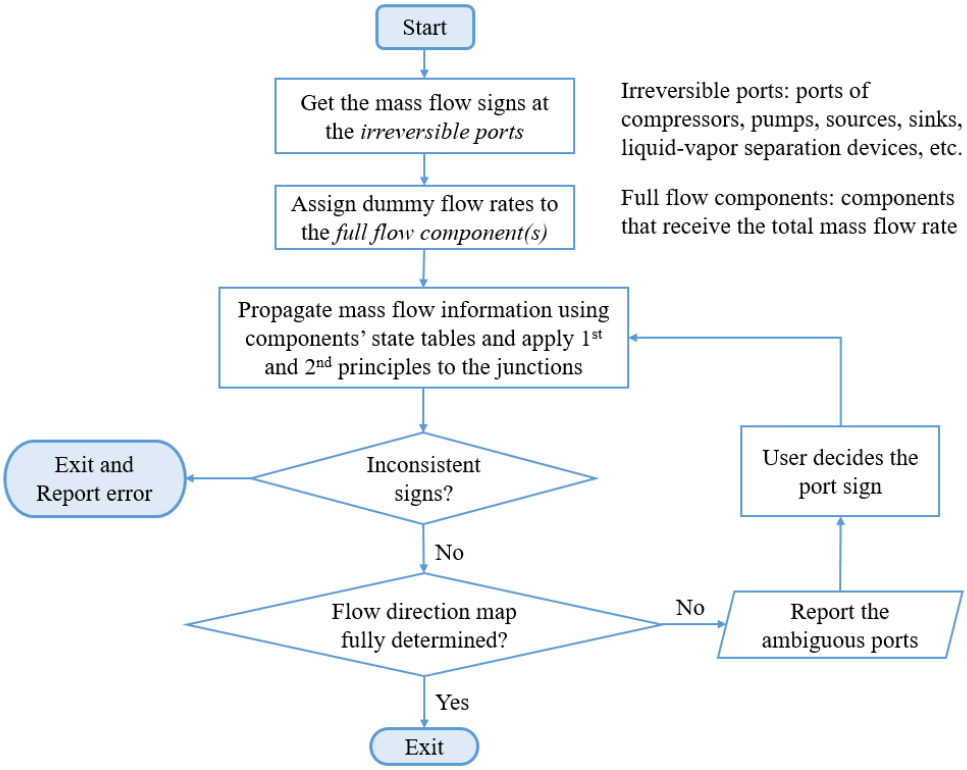

Figure 2.5 Flowchart to determine the flow direction map per fluid loop

If there still exists ambiguous ports after the mass flow sign propagation, then the full determination of the flow direction map would require additional information of physical properties. And such properties usually cannot be obtained until after the component

executions. In such situations, the ambiguous ports would be exposed to the user's decision. For example, in Figure 2.6, the two ports of C_3 are ambiguous. The two possible flow patterns are shown in (a) and (b), respectively. And the actual flow direction in C_3 would depend on the pressure levels at J2 and J3, which cannot be determined until the pressure drop of the other components are known. Thus, the ports of C_3 would be reported to the user.

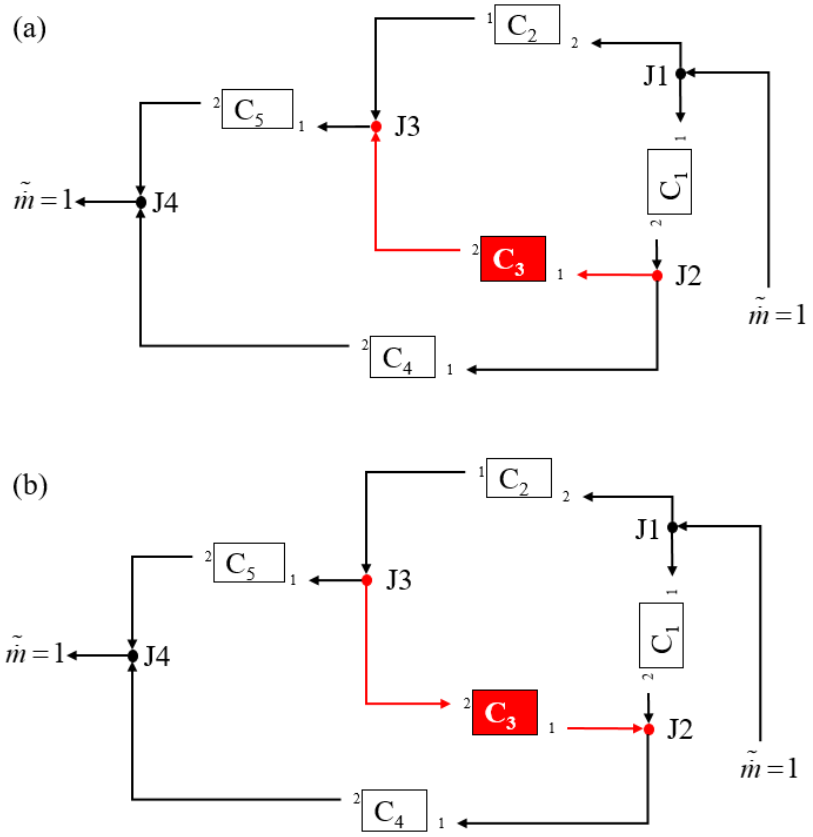

Figure 2.6 Example of ambiguous ports (in red) after the mass flow sign propagation

2.4.2.Generic formulation of the system of equations

After the flow direction map is fully determined, we need to identify the unknown variables and to formulate the equations. This section presents a generic method to formulate the system of equations that describe the steady state of an arbitrary system. As

described in Section 2.3, in the component-based simulation environment, each component model is seen by the system solver as a black box that maps the inlet parameters of this component to its outlet parameters. Thus, the system of equations in the context of this simulation framework does not involve any component-level equations that govern the heat transfer and hydraulic relations in the components.

2.4.2.1. Formulation of the unknown variables

The system-level unknown variables are the input parameters of each component model. The model input parameters depend on the boundary condition type of the component model. Each pressure based component with N_{in} inlet ports and N_o outlet ports brings the following unknown variables.

Pressure at each of the inlet ports: $P_i, i = 1, ..., N_{in}$

Enthalpy at each of the inlet ports: $h_i, i = 1, ..., N_{in}$

Pressure at each of the outlet ports: $P_i, i = 1, ..., N_o$

Each mass flow based component with N_{in} inlet ports brings the following unknown variables.

Pressure at each of the inlet ports: $P_i, i = 1, ..., N_{in}$

Enthalpy at each of the inlet ports: $h_i, i = 1, ..., N_{in}$

Mass flow rate at each of the inlet ports: $\dot{m}_i, i = 1, ..., N_{in}$

2.4.2.2. Formulation of the system-level conservation equations

The system-level equations are formulated based on the conservation/balance relations at each junction. Since the pressure level of the ports connected to one junction must be the same, an N-port junction would result in N-1 pressure balance equations, given by

$$P_1 = P_i, i = 2, ..., N \tag{3}$$

Since a junction does not store or generate the flow or the energy, each junction would result in one mass flow balance equation and one energy balance equation, given by

$$\sum_{i=1}^{N_{in}} \dot{m}_i = \sum_{j=1}^{N_o} \dot{m}_j \tag{4}$$

$$\sum_{i=1}^{N_{in}} \dot{m}_i h_i = \sum_{j=1}^{N_o} \dot{m}_j h_i \tag{5}$$

where N_{in} and N_o are the number of inlet ports and outlet ports connected to the current junction. Furthermore, for a junction with N_{in} inlet ports (ports pointing out of the junction), the enthalpy at these ports are the same. Thus, each junction with N_{in} inlet ports would result in additional N_{in} -1 enthalpy balance equations, given by

$$h_1 = h_i, i = 2, ..., N_{in} \tag{6}$$

2.4.2.3. Additional closure equation for a closed fluid loop

For a closed loop with N junctions, although there will be N mass flow balance equations, these N equations are linearly dependent: any of the N-1 mass flow equations

can deduce the last equation. Therefore, we must remove one junction mass flow balance equation, and this results in the need for one more closure equation. This additional closure equation may come from specifying any of the system design parameters, such as system charge, suction superheat, system subcooling, etc.

For example, Figure 2.7 shows the connection of a simple 4-component vapor compression system. And Table 2.4 shows the 12 unknown variables and the conservation equations. Since the four components in this system are single fluid group component, the fluid group notations are omitted. The mass flow balance equation at J1 is not included in the equations (Removing mass flow balance equation at any junction would be mathematically equivalent). As a result, one additional closure equation is added, which is the system design parameter.

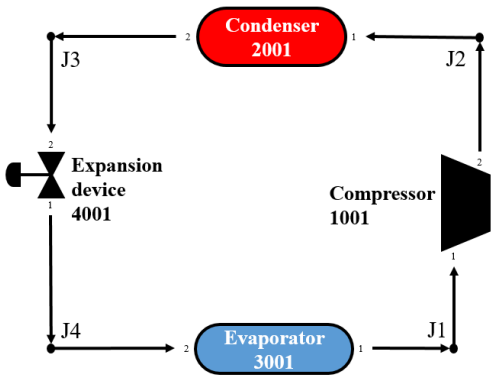

Figure 2.7 Schematic of a 4-component vapor compression system

Table 2.4 Unknown variables and conservation equations for a 4-component cycle

No.	Unknown variable	Conservation equation	No.	Unknown variable	Conservation equation
1	$P_{1001,1}$	$P_{1001,1} = P_{3001,1}$	7	$P_{4001,2}$	$h_{4001,2} = h_{2001,2}$
2	$h_{1001,1}$	$h_{1001,1} = h_{3001,1}$	8	$h_{4001,2}$	$\dot{m}_{4001,2} = \dot{m}_{2001,2}$
3	$P_{1001,2}$	$P_{2001,1} = P_{1001,2}$	9	$P_{4001,1}$	$P_{3001,2} = P_{4001,1}$
4	$P_{2001,1}$	$h_{2001,1} = h_{1001,2}$	10	$P_{3001,2}$	$h_{3001,2} = h_{4001,1}$
5	$h_{2001,1}$	$\dot{m}_{2001,1} = \dot{m}_{1001,2}$	11	$h_{3001,2}$	$\dot{m}_{3001,2} = \dot{m}_{4001,1}$

No.	Unknown variable	Conservation equation	No.	Unknown variable	Conservation equation
6	$\dot{m}_{2001,1}$	$P_{4001,2} = P_{2001,2}$	12	$\dot{m}_{3001,2}$	System design parameter specification

This method differs from the Junction Solver algorithm [27] because the Junction Solver require all components implement the pressure based boundary condition. This requirement has a severe impact on the usability of the algorithm. It also increases the computation effort. The implementation of pressure based boundary condition on friction-based components such as heat exchangers and pipes results in additional component-level iterative procedures to determine refrigerant mass flow rate. This method, however, does not put any constraint on the component boundary condition type, and thus greatly increases the overall usability of the simulation framework.

2.4.3.Tearing system of equations for arbitrary vapor compression systems

Although the system of equations as formulated in 2.4.2 is generic for all system configurations, it is too large to be directly delegated to the Newton or quasi-Newton iteration scheme, especially when the system configuration gets complicated. Moreover, the success of any Newton-based scheme highly depends on good initial guesses. So, the larger the number of unknowns, the more insight required from the users into the system they are modeling to ensure the success of the solution process. This becomes a usability issue and can compromise the solver robustness. Therefore, we need to reduce the dimensionality of the system of junction equations formulated in the previous section.

There are various algorithms for the symbolic manipulation of large differential algebraic equation (DAE) systems [44]. Of them, the tearing algorithm [45] is the most relevant strategy for dimensionality reduction of vapor compression systems.

2.4.3.1. Tearing variables and residual equations for vapor compression systems

The system of equations for vapor compression systems is a typical example of an algebraic loop [46]: the unknown variables are coupled with one another, and there is not a single equation that can be solved independently. However, the loop can be torn apart by taking an initial guess at the input parameters of one component model.

Let us assume the four component models in Figure 2.7 all implement the mass flow-based boundary condition type: they take inlet pressure, inlet enthalpy and inlet mass flow rate as the input parameters, and output outlet pressure, outlet enthalpy, and outlet mass flow rate. Then, the output parameters of the upstream component are essentially the input parameters of the downstream component, given the junction conservation equations.

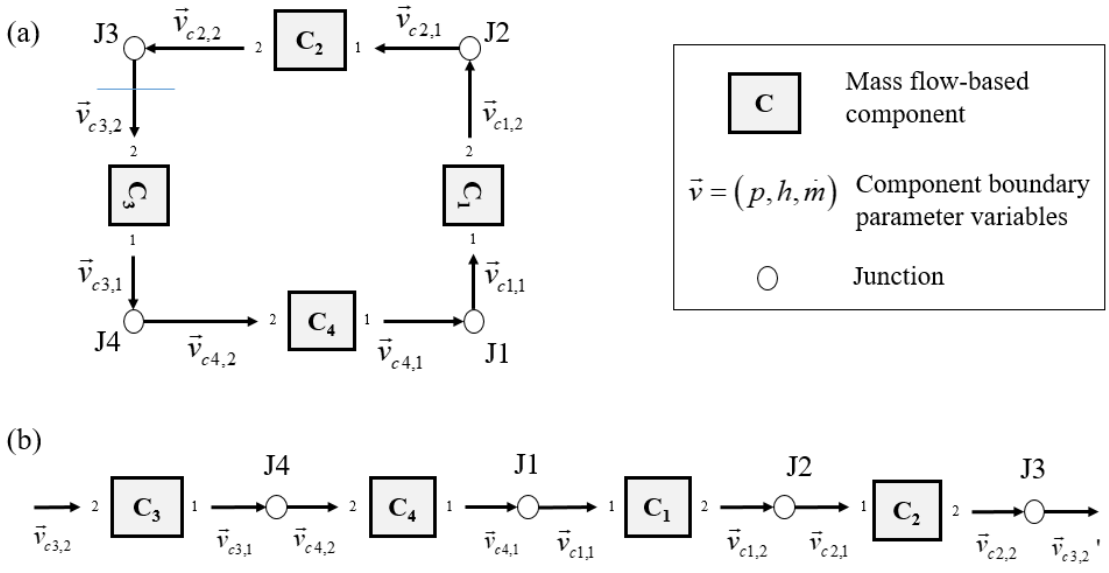

Figure 2.8 Tearing apart a 4-mass flow-based component system: (a) before (b) after

Thus, the loop, as shown in Figure 2.8 (a) can be easily torn apart at any component. For example, breaking the branch corresponding to the inlet parameters of C_3 would give

the graph as shown in Figure 2.8 (b), which suggests the following way of organizing the component executions to find the solution.

Initial $\vec{v}_{c3,2} = \left(p, h, \dot{m} \right)_{c3,2}$

REPEAT

$$\vec{v}_{c3,2} \xrightarrow{C_3} \vec{v}_{c3,1}$$
$$\vec{v}_{c3,1} \xrightarrow{J4} \vec{v}_{c4,2}$$
$$\vec{v}_{c4,2} \xrightarrow{C_4} \vec{v}_{c4,1}$$
$$\vec{v}_{c4,1} \xrightarrow{J1} \vec{v}_{c1,1}$$
$$\vec{v}_{c1,1} \xrightarrow{C_1} \vec{v}_{c1,2}$$
$$\vec{v}_{c1,2} \xrightarrow{J2} \vec{v}_{c2,1}$$
$$\vec{v}_{c2,1} \xrightarrow{C_2} \vec{v}_{c2,2}$$
$$\vec{v}_{c2,2} \xrightarrow{J3} \vec{v}_{c3,2}'$$

UNTIL converged $\left(\vec{v}_{c3,2} - \vec{v}_{c3,2}' \right)$

The variables selected to tear apart the algebraic loop are the *tearing variables.* After the tearing variables are selected, the corresponding equations to be solved for are the *residual equations*. In this case, the input vector (containing 3 parameters) of C_3 are the tearing variables. The vector equation $\vec{v}_{c3,2} - \vec{v}_{c3,2}' = 0$ are the residual equations. The tearing has reduced the dimensionality of the problem from 12 to 3.

It should be noted that there are usually many ways to tear an algebraic loop, and different tearing strategies would result in different problem dimensions, and different sets of residual equations. In this case, tearing from any of the four components does not make a difference. However, in a real vapor compression system, the components does not implement uniform boundary condition type, and there are splits, merges, and

multiple fluid loops. All of them present complications that require an algorithm to carefully select the tearing variables, and find the corresponding residual equations.

2.4.3.2. Tripartite graph method

Tarjan [47] used a bipartite graph to represent any system of equations. It enumerates the equations in one set and the unknown variables in on other. A connecting line between an equation and an unknown indicates that the unknown appear in the equation. Tarjan algorithm consists in a procedure by which the graph is being colored to identify and isolate algebraic loops.

However, Tarjan algorithm, or any other tearing algorithms [48] cannot be directly applied to our problem. The bipartite graph on which the Tarjan algorithm was based uses two columns of vertices to represent the equations and variables separately. These two columns are sufficient representation in the acausal modeling approach. However, the component-based approach is not an acausal approach. In addition to the junction equations and the unknown variables, there is a different type of structure that is absent in the acausal approach: component models with predefined inputs-outputs relations. Therefore, the bipartite graph is not sufficient to represent all the information in the component-based simulation. In order to account for the causality in the component-based approach, we propose a tripartite graph, with a third column of vertices to represent the component models. This is a necessary adaptation of a graphical method that is ideal in an equation-based acausal modeling paradigm to a component-based causal modeling paradigm.

Let us consider the vapor compression system is Figure 2.9. Component C_1 is the compressor model with pressure-based boundary condition, C_2 is the outdoor HX model

with pressure-based boundary condition, and C_3 is the indoor unit model with mass flow-based boundary condition. Since all components are single fluid group component, we will omit the fluid group notations.

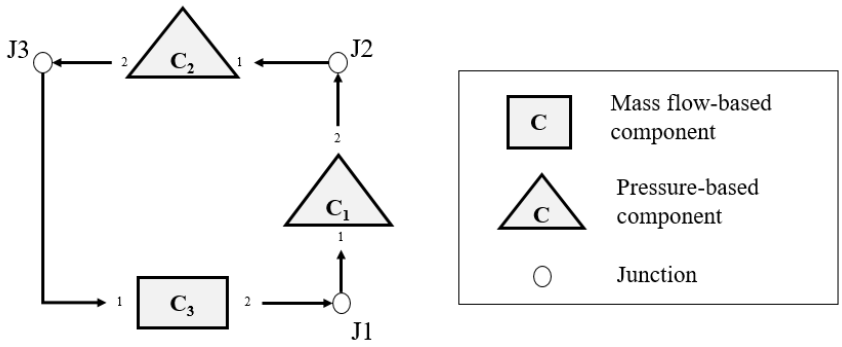

Figure 2.9 Three-component vapor compression system

The system of equations for this vapor compression system can be represented by a tripartite graph as shown in Figure 2.10. The graph has three sets of vertices. One set is for the component models. One set is for the variables, including the input and output parameters of each component model (e.g., $p_{1,2}$ represents the pressure of port 2 of C_1). And one set is for the junction balance equations, formulated as discussed in Section 2.4.2.2. There are only 8 equations (instead of 9) for the 3 junctions, because one of the mass flow balance equations is redundant.

In the tripartite graph, each component model is connected to 6 variables by the directed lines. If the directed line is oriented toward the component model, the variable is an input parameter for this component. Otherwise, the variable is an output parameter. A component model is ready for execution when all of its input parameters are known. Each junction balance equation is attached to at least 2 variables by undirected lines. An equation is ready to be solved for when there is only one unknown variable attached to this equation. And this variable is the *output variable* for the equation.

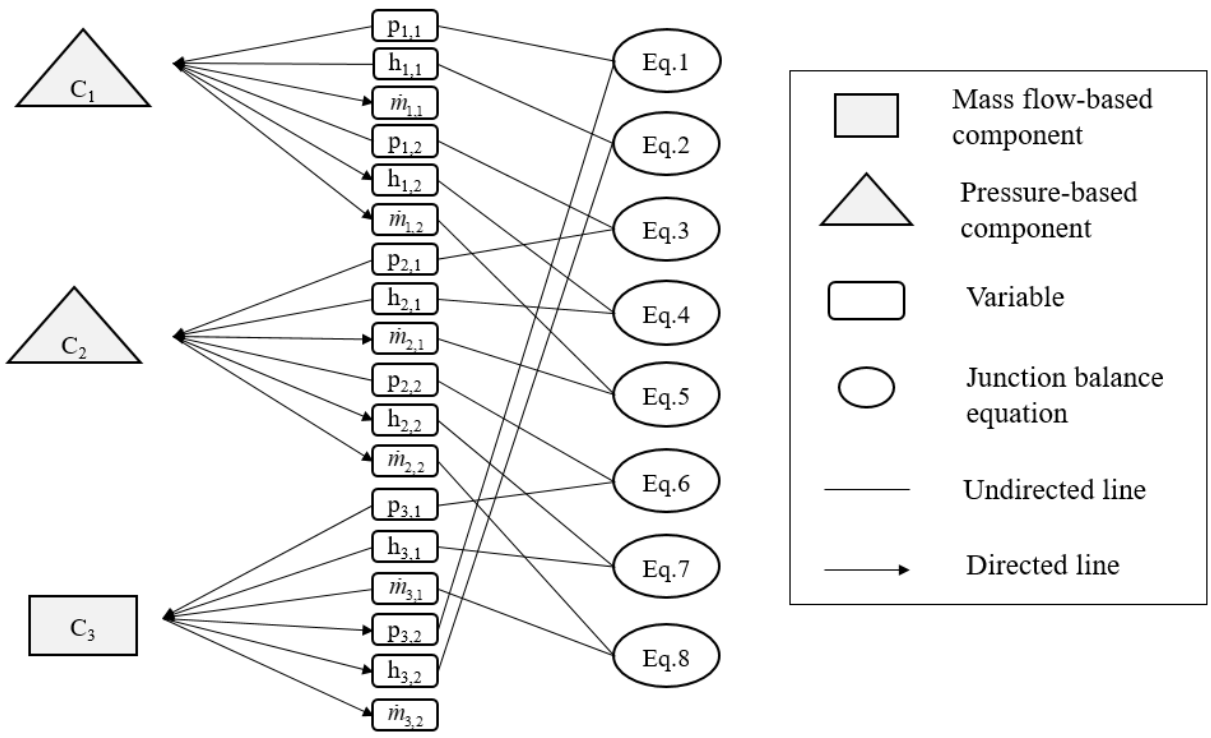

Figure 2.10 Tripartite graph for the three-component system in Figure 2.9

The tripartite graph is a complete algebraic loop: there are no executable component models, nor solvable equations. Therefore, we must select the initial tearing variables to break the loop. As discussed in Section 2.4.3.1, it is mathematically equivalent to tear at any of the components. However, our knowledge of these systems tells us that, in most cases, the best option for the initial tearing variables is the input parameters of the compressors. This is because, the engineers that design the vapor compression system usually have a good sense of the operating pressures of the compressors in a system. Moreover, the mass flow rate calculated by the compressor model can be propagated to the rest of the system. Therefore, we will use the input parameters of the compressor (C_1) as the initial tearing variables, and this will result in C_1 being executable.

After C_1 execution, we color the known variables and their attached lines into blue. And this results in 5 solvable equations (Eq.1 – Eq.5). We color the output variables of

these equations into blue. And if the output variable is a component input, we color the directed line attached to this output variable in blue. Figure 2.11 shows the updated tripartite graph, which is again trapped in an algebraic loop. Therefore, new tearing variables are required. The graph shows that all of the input parameters of C_3 are still unknown, while C_2 has only one unknown input parameter, which is the outlet pressure. So clearly, it should be the 4th tearing variable. And C_2 becomes executable.

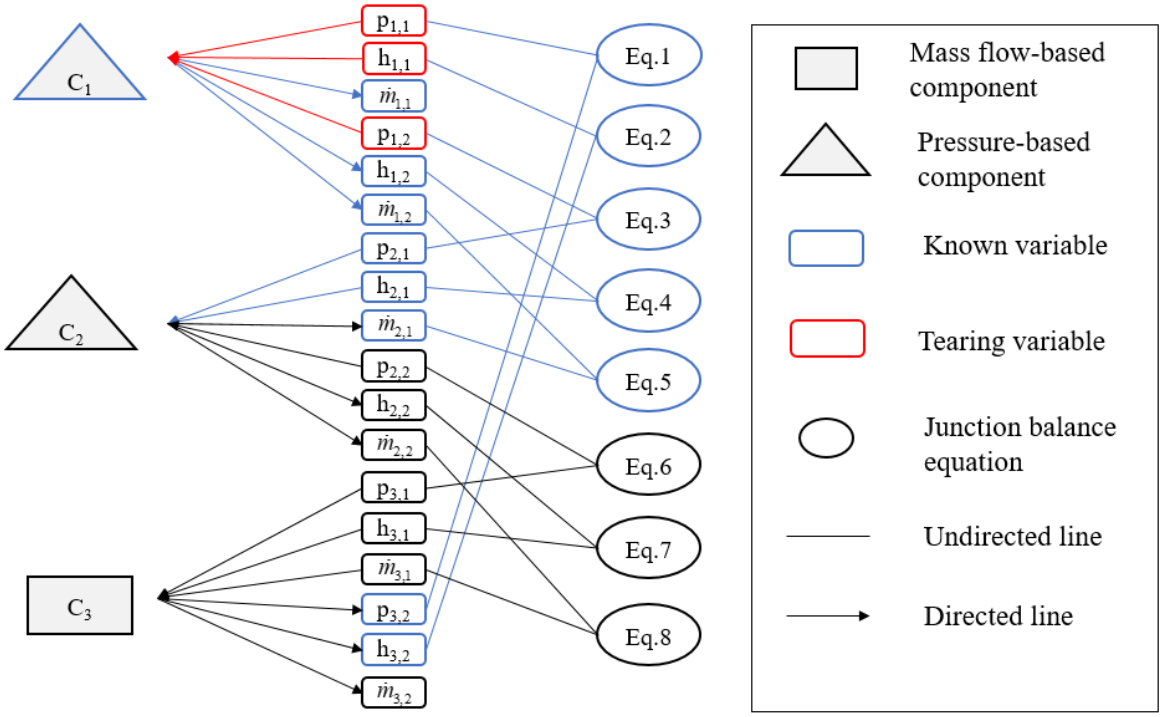

Figure 2.11 Updated tripartite graph for the three-component system in Figure 2.9

As shown in Figure 2.12, the new tearing variable and C_2 execution results in 3 solvable equations (Eq.6 – Eq.8), which enables C_3 execution without having to add any more tearing variables. However, as we are trying to color $\dot{m}_{2,1}$, which is one of the output parameters from C_2 execution, this variable has already been colored, because it was the output variable of Eq.5. This means that, the tearing variable $P_{2,2}$ must be iterated

until the mass flow rate of C_2 equals that of C_1. Therefore, Eq.5 is a residual equation. Similarly, Eq.1 and Eq.2 are also residual equations.

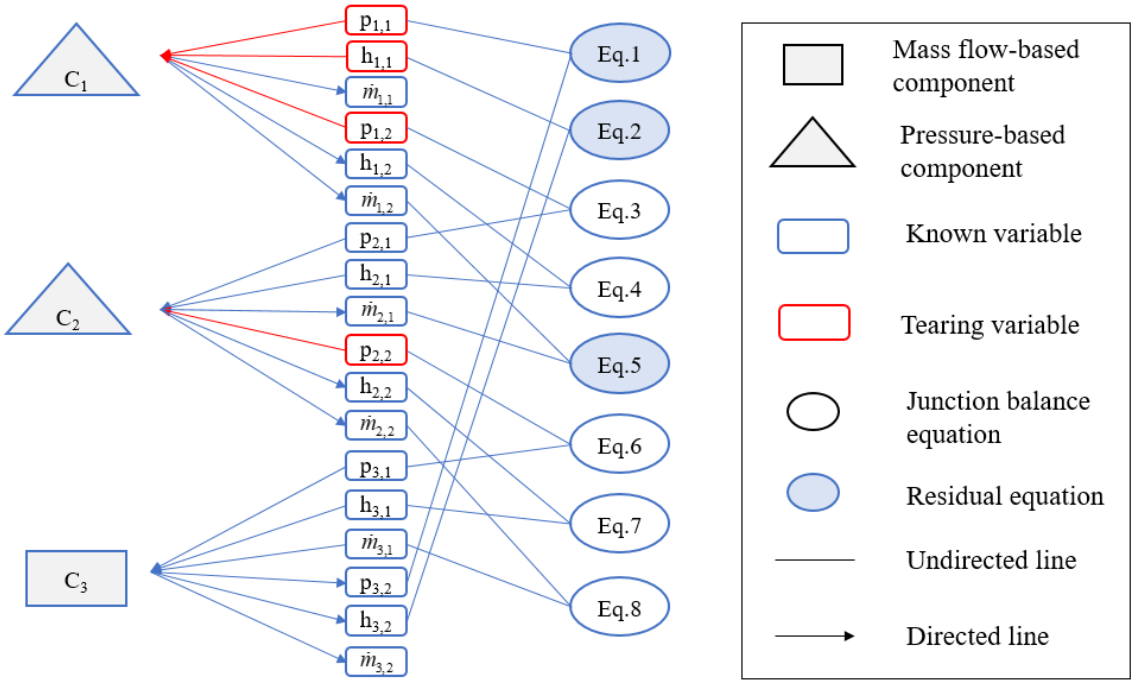

Figure 2.12 Final tripartite graph for the three-component system in Figure 2.9

Till now we have 4 tearing variables, but only 3 residual equations. The last equation is the system design parameter specification, as discussed in section 2.4.2.3. Now we have reduced the dimension of the problem to 4. The tearing variables and residual equations for the three-component system are listed in Table 2.5, which can now be delegated to a Newton or quasi-Newton iteration procedure.

Table 2.5 List of tearing variables and residual equations for the system in Figure 2.9

No.	Tearing variable	Residual equation
1	$P_{1,1}$	Eq.1: $P_{1,1} = P_{3,2}$
2	$h_{1,1}$	Eq.2: $h_{1,1} = h_{3,2}$
3	$P_{1,2}$	Eq.5: $\dot{m}_{2,1} = \dot{m}_{1,2}$
4	$P_{2,2}$	System design parameter specification

2.4.3.3. Tripartite graph-based tearing algorithm for arbitrary vapor compression systems

The notations for the tripartite graph method are listed in Table 2.6 for quick reference. The tripartite graph used to represent generalized vapor compression systems is defined as a network $G=\{C,V,U,L\}$. C, V, U are three vertex sets that denote the set of components, unknown variables, and junction balance equations. L is the set of lines or edges in the graph. All lines in the tripartite graph have one endpoint in V, and the other in U or C. We use $\kappa(u,v)=1$ to denote that variable *v* is attached to equation *u*, and $\kappa(u,v)=0$ denotes that *v* is not attached to *u*. The connection between U and V is an undirected graph, so that $\kappa(u,v)=\kappa(v,u)$. On the other hand, the connection between C and V is a directed graph. So we use $\kappa'\langle c,v\rangle=1$ to denote that variable *v* is attached to component *c*, and that *v* is an output parameter. Similarly, $\kappa'\langle v,c\rangle=1$ denotes that variable *v* is an input parameter of component *c*.

Table 2.6 Notations and explanations

Notations	**Explanations**
C, V, U	A set of components, variables, and equations
c, v, u	Component, variable, and equation
L	A set of lines/edges that connect the vertex in the graph
L_{uv}, L_{cv}, L_{vc}	Equation-variable connectivity matrix, Component-input variable connectivity matrix, and component-output variable connectivity matrix
$\kappa_{ij}=\kappa(u_i,v_j)=1$	Equation u_i contains variable v_j
$\kappa'_{ij}=\kappa\langle c_i,v_j\rangle=1$	variable v_j is the output parameter of component c_i
$\kappa'_{ji}=\kappa\langle v_j,c_i\rangle=1$	variable v_j is the input parameter of component c_i

Notations	Explanations
V^*	The set of known variables that result from equation solving or component symbolic execution; $V^* \subseteq V$
V_T	The set of tearing variables; $V^T \subseteq V^*$
U_R	The set of residual equations; $U_R \subseteq U$

With the notations mentioned above, we can formulate the problem as follows:

Given a set of components, variables, and equations: C, V, U, and the connectivity matrices: $L_{uv} = \{\kappa_{ij}\}$, $L_{cv} = \{\kappa'_{ij}\}$, $L_{vc} = \{\kappa'_{ji}\}$, *find the component execution sequence, so that we have the least number of tearing variables and residual equations to be delegated to a Newton or quasi-Newton iteration procedure.*

A tearing algorithm is developed to systematically determine the most efficient component execution order, and identify the tearing variables and residual equations for generalized vapor compression system. Figure 2.13 shows the flowchart, for arbitrary configurations with multiple open and closed fluid loops.

The algorithm starts out by determining the initial tearing variables, which are always the input parameters of the compressor in a closed loop. If there are more than one compressors in the same loop, just tear from any one. Then, the algorithm will identify the solvable junctions, and color their output variable. Similarly, it will identify the executable components, and color their output parameters. When there are no more executable components or solvable junction equations, the algorithm will check for unexecuted compressor models, and then will tear from the component model with the least unknown input parameters.

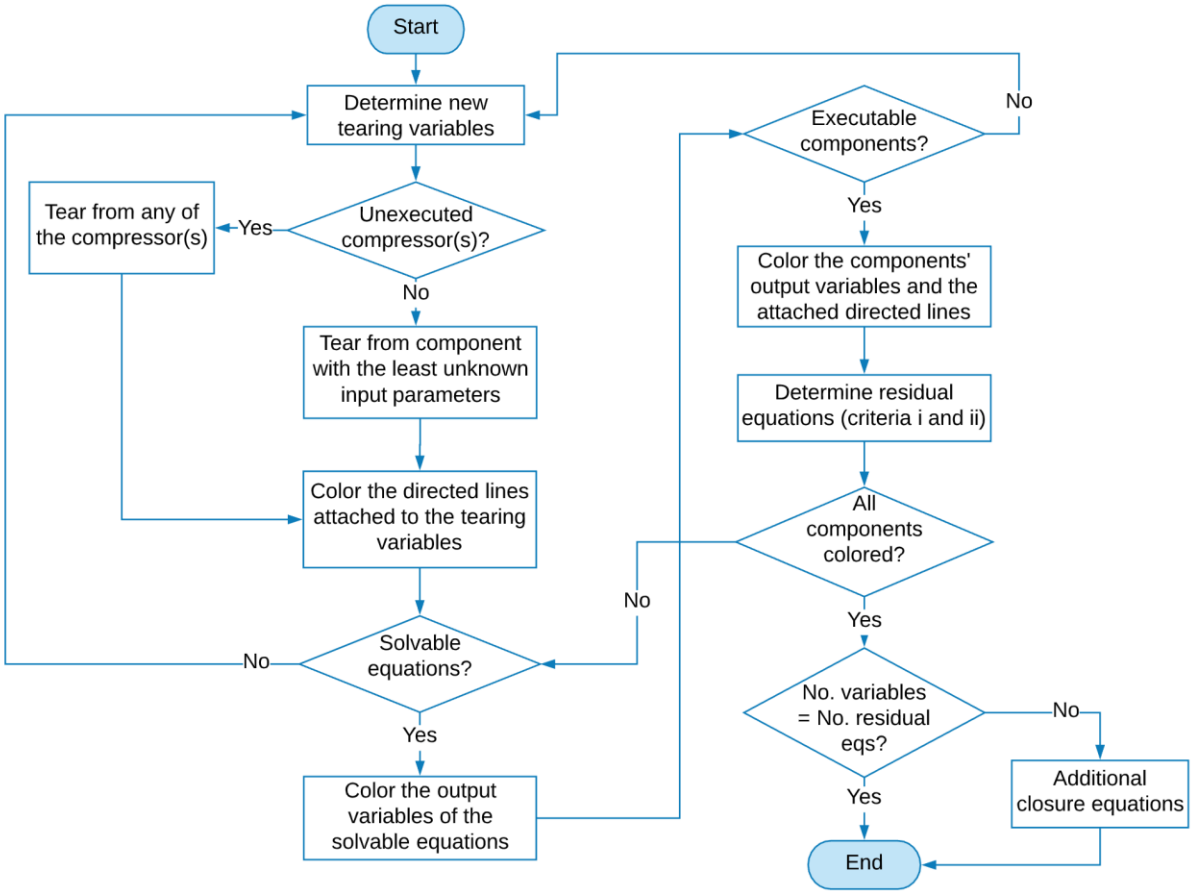

Figure 2.13 Flowchart of the tearing algorithm for arbitrary vapor compression systems

After each component coloring, the algorithm will update the set of known variables and tearing variables. We use c_k to denote the kth component to be symbolically executed. We use $v_{i,k}$ to denote the input parameters of component c_k, and $v_{o,k}$ denotes the output parameters. V_k^* is the updated known variables after c_k symbolic execution. The residual equation criteria are as follow:

For k = 2, 3, 4…

For each $v_{o,k}$

i) If $v_{o,k}$ has already been determined: $v_{o,k} \in V_{k-1}^*$

If there is an equation u_i s.t. $\kappa\left(u_i, v_{o,k}\right)=1$, u_i is a residual equation: $u_i \in U_R$

ii) If $v_{o,k} \notin V_{k-1}^*$

If an equation u_i satisfies all conditions below, $u_i \in U_R$:

ii.1) u_i contains this output parameter: $\kappa\left(u_i, v_{o,k}\right)=1$

ii.2) u_i contains at least one tearing variable: $\exists v:\ v \in V_T \ \& \ \kappa\left(v, u_i\right)=1$

ii.3) All variables attached to u_i have been determined: For

$V_{u_i}=\left\{v \mid \kappa\left(v, u_i\right)=1\right\}:\ V_{u_i} \subseteq V_k^*$

After all of the components have been colored, the algorithm checks for necessity of additional closure equations. Normally, the algorithm will find itself in short of one residual equation per closed loop. The user must specify one design parameter for each closed loop. Moreover, in a lot of simulation applications, the expansion device is represented with a simple isenthalpic process without detailed modeling. In this case, we say the expansion device is bypassed. For each bypassed expansion device, the mass flow balance associated with this expansion device is no longer a residual equation, and the user must specify one additional design parameter, such as suction superheat to close the residual equations.

3. Verification and validation of the general-purpose simulation framework

The general-purpose component-based simulation framework proposed in Chapter 2 allows for the simulation of arbitrary vapor compression systems. In this chapter, the simulation framework and the solution methodology is verified/validated with five different test systems. These systems were chosen to represent a wide range of HVAC&R applications. Table 3.1 shows a summary of the test systems.

Table 3.1 Test systems for validation

No.	System	Refrigerant	System capacity	No. of tests	Verification/ validation baseline
1	Reversible heat pump [49]	R410A	10 kW	5	Enthalpy marching solver
2	Dual circuit chiller	R410A	100 kW	4	Experimental data
3	Vapor injection system with economizer [50]	CO_2	11 kW	4	Published test data
4	Transcritical supermarket system [51]	R410A	12 kW	4	Published test data
5	Variable refrigerant flow multi-split system	R410A	10 kW	5	Experimental data

3.1. System descriptions and verification/validation method

3.1.1. Description of the test systems

System 1 (Figure 3.1a) is a R410A-10 kW (3-ton) reversible heat pump. The system consisted of a scroll compressor, a tube-fin outdoor coil and a tube-fin indoor coil. A four-way valve was used to switch between the cooling mode and heating mode. Details about the experimental setup and primary component geometries can be found in [49].

System 2 (Figure 3.1b) is a 100 kW dual circuit chiller. The refrigerant was R410A in both circuits. It should be noted that the proposed simulation framework is perfectly capable to handle different working fluids in different circuits. Each circuit consisted of two parallel scroll compressors, and a tube-fin condenser. The two circuits shared a plate evaporator, with water as the secondary fluid. System 3 (Figure 3.2a) is an 11 kW R410A vapor injection system with economizer. The system consisted of a vapor-injected scroll compressor, a tube-fin indoor coil, a tube-fin outdoor coil, and a plate-type economizer. The experimental setup and primary component details can be found in [50].

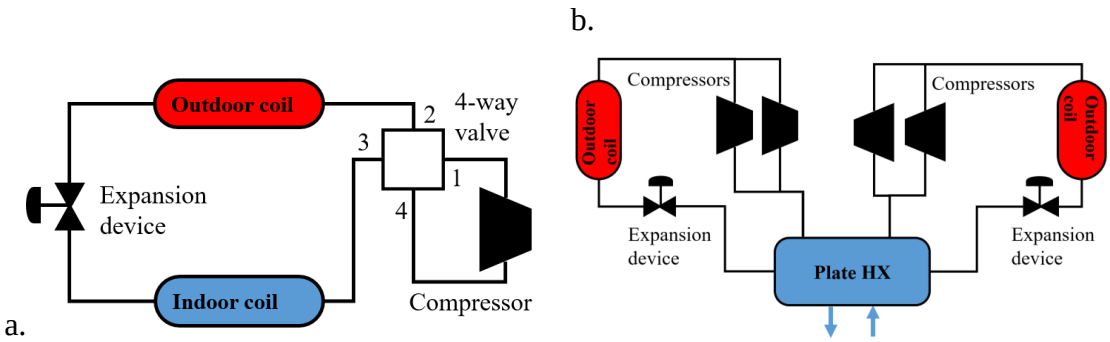

Figure 3.1 Schematic of (a) test system 1; (b) test system 2

System 4 (Figure 3.2b) is a trans-critical supermarket CO_2 system with mechanical subcooler. The system had a variable speed MT compressor, a single speed LT compressor, and a tube-fin gas cooler. Three plate HXs served as the subcooler HX, the MT and LT evaporators, all of which used water-glycol as the secondary fluid. The experimental setup and instrumentation can be found in [51]. The mechanical subcooler system was not simulated. Instead, the subcooler HX was simulated with glycol condition given by the experimental data. In addition, since no details were given about the two suction line HXs, they were disabled in the simulation. System 5 (Figure 3.2c) is a 10 kW

variable refrigerant flow multi-split system. This system has 1 tube-fin outdoor coil, and 4 indoor units. Each indoor unit has an expansion device and a tube-fin indoor coil.

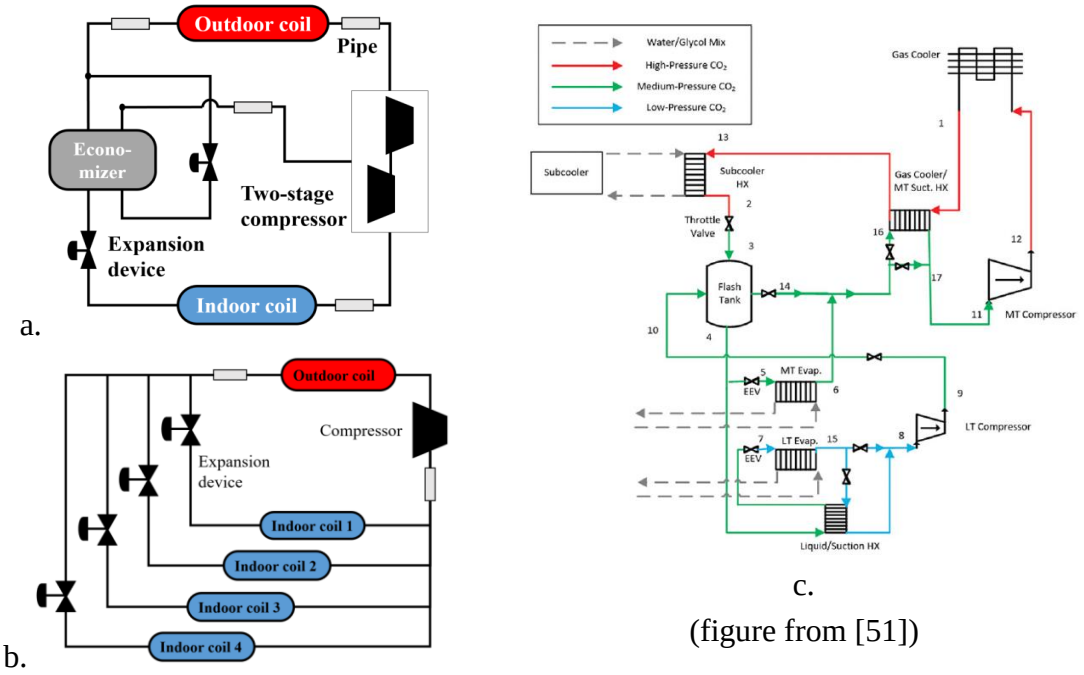

(figure from [51])

Figure 3.2 Schematic of (a) test system 3; (b) test system 4; (c) test system 5

3.1.2.Modeling approaches of the major components

The air-to-refrigerant tube-fin HXs in the test systems were all simulated with the finite-volume air-to-refrigerant HX model by Jiang et al [5]. The fluid-to-fluid plate HXs were simulated with the finite-volume plate HX model by Qiao et al [6]. The only exception was the economizer in system 3. It was modeled with a lump-effectiveness approach. The heat transfer and pressure drop correlations used in the HX models are summarized in Table 3.2 and Table 3.3.

Table 3.2 Heat transfer correlations used in the finite-volume HX modeling

System No.	HX	Type	Refrigerant			Secondary fluid
			Liquid phase	Two-phase	Vapor phase	
1	IC - cooling	Air-to-refrigerant, Tube-fin	Dittus and Boelter, 1985 [52]	Jung et al. 1989 [53]	Dittus and Boelter, 1985 [52]	Wang et al. 1998 [54]
	OC - heating	Air-to-refrigerant, Tube-fin				
	IC - heating	Air-to-refrigerant, Tube-fin		Cavallini et al. 2003 [55]		
	OC - cooling	Air-to-refrigerant, Tube-fin				
2	PHX	Fluid-to-fluid, plate type	Gnielinski, 1976 [56]	Kim et al. 2007 [57]	Gnielinski, 1976 [56]	Kumar, 1984 [58]
	OCs	Air-to-refrigerant, Tube-fin		Shah, 2013 [59]		Kim et al. 1999 [60]
3	IC	Air-to-refrigerant, Tube-fin	Gnielinski, 1976 [56]	Jung et al. 1989 [53]	Gnielinski, 1976 [56]	Wang et al. 1999 [61]
	OC	Air-to-refrigerant, Tube-fin				Kim et al. 1999 [60]
4	Gas cooler	Air-to-refrigerant, Tube-fin	Dittus and Boelter, 1985 [52]	Cavallini et al. 2003 [55]	Dittus and Boelter, 1985 [52]	Bacellar et al. 2014 [62]
	Subcooler HX	Fluid-to-fluid, plate type	Muley and Manglik, 1999 [63]	Yan et al. 1999 [64]	Muley and Manglik, 1999 [63]	Muley and Manglik, 1999 [63]
	MT Evap.	Fluid-to-fluid, plate type	Fixed value	Kim et al. 2007 [57]		
	LT Evap.	Fluid-to-fluid, plate type	Fixed value			

System No.	HX	Type	Refrigerant			Secondary fluid
			Liquid phase	Two-phase	Vapor phase	
5	ICs	Air-to-refrigerant, Tube-fin	Schlager et al. 1989 [65]	Schlager et al. 1989 [65]	Schlager et al. 1989 [65]	Wang et al. 1999 [61]
	OC	Air-to-refrigerant, Tube-fin		Shah, 2016 [66]		Wang et al. 1998 [54]

Table 3.3 Pressure drop correlations used in the finite-volume HX modeling

System No.	HX	Type	Refrigerant			Secondary fluid
			Liquid phase	Two-phase	Vapor phase	
1	IC - cooling	Air-to-refrigerant, Tube-fin	Bhatti, 1987 [67]	Jung and Radermacher, 1989 [68]	Churchill, 1977 [69]	Wang et al. 1998 [54]
	OC - heating	Air-to-refrigerant, Tube-fin				
	IC - heating	Air-to-refrigerant, Tube-fin		Friedel, 1979 [70]		
	OC - cooling	Air-to-refrigerant, Tube-fin				
2	PHX	Fluid-to-fluid, plate type	Muley and Manglik, 1999 [63]	Lockhart and Martinelli, 1949 [71]	Muley and Manglik, 1999 [63]	Ignored
	OCs	Air-to-refrigerant, Tube-fin	Churchill, 1977 [69]	Friedel, 1979 [70]	Churchill, 1977 [69]	Wang et al. 2000 [72]
3	IC	Air-to-refrigerant, Tube-fin	Incropera and DeWitt, 1996 [73]	Jung and Radermacher, 1989 [68]	Incropera and DeWitt, 1996 [73]	Wang et al. 1999 [61]
	OC	Air-to-refrigerant, Tube-fin				Kim et al. 1999 [60]

System No.	HX	Type	Refrigerant			Secondary fluid
			Liquid phase	Two-phase	Vapor phase	
4	Gas cooler	Air-to-refrigerant, Tube-fin	Incropera and DeWitt, 1996 [73]	Koyama et al. 2008 [74]	Incropera and DeWitt, 1996 [73]	Bacellar et al. 2014 [62]
	Subcooler HX	Fluid-to-fluid, plate type	Ignored	Ignored	Ignored	Ignored
	MT Evap.	Fluid-to-fluid, plate type	Ignored	Khan and Chyu, 2010 [75]	Muley and Manglik, 1999 [63]	Ignored
	LT Evap.	Fluid-to-fluid, plate type	Ignored	Ignored	Ignored	Ignored
5	ICs	Air-to-refrigerant, Tube-fin	Schlager et al. 1989 [65]	Schlager et al. 1989 [65]	Schlager et al. 1989 [65]	Wang et al. 1999 [61]
	OC	Air-to-refrigerant, Tube-fin		Koyama and Yonemoto, 2006 [76]		Wang et al. 1998 [54]

The compressors in system 1, 2, 5, and the LT compressor in system 4 were represented by 10-coefficient performance map. The regression coefficients in the polynomial equations were provided by respective compressor manufacturers. The two-stage compressor in system 3 was modeled with a hybrid approach. The 1st and 2nd stage efficiencies were curve fitted with 4 sets of coefficients. These coefficients can be found in [77]. The expansion devices in all 5 test systems were bypassed. They were represented with isenthalpic process without detailed simulation.

3.1.3.Validation approach

For each system, we used the solution methodology (as described in section 2.4) to determine the mathematical formulation for each system. The method presented in Section 2.4.1 was used to determine the system flow directions. The tearing algorithm presented in Section 2.4.3 was applied to determine the component execution order, and to formulate the system of equations that describe the system steady state at various conditions. The formulated equations were delegated to the Broyden iteration scheme [78] to obtain the steady-state solutions.

The 5 test systems had different baselines to validate their equation formulations. For system 1, the enthalpy marching solver [4] was the verification baseline. The simulation results of system 2, 3, 4, 5a were validated with respective experimental data.

Simulation energy imbalance, system performance deviation, and saturated temperature difference were used to evaluate the simulation results. Simulation energy imbalance serves to assess the simulation convergence and indicate whether the numerical solution is a closed loop. It is defined as

$$\Delta_E = \frac{Q_{indoor} + Q_{outdoor} + W_{comp}}{\left|W_{comp}\right|} \tag{7}$$

in which the capacities and compressor work follow the sign convention of energy and work transfer that energy transferred out of a component is positive, and work done by a component is positive. It is worth noting that the W_{comp} in the equation does not account for power consumption due to mechanical loss. The system performance deviation is defined as

$$\delta_Y = \frac{Y - Y_{baseline}}{Y_{baseline}} \tag{8}$$

where Y stands for system COP, power consumption, or system capacity. $Y_{baseline}$ is the system performance from the baseline results. Saturated temperature difference is given by

$$\Delta T = T - T_{baseline} \tag{9}$$

where T stands for saturated temperatures such as SST and SDT. This temperature difference measures the deviation between the simulated pressure level and that from the baseline. For the transcritical system, pressure difference is used, which is

$$\delta_P = P - P_{baseline} \tag{10}$$

For thermodynamic property calculation, NIST REFRPOP data library [79] was used, augmented with curve-fits as described in [80].

3.2. *Verification and validation Results*

This section presents the validation results of the proposed solution methodology. For each test system, we first present the equation formulation determined by the solution methodology, including the system flow directions, corresponding equation set, as well as the number of additional design criteria required to close the equation. Then we present the convergence index, and the comparison of the simulation results and respective baseline results at a series of test conditions.

The main focus of the validation is to test the mathematical viability of the equation set determined by the algorithm: whether or not it can reach convergence and reasonable numerical results by the most commonplace nonlinear equation iteration scheme. Component model accuracy improvement, such as coefficient tuning and calibration, is not within the scope of this validation work.

3.2.1. System 1: Reversible heat pump

3.2.1.1. Equation formulation

This system is the most basic configuration of vapor compression systems. Figure 3.3 shows the system schematic as a network of components with the two boundary conditions. The four-way valve in the system has two operating modes, and thus can switch the mode of the system. We used mass flow sign propagation to determine the system flow directions, which are also shown in Figure 3.3. In the cooling mode, the four-way valve directs the refrigerant flow from port 1 to 2, and from port 3 to 4. Thus, the outdoor HX serves as the condenser, and the indoor HX serves as the evaporator. In the heating mode, the refrigerant in the four-way valve is flowing from port 1 to 3, and from port 2 to 4, so that the functions of the two HXs are reversed.

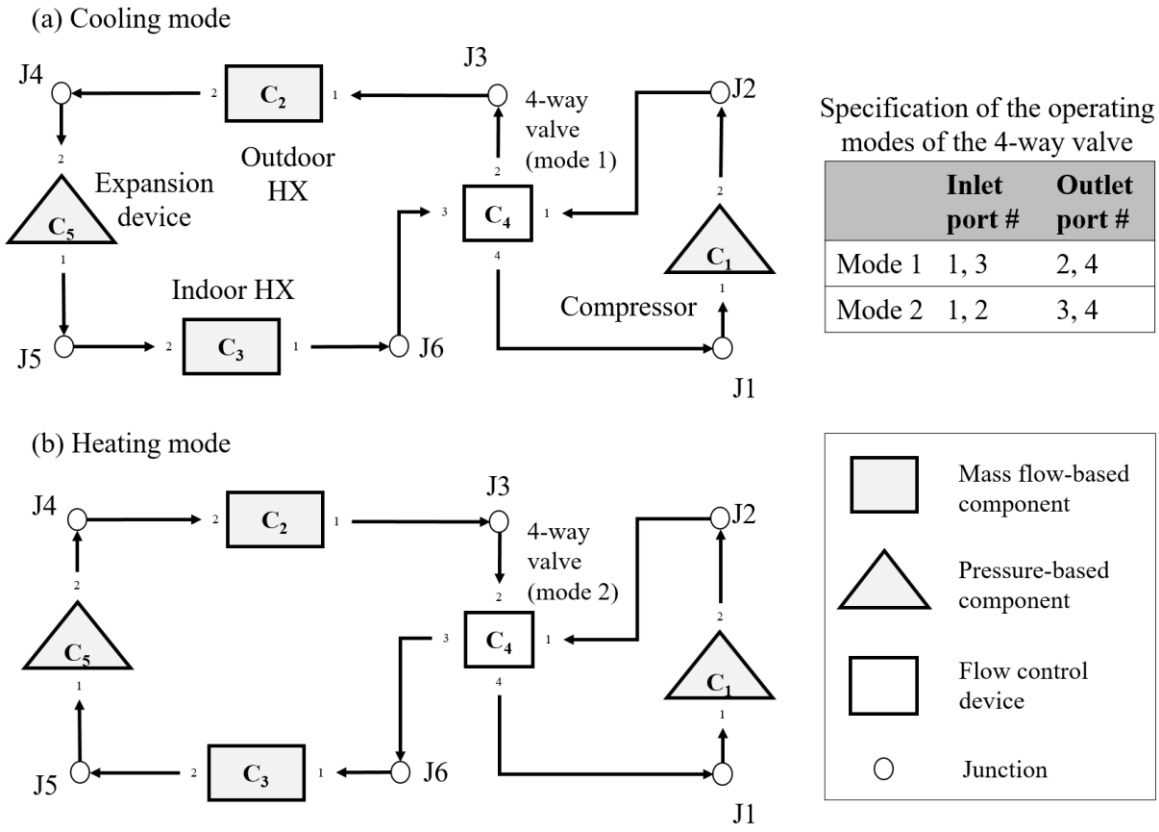

Figure 3.3 Component-based representation schematic with flow directions of System 1 - Reversible heat pump

After the system flow directions were determined, the tearing variables and residual equations were then determined by the tripartite graph tearing algorithm. They are given in Table 3.4. In the subscripts, the two digits represent the component ID, and the port ID, respectively, e.g., $P_{1,2}$ means the pressure of port 2 of component C_1. The component execution order is very straightforward in this case. It is simply along the refrigerant flow direction. As noted in section 3.1.2, the expansion device was bypassed in the simulation. Therefore, two design criteria are required to close the equations in both the cooling mode and the heating mode.

Table 3.4 Tearing variables and residual equations for System 1 - Reversible heat pump

No.	Cooling mode		Heating mode	
	Tearing variable	Residual equation	Tearing variable	Residual equation
1	$P_{1,1}$	$P_{1,1} = P_{4,4}$	$P_{1,1}$	$P_{1,1} = P_{4,4}$
2	$h_{1,1}$	$h_{1,1} = h_{4,4}$	$h_{1,1}$	$h_{1,1} = h_{4,4}$
3	$P_{1,2}$	Design criterion 1	$P_{1,2}$	Design criterion 1
4	$P_{5,1}$	Design criterion 2	$P_{5,2}$	Design criterion 2

3.2.1.2. Simulation conditions and results verification

The simulation conditions followed the AHRI Standard 210/240 (2017), as shown in Table 3.5. Compressor suction superheat and expansion device inlet subcooling were chosen as the system design criteria, and they were set to be 10 K and 5 K for all 5 simulation conditions.

Table 3.5 Simulation conditions for System 1 - Reversible heat pump (AHRI Standard 210/240 [81])

Mode	Test name	Indoor ambient temperature (°C)		Outdoor ambient temperature (°C)	
		T_{db}	T_{wb}	T_{db}	T_{wb}
Cooling	A	26.7	19.4	35	23.9
	B	26.7	19.4	27.8	18.3
Heating	H1	21.1	15.6	8.3	6.1
	H2	21.1	15.6	1.7	0.6
	H3	21.1	15.6	-8.3	-9.4

For this system, the results by the enthalpy marching solver were used as the verification baseline. Table 3.6 shows the verification summary, which includes the simulation energy imbalance, system performance deviation, and the saturation temperature difference from the baseline results. The definitions for these three are given

in section 3.1.3. The verification results show good convergence and that the current approach was able to reproduce the baseline simulation results.

Table 3.6 Verification summary of System 1- Reversible heat pump simulation

Test Name	Δ_E (%)	System performance deviation δ (%)			Saturated temperature difference ΔT (K)	
		COP	Q	W	SDT	SST
A	0.01	-0.05	0.06	0.11	-0.05	0.0
B	0.05	-0.03	0.08	0.11	-0.05	0.0
H1	0.00	0.03	0.10	0.06	-0.02	0.0
H2	0.00	0.02	0.09	0.06	-0.02	0.0
H3	0.00	0.03	0.10	0.05	-0.03	0.0

3.2.1.3. Simulation with alternative design criteria

The simulation results in the previous section were obtained using superheat and subcooling as the design criteria. To demonstrate the flexibility of the solution method, we simulated the reversible heat pump with alternative design criteria, as shown in Table 3.7.

Table 3.7 Alternative design criteria for System 1 simulation

Test No.	Test Condition	Expansion device component model	Design criterion 1	Design criterion 2
1	A	Pressure based component	SC = 5 K	NA
2	A	Pressure based component	SH = 10 K	NA
3	H1	Bypassed	Charge = 1.649 kg	SH = 10 K
4	H1	Bypassed	Charge = 1.649 kg	SC = 5 K
5	H1	Bypassed	SH = 10 K	SC = 5 K

In test 1 and 2, AHRI A cooling test (Table 3.5) was used as the simulation condition. Expansion device was modeled as a pressure based component, and thus the system of

equations requires only 1 design criterion. We chose subcooling and superheat, respectively, to be the design criterion in these 2 tests. In test 3 - 5, AHRI H1 heating test (Table 3.5) was used. Expansion device was bypassed, and resulted in the requirement for 2 design criteria. System total charge was used as one of them, in addition to either superheat or subcooling. Test 5 used the same design criteria (superheat and subcooling) as the previous section, in which the system charge was calculated to be 1.649 kg. Therefore, we used this value in test 3 and 4.

Simulation results with alternative design criteria are shown in Table 3.8. The results show good convergence for all the tests, and evidence the flexibility of the proposed solution methodology in terms of the selection of design criteria. When the expansion device is modeled, the user may choose either superheat or subcooling as the design criterion. Moreover, results of test 3 to 5 show excellent consistency. When the user selects any two criteria from SH, SC, and charge, the simulation results are identical.

Table 3.8 Simulation results of System 1 with alternative design criteria

Test No.	Test Condition	Design criteria	Δ_E (%)	COP	Q	W	P_{dis}	P_{suc}
1	A	SC	-0.07	4.442	11023	2482	2.707	1.141
2	A	SH	0.03	4.411	10826	2455	2.678	1.136
3	H1	Charge and SH	0.00	4.731	9701.2	2050	2.155	0.755
4	H1	Charge and SC	0.00	4.731	9701.4	2050	2.155	0.755
5	H1	SH and SC	0.00	4.731	9701.2	2050	2.155	0.755

3.2.2.System 2: Dual-circuit chiller

3.2.2.1.Equation formulation

Figure 3.4 shows the component-based representation of this system with the flow directions. Since the two parallel scroll compressors in each circuit/fluid loop shared the same inlet and outlet conditions, we simplified them into one single component of compressor rack. Therefore, this system ended up with only two alternating base configurations, No. 1 and 2 from Table 2.2. The plate HX was represented with a mass flow-based component with two fluid groups, each has an inlet port and an outlet port. The definitions for a *fluid loop (or circuit)* and a *fluid group* is specified in section 2.1.2. Although the system has two fluid loops, only the plate HX has two fluid groups, while all the other components have one fluid group.

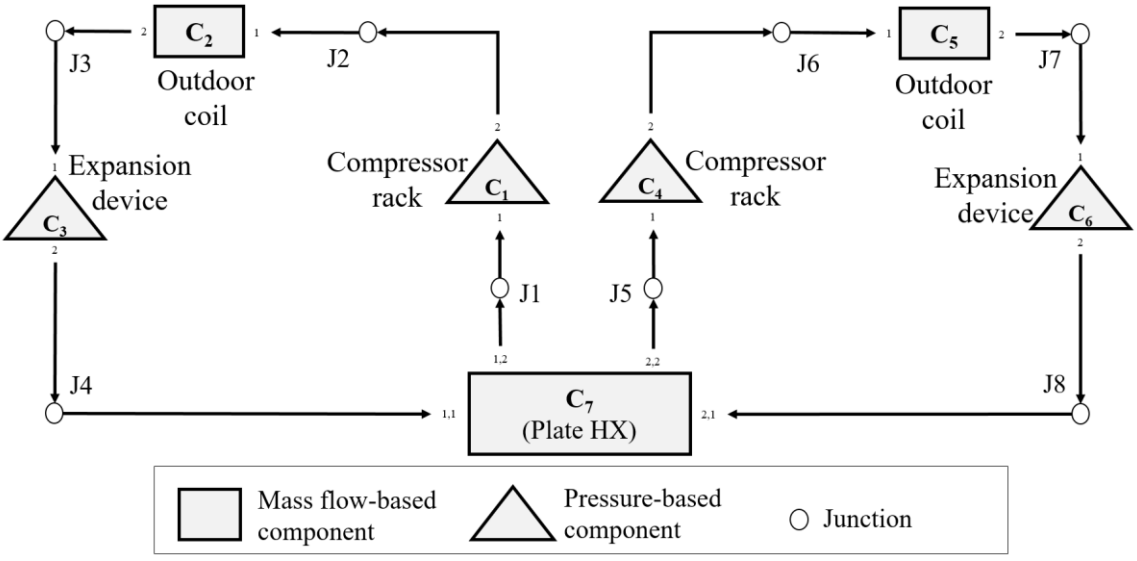

Figure 3.4 Component-based representation schematic with flow directions of System 2 - Dual circuit chiller

Similar to system 1, the component execution order also follows the refrigerant flow in this system. The only difference from simulating two independent circuits is that, since

the plate HX (C_7) couples the two circuits, it cannot be executed until $C_1 – C_6$ are all executed. Table 3.9 shows the tearing variables and residual equations determined by the tripartite graph tearing algorithm. For 3-digit subscripts, the three digits represent the component ID, the fluid group ID, and the port ID, respectively. Two design criteria are required for each circuit because of the bypassed expansion devices.

Table 3.9 Tearing variables and residual equations for System 2 - Dual circuit chiller

No.	Tearing variable	Residual equation	No.	Tearing variable	Residual equation
1	$P_{1,1}$	$P_{1,1} = P_{7,1,2}$	5	$P_{4,1}$	Design criterion 1: circuit 1 SH
2	$h_{1,1}$	$h_{1,1} = h_{7,1,2}$	6	$h_{4,1}$	Design criterion 2: circuit 1 SC
3	$P_{1,2}$	$P_{4,1} = P_{7,2,2}$	7	$P_{4,2}$	Design criterion 3: circuit 2 SH
4	$P_{3,2}$	$h_{4,1} = h_{7,2,2}$	8	$P_{6,2}$	Design criterion 4: circuit 2 SC

3.2.2.2. Simulation conditions and results validation

Table 3.10 shows the simulation conditions, which includes 100, 75, 50, and 25 percent load. The number of active compressors in each circuit were adjusted according to the load condition. The indoor water temperatures and outdoor air temperatures were kept the same as those in the experiment. The compressor suction superheat and expansion device inlet subcooling in each circuit were chosen as the system design criteria, and they were also set to be the experimental values at corresponding simulation conditions.

Table 3.10 Simulation conditions for System 2: Dual circuit chiller

Load (%)	No. active compressors		Indoor EWT(°C)	Indoor LWT (°C)	Outdoor ambient temperature (°C)
	Circuit 1	Circuit 2			

100	2	2	11.9	6.9	35
75	2	1	9.0	5.0	30.3
50	1	1	17.3	15.2	24.9
25	1	0	16.3	15.3	25.0

Table 3.11 shows the validation summary of the system simulation results. The results show that the maximum value of energy imbalance was 0.57%. The simulated power consumption and capacities were within $\pm 5\%$ deviation compared to the experimental data. The maximum saturation temperature difference was at circuit 2 SST at 75% load, which showed 1.95 K higher than the measured data.

Table 3.11 Validation summary of System 2 - Dual circuit chiller simulation

Load (%)	Δ_E (%)	System performance deviation δ_Y (%)			Saturated temperature deviation ΔT (K)			
		COP	Q	W	SDT_1	SDT_2	SST_1	SST_2
100	-0.03	-0.77	2.53	3.32	-0.99	-1.62	0.27	0.36
75	0.57	3.48	3.41	-0.06	-1.83	-0.53	0.36	1.95
50	0.23	-7.04	-4.39	2.84	-1.31	-1.34	0.39	0.54
25	0.01	-8.94	-4.44	4.93	-1.69	NA	-1.19	NA

3.2.3.System 3: Two-stage vapor injection system using economizer

3.2.3.1.Equation formulation

Figure 3.5 shows the component-based system representation with flow directions. The system contains base configurations No.1 (J1, J8, J9), No.2 (J2, J6, J10), No.3 (J3, J4, J7, J11) and No.7 (J5). These base configurations can be referred to Table 2.2. The economizer (C_5) is a mass flow-based component with 2 inlets and 2 outlets. Unlike the plate HX in system 2, these 4 ports belong to the same fluid group. Therefore, the internal flow paths (port mapping) must be specified within the component model.

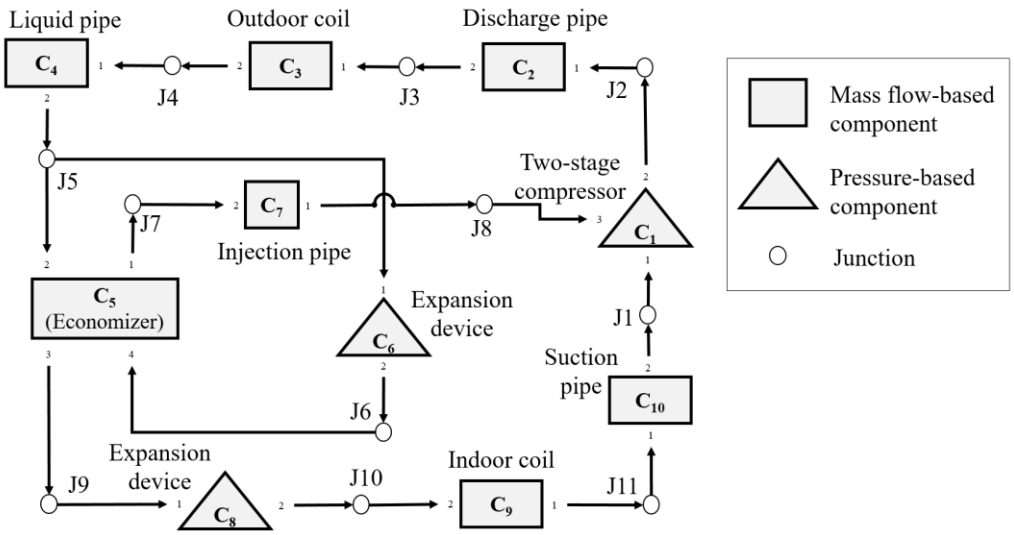

Figure 3.5 Component-based representation with flow directions of System 3 - Vapor injection system

Table 3.12 shows the corresponding tearing variables and residual equations. Variables 1-5 were the boundary conditions of C_1, which was a pressure-based component with 2 inlets and 1 outlet. Variable 6 was due to the splitting junction J5 and the fact that C_6 was a bypassed pressure component. Variable 7 and 8 were the outlet pressures of the two pressure-based components, C_6 and C_8. Equation 1, 2, 4 and 5 were required to ensure that the system would form a closed thermodynamic cycle. Equation 3 ensures that the splitting ratio at J5 would be consistent with the compressor injection ratio. To close the system of equations, we need 3 additional design criteria. For this system, these 3 criteria can also be regarded as the high-side, intermediate, and low-side convergence criterion.

Table 3.12 Tearing variables and residual equations for System 3 - Vapor injection system

No.	**Tearing variable**	**Residual equation**	**No.**	**Tearing variable**	**Residual equation**
1	$P_{1,1}$	$P_{1,1} = P_{10,1}$	5	$P_{1,2}$	$h_{1,3} = h_{7,1}$

No.	Tearing variable	Residual equation	No.	Tearing variable	Residual equation
2	$h_{1,1}$	$h_{1,1} = h_{10,1}$	6	$\dot{m}_{6,1}$	Design criterion 1: suction SH
3	$P_{1,3}$	$\dot{m}_{1,1} = \dot{m}_{10,2}$	7	$P_{6,2}$	Design criterion 2: compressor discharge T
4	$P_{1,3}$	$P_{1,3} = P_{7,1}$	8	$P_{8,2}$	Design criterion 3: injection ratio

3.2.3.2. Simulation conditions and results validation

The simulation condition was at a high ambient temperature of 46.1 °C. It is one of the test conditions selected by the original research [50], and it best reflects the motivation of using two-stage system in the extreme climate. The indoor dry-bulb and wet-bulb temperatures were 26.7 and 19.4 °C. The injection ratio was defined as the ratio of injected mass flow rate and the suction mass flow rate. We simulated the system at various injection ratios ranging from 0.055 to 0.278. The three design criteria were suction superheat, discharge temperature, and the injection ratio. They were set to be equal to the experimental values.

Figure 3.6 compares the simulated and experimental system performance and mass flow rates at various injection ratios, and shows a good agreement between the two. Table 3.13 shows the energy imbalance and the saturation temperature difference at different conditions.

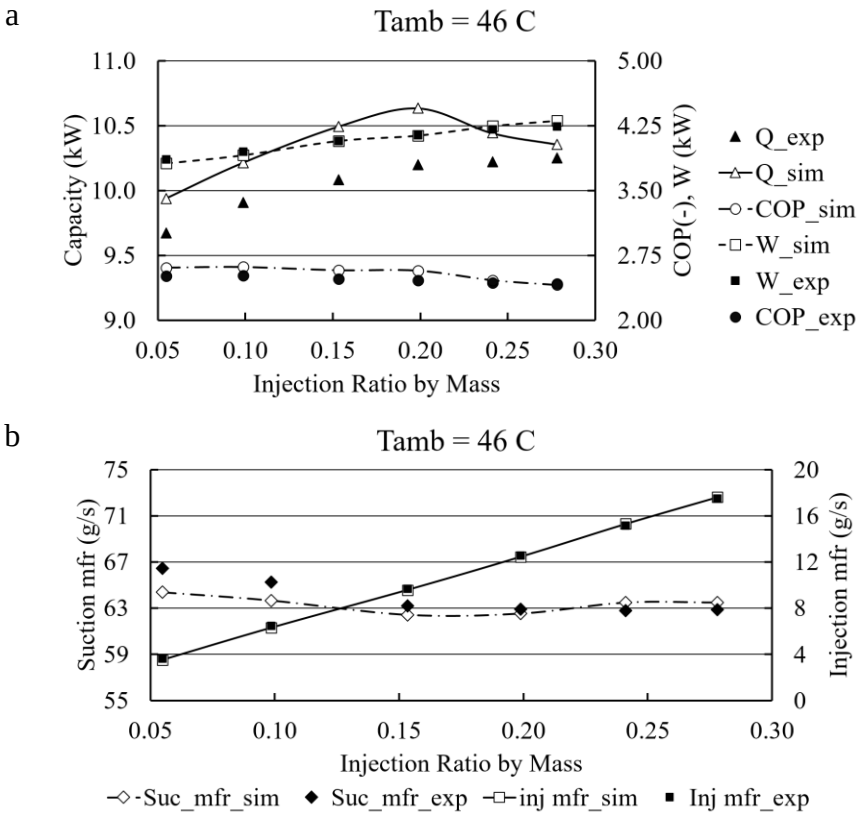

Figure 3.6 Simulation results validation on: (a) system performance, (b) mass flow rates

Table 3.13 Energy imbalance and saturation temperature difference for System 3 - Vapor injection system simulation

Injection Ratio	Δ_E (%)	Saturated temperature deviation ΔT (K)		
		SDT	SST	SIT
0.055	0.01	-0.81	-0.3	-1.49
0.099	-0.13	-0.69	-0.23	-0.5
0.153	-0.01	-0.69	-0.01	0.26
0.199	0.03	-0.97	0.01	0.00
0.241	0.01	-1.44	0.27	0.01
0.278	-0.01	-1.47	0.36	0.01

3.2.4.System 4: Trans-critical supermarket CO_2 system

3.2.4.1.Equation formulation

Figure 3.7 shows the component-based representation of the system. It is simplified from the original system schematic, because the subcooler system was not simulated, and the two suction line HXs were not in effect in the simulation. The system contains base configurations No. 1(J1, J4, J6, J13), No. 2 (J2, J9, J10, J11), No. 3 (J3, J12), No. 5 (J8), and No. 10 (J5, J7) from Table 2.2.

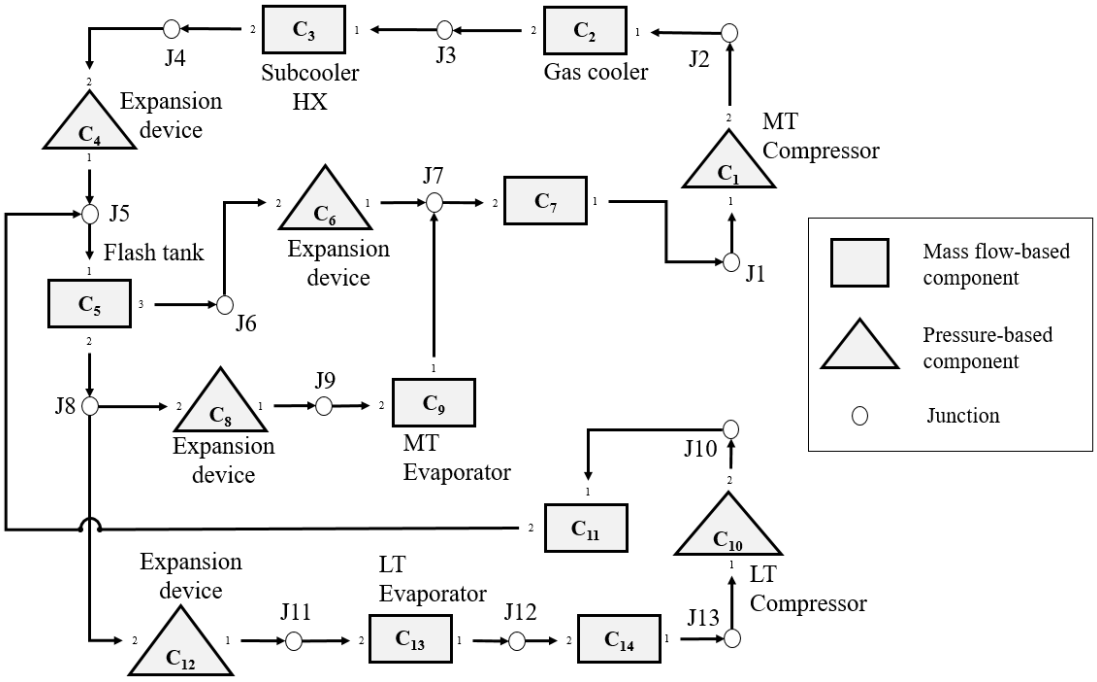

Figure 3.7 Component-based representation schematic with flow directions of System 4 - Trans-critical CO_2 system

As shown by Table 3.14, the two compressors (C_1 and C_{10}) lead to variables 1-6. Since C_8 and C_{12} were bypassed expansion devices, one of the mass flow rates after the splitting junction J_8 was the 7^{th} tearing variable. The last two were the outlet pressure of the pressure-based components C_8 and C_{12}. Equation 1, 2, 4 and 5 ensured that the solution was closed thermodynamically. Equation 3 ensured that the variable 7

corresponded to the LT compressor mass flow rate. Apart from these, 4 design criteria were required to close the equations.

Table 3.14 Tearing variables and residual equations for System 4 - Trans-critical CO_2 system

No.	Tearing variable	Residual equation	No.	Tearing variable	Residual equation
1	$P_{1,1}$	$P_{1,1} = P_{7,1}$	6	$P_{10,2}$	Design criterion 1: discharge P at J2
2	$h_{1,1}$	$h_{1,1} = h_{7,1}$	7	$\dot{m}_{8,2}$	Design criterion 2: expansion device C_6 outlet x
3	$P_{1,2}$	$\dot{m}_{10,1} = \dot{m}_{14,1}$	8	$P_{8,1}$	Design criterion 3: MT evaporator C_9 outlet SH
4	$P_{10,1}$	$P_{10,1} = P_{14,1}$	9	$P_{12,1}$	Design criterion 4: LT evaporator C_{13} outlet SH
5	$h_{10,1}$	$h_{10,1} = h_{14,1}$			

3.2.4.2. Simulation conditions and results validation

We selected 4 out of 11 test points in [51] as the simulation conditions. Two of them had the subcooler system turned on, two of them off. Table 3.15 shows the temperature specifications at each condition, and their respective original test numbers. We used the same set of convergence criteria as in [51]: MT compressor discharge pressure, expansion device outlet quality at J7, and superheat at the outlet of MT and LT evaporators. Their values were set to be the experimental values at the corresponding testing conditions.

Table 3.15 Simulation conditions for System 4 - trans-critical CO2 system

Test No.	**Original Test No. in** [51]	**Outdoor T_{db} (K)**	**Subcooler EWT**	**MT Evap. EWT**	**LT Evap. EWT**
1	2	312.3	302.4	280.3	277.2

Test No.	**Original Test No. in** [51]	**Outdoor T_{db} (K)**	**Subcooler EWT**	**MT Evap. EWT**	**LT Evap. EWT**
2	6	289.1	288.8	279.7	277.6
3 (no sub)	9 (no sub)	308.0	302.4	278.4	277.4
4 (no sub)	11 (no sub)	289.3	302.4	278.0	277.5

Table 3.16 shows the validation summary. The simulated system performance shows small deviation from the measured data. Since test 1, 2, and 3 were all transcritical conditions, we reported the pressure difference instead of the saturation temperature difference from the measured data. Four pressure levels were compared: MT compressor discharge pressure P_{J2}, flash tank pressure P_{J5}, MT evaporator pressure P_{J9}, and LT evaporator pressure P_{J11}. In test 2, the simulated pressure at J11 (LT evaporator pressure) is 121kPa higher than the experiment pressure (1.44 MPa [51]), which is roughly 8% deviation with respect to the measured value. In test 4, the normalized energy balance was 0.91% and was highest among the 4 tests. This could be due to the nonlinearity of the HX models at this condition.

Table 3.16 Validation summary of System 4 - Trans-critical CO_2 system simulation

Test No.	Δ_E (%)	System performance deviation δ_Y (%)			Pressure difference δ_P (kPa)			
		Y = COP	Y = Q	Y = W	P_{J2}	P_{J5}	P_{J9}	P_{J11}
1	0.22	0.56	1.14	0.58	2.08	-3.87	55.81	76.54
2	0.39	0.67	1.26	0.58	1.88	-16.24	1.77	121.16
3	0.57	-0.90	-0.41	0.49	4.27	-0.23	-4.29	3.04
4	0.91	-0.82	0.34	1.17	-2.98	42.48	44.91	-0.94

3.2.5.System 5: VRF multi-split system

3.2.5.1.Equation formulation

Figure 3.8 shows the component-based representation of the system. It contains base configurations No.1 (J1), No.2 (J2, J5, J7, J8, J9), No.3 (J3), No.5 (J4) and No.9 (J6). The component execution follows the refrigerant flow direction. Table 3.17 shows the corresponding tearing variables and residual equations. Variables 1-3 were the boundary conditions of C_1. Variable 4-6 were due to the splitting junction J4 and the fact that C_4, C_6, C_8, and C_{10} were bypassed pressure components. The remaining variables were the outlet pressures of the pressure-based components. Equation 1 and 2 ensure that the system was closed thermodynamically. Equation 3-5 ensure that the splitting ratios at J4 would result in pressure balance at the merging junction J6. To close the equations, we need 5 additional design criteria.

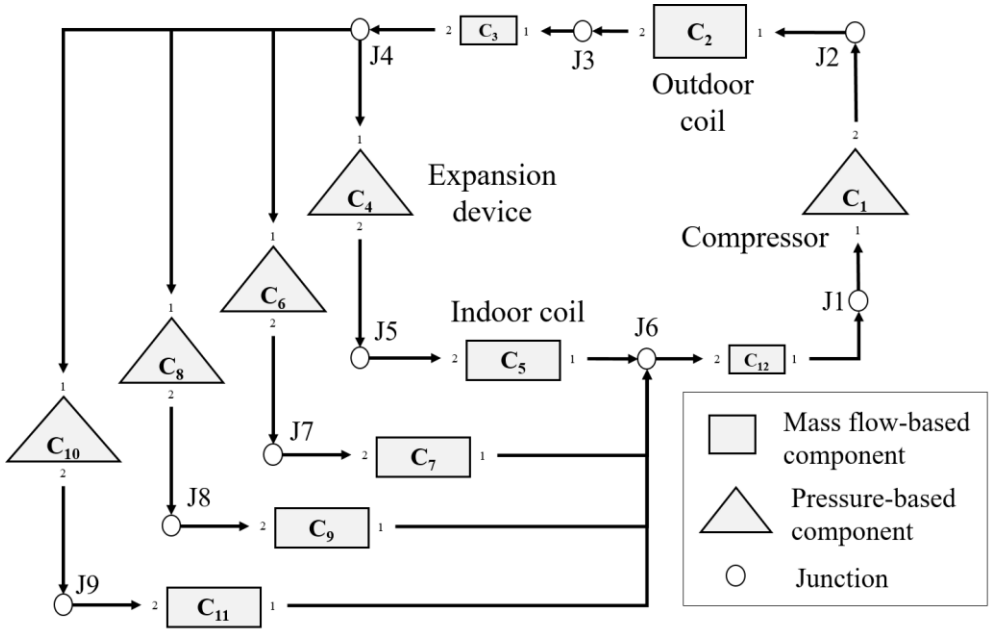

Figure 3.8 Component-based representation schematic with flow directions of System 5 - VRF multi-split system

Table 3.17 Tearing variables and residual equations for System 5 - VRF-multi split system

No.	Tearing variable	Residual equation	No.	Tearing variable	Residual equation
1	$P_{1,1}$	$P_{1,1} = P_{12,1}$	6	$\dot{m}_{8,1}$	Design criterion 1: SC at J3
2	$h_{1,1}$	$h_{1,1} = h_{12,1}$	7	$P_{4,2}$	Design criterion 2: indoor coil C_5 outlet SH
3	$P_{1,2}$	$P_{5,1} = P_{7,1}$	8	$P_{6,2}$	Design criterion 3: indoor coil C_7 outlet SH
4	$\dot{m}_{4,1}$	$P_{5,1} = P_{9,1}$	9	$P_{8,2}$	Design criterion 4: indoor coil C_9 outlet SH
5	$\dot{m}_{6,1}$	$P_{5,1} = P_{11,1}$	10	$P_{10,2}$	Design criterion 5: indoor coil C_{11} outlet SH

3.2.5.2. Simulation conditions and results validation

The system was simulated at 5 different outdoor temperatures, as shown in Table 3.18. The compressor speed were adjusted according to the outdoor ambient temperature. In all 5 test conditions, the indoor temperatures were kept constant at 26.7/19.4 °C. We used the subcooling at J4 and the indoor coil outlet superheat as the design criteria. There were 4 indoor coils, and thus the 4 individual superheat specifications, together with the subcooling, fulfilled the requirement of 5 design criteria. The superheat and subcooling values are given in Table 3.18. The superheat value was the same for all 4 indoor coils.

Table 3.18 Simulation conditions for System 5 - VRF multi-split system

Test No.	**Compressor speed**	**Outdoor ambient temperature (°C)**		**SC (K)**	**Indoor coil outlet SH (K)**
		T_{db}	**T_{wb}**		
1	Max	35	23.9	1.56	7.61
2	Max	27.8	18.3	0.28	6.95
3	Intermediate	30.6	20.6	0.81	7.03

Test No.	**Compressor speed**	**Outdoor ambient temperature (°C)**		**SC (K)**	**Indoor coil outlet SH (K)**
		T_{db}	**T_{wb}**		
4	Min	27.8	18.3	3.04	7.67
5	Min	19.4	11.9	3.86	7.54

Table 3.19 shows the validation summary of the system simulation results. The simulation of all 5 tests was well converged, showing small energy imbalance. The simulated system performance were within $\pm$ 10% deviation from the experimental data. The maximum saturation temperature deviation was 1.66 K.

Table 3.19 Validation summary of System 5 - VRF multi-split system simulation

Test No.	Δ_E (%)	System performance deviation δ_Y (%)			Saturated temperature deviation ΔT (K)	
		Y = COP	Y = Q	Y = W	SDT	SST
1	-0.03	1.44	3.59	2.12	1.14	1.26
2	0.03	0.99	2.10	1.10	1.62	1.55
3	-0.01	4.13	7.23	2.98	1.62	-0.23
4	0.01	4.26	7.16	2.78	1.04	-0.22
5	-0.09	6.72	5.97	-0.70	1.66	1.48

3.3. Summary

This chapter validated the general-purpose simulation framework with 5 different test systems. The capacities of the test systems range from 10 to 100 kW. Residual equations were formulated for each system, and they were solved under various conditions. The verification and validation of the 5 test systems are summarized in Table 3.20. For each test system, the table shows the maximum energy imbalance, the maximum system performance deviation (in terms of the absolute value), and computational time over all

the test conditions. For system 2, the maximum COP deviation was 8.94%. This was because the simulated Q was under-estimated while W was over-predicted. Figure 3.9 shows the comparison between the simulation and experimental data for system 2, 3, 4 and 5.

Table 3.20 Verification and validation summary of the 5 test systems

No.	System	No. of test conditions	Max $\|\Delta_E\|$ (%)	Max $\|\delta_Y\|$ (%)	Computational time (s)
1	R410A reversible heat pump	5	0.05	0.11 (Y=W)	2 – 4
2	R410A dual circuit chiller	4	0.57	8.94 (Y=COP)	3 – 4
3	R410A vapor injection system with economizer	6	0.13	4.4 (Y = COP)	48 – 851
4	Trans-critical CO_2 supermarket system	4	0.91	1.26 (Y = Q)	5 – 14
5	VRF multi-split system	5	0.09	7.23 (Y=Q)	94 – 375

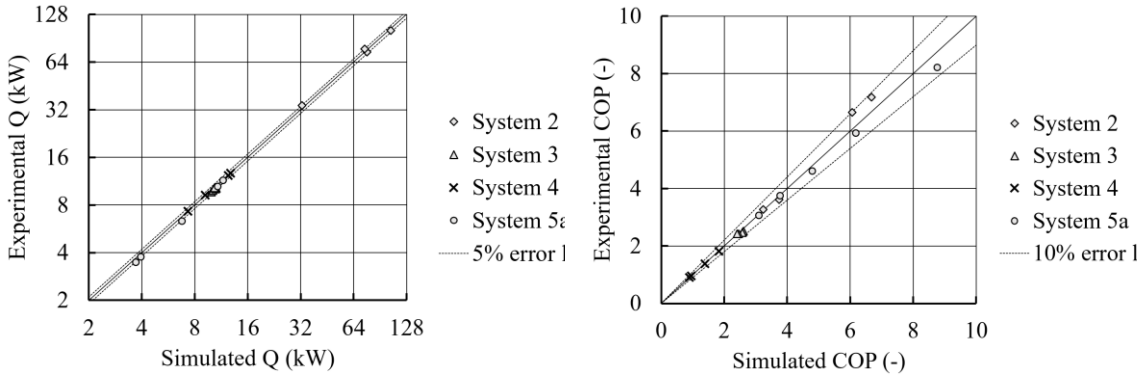

a b

Figure 3.9 Comparison between the simulation and experimental data: (a) system capacity; (b) COP

By reducing the vapor compression system into 10 base configurations, the solution methodology proposed in the Chapter 2 can systematically determine the system flow directions, formulate the residual equation set, and identify the lack of closure equations for arbitrary system configurations. The simulation results show that the equation formulation by the methodology presented good mathematical viability for a wide variety of system configurations. The comparison against the experimental data at various test conditions shows that the equation set could result in reasonable numerical solution within acceptable deviation range.

4. Steady-state analysis of advanced systems

In Chapter 3, the general-purpose simulation framework and solution methodology has been extensively validated with five test systems. While they represent a wide range of HVAC&R applications, these systems are conventional systems that have achieved substantial market penetration in the residential or commercial sectors.

In this Chapter, the extensively validated solution methodology is applied to analyze two complex systems: a variable refrigerant flow (VRF) heat recovery system, and a simultaneous vapor and liquid injection system. As opposed to the conventional systems in Chapter 3, these advanced systems are still in the early R&D stage, and have not been widely applied. And thus validation data is extremely limited. Therefore, the main focus of this Chapter is to show that the general-purpose simulation framework can reliably contributes to the performance evaluation of the advanced systems and the acceleration of their R&D stage.

4.1. Simulation of VRF heat recovery system

As one of the latest emerging HVAC&R technologies, the variable refrigerant flow (VRF) system with heat recovery has obtained extensive attention. Compared with the conventional VRF-multi split systems, VRF heat recovery system can provide simultaneous cooling and heating operations, and thus lead to substantial energy saving potential and more flexible zonal control [82].

In this section, a VRF heat recovery system and its performance evaluation at various operating modes are presented. Figure 4.1 shows the system schematic. The reference of the system configuration is [82]. It has 3 dedicated refrigerant pipes and 3 four-way

valves to enable 6 operating modes. They include a cooling-only mode, a heating mode, and 4 simultaneous-heating-cooling modes. Since the reference did not provide information about the major components, the HXs of the reversible heat pump in section 3.2.1 was used for this system. The HX component model, and the correlation specifications are the same as in the reversible heat pump simulation. The compressor was represented with an efficiency based model, with a volumetric efficiency of 0.95, isentropic efficiency of 0.7, and displacement of 92.5 cc. The expansion device modeling in this system was bypassed, and was instead represented with an isenthalpic process.

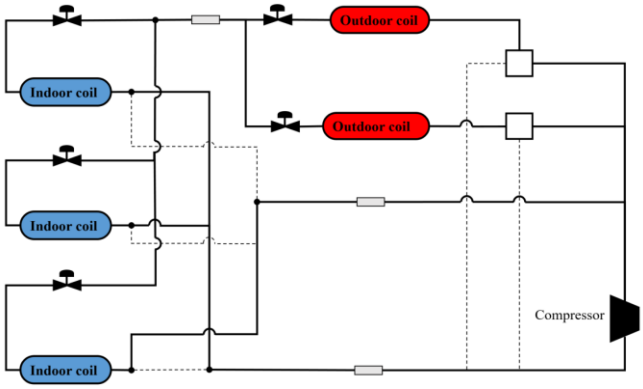

Figure 4.1 Schematic of the VRF heat recovery system

4.1.1.Equation formulation

For demonstration purpose, this system was simulated at 3 different operating modes: cooling only, heating only and simultaneous heating and cooling. Figure 4.2 shows the component-based representation and the corresponding flow directions at cooling-only mode. Only major splitting and merging junctions are displayed in the figure. There were 11 check valves, all labeled with a separate series of IDs in the figure, to vary the flow directions in the HXs and thus to enable mode switching. For cooling-only mode, 5 check valves were enabled (CKV 2, 3, 4, 6, 8), while the other 6 were disabled from the system. Since the 2 outdoor coils served as the condenser, the two expansion devices (EXV 1, 2)

immediately after the outdoor coils were disabled. So the refrigerant would flow through the dummy pipes, C_{28} and C_{29}, instead. Table 4.1 shows the on-off logics of the check valves and expansion valves in the other two operating modes in the simulation.

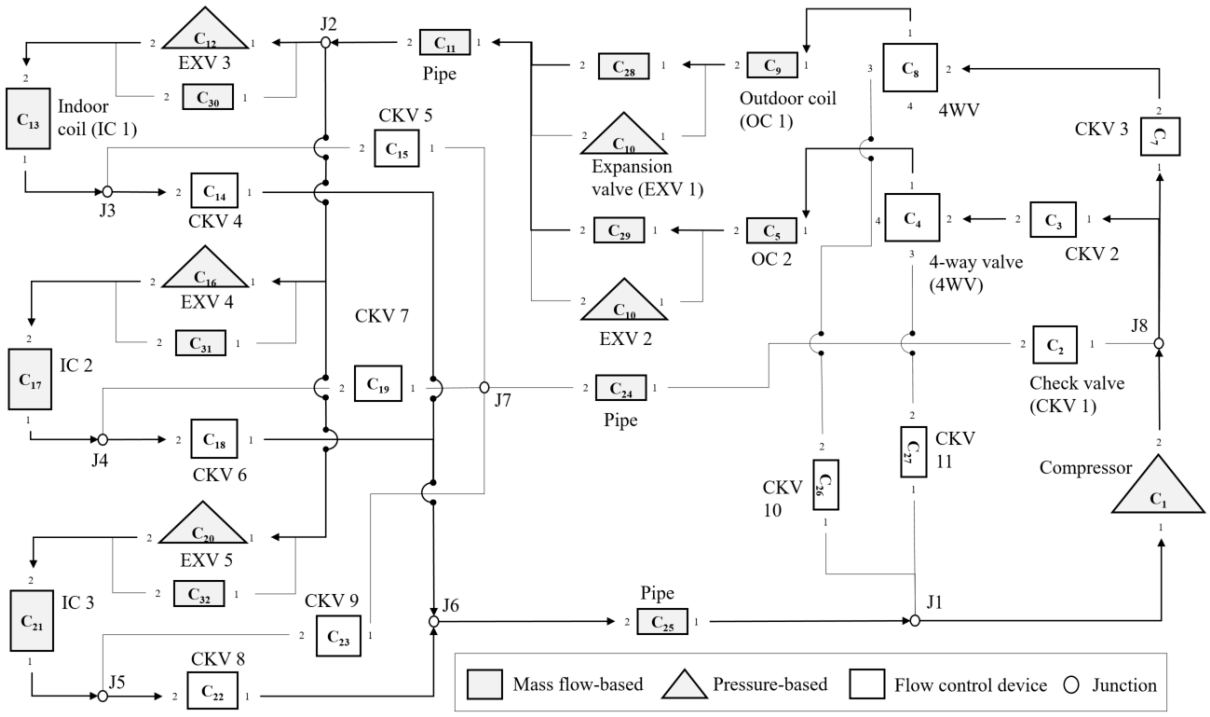

Figure 4.2 Component-based representation schematic of VRF heat recovery system at cooling only mode with flow directions

Table 4.1 Summary of the 3 operating modes

Mode No.	Mode	Enabled check valves	Enabled expansion valves	Condensers	Evaporators
1	Cooling only	CKV 2, 3, 4, 6, 8	EXV 3, 4, 5	OC 1, 2	IC 1, 2, 3
2	Simultaneous heaing & cooling	CKV 1, 4, 7, 9, 10, 11	EXV 1, 2, 3	IC 2, 3	IC 1; OC 1, 2
3	Heating only	CKV 1, 5, 7, 9, 10, 11	EXV 1, 2	IC 1, 2, 3	OC 1, 2

The component execution order would differ according to the operating mode. The HXs that serve as the condensers would always be executed before the evaporators. Table 4.2 shows the system equation formulations at the 3 operating modes. In all of the 3 modes, the boundary conditions of the compressor were the shared tearing variables. Apart from this, the algorithm selected the mass flow rates at the splitting junctions, and the outlet pressures of the active expansion devices as the tearing variables. Meanwhile, the algorithm would identify as the residual equations the junction equations that ensure the solution was closed thermodynamically, and ensure the pressure balance at the merging junctions. Lastly, modes 1 and 2 requires 4 design criteria to close the equations, while mode 3 requires 3 criteria.

Table 4.2 Tearing variables and residual equations of VRF heat recovery system at different operating modes

No.	**Mode 1: cooling only**		**Mode 2: simultaneous heating and cooling**		**Mode 3: heating only**	
	Tearing variable	**Residual equation**	**Tearing variable**	**Residual equation**	**Tearing variable**	**Residual equation**
1	$P_{1,1}$	$P_{10,2} = P_{6,2}$	$P_{1,1}$	$P_{1,1} = P_{26,1}$	$P_{1,1}$	$P_{1,1} = P_{26,1}$
2	$h_{1,1}$	$P_{1,1} = P_{25,1}$	$h_{1,1}$	$P_{1,1} = P_{27,1}$	$h_{1,1}$	$P_{1,1} = P_{27,1}$
3	$P_{1,2}$	$h_{1,1} = h_{25,1}$	$P_{1,2}$	$P_{1,1} = P_{25,1}$	$P_{1,2}$	$P_{20,1} = P_{16,1}$
4	$\dot{m}_{7,1}$	$P_{14,1} = P_{18,1}$	$\dot{m}_{19,1}$	$\sum_{J1,in}(\dot{m}h) = \sum_{J1,o}(\dot{m}h)$	$\dot{m}_{15,1}$	$\sum_{J1,in}(\dot{m}h) = \sum_{J1,o}(\dot{m}h)$
5	$\dot{m}_{12,1}$	$P_{14,1} = P_{22,1}$	$\dot{m}_{12,1}$	$P_{16,1} = P_{20,1}$	$\dot{m}_{19,1}$	$P_{20,1} = P_{12,1}$
6	$\dot{m}_{16,1}$	Criterion 1: SC at C_{11} inlet	$\dot{m}_{10,2}$	Criterion 1: SC at J2	$\dot{m}_{10,2}$	Criterion 1: SC at J2

No.	Mode 1: cooling only		Mode 2: simultaneous heating and cooling		Mode 3: heating only	
	Tearing variable	**Residual equation**	**Tearing variable**	**Residual equation**	**Tearing variable**	**Residual equation**
7	$P_{12,2}$	Criterion 2: IC1 outlet SH	$P_{12,2}$	Criterion 2: IC1 outlet SH	$P_{10,1}$	Criterion 2: OC1 outlet SH
8	$P_{16,2}$	Criterion 3: IC2 outlet SH	$P_{10,1}$	Criterion 3: OC1 outlet SH	$P_{6,1}$	Criterion 3: OC1 outlet SH
9	$P_{20,2}$	Criterion 4: IC3 outlet SH	$P_{16,1}$	Criterion 4: OC2 outlet SH		

4.1.2.Simulation conditions and results

Table 4.3 shows the simulation conditions. The cooling-only mode was simulated at 35 °C outdoor ambient temperature. The other 2 modes were both simulated at 8.3/6.1 °C outdoor temperatures. In mode 1, one indoor unit undertook dry cooling condition of 26.7/13.9 °C, while the other 2 undertook the wet cooling condition of 26.7/19.4 °C. In mode 2, the indoor conditions were dry cooling for IC1, and heating condition (21.1/15.6 °C) for IC 2, 3. This mode may represent a case in the winter where one room (i.e., server or equipment closet) requires cooling 24/7, while the other rooms require heating. We used the subcooling at J2 and the evaporator outlet superheat as the design criteria. There were 3 evaporators in mode 1 and 2, and thus the 3 individual superheat specifications, together with the subcooling, fulfilled the requirement of 4 design criteria. Similarly, the requirement of 3 criteria was fulfilled with the subcooling and 2 individual

superheat specifications. The values for subcooling and evaporator outlet superheat were fixed to 5 K in all 3 modes.

Table 4.3 Simulation conditions for the VRF-heat recovery system

No.	OC1 (°C)		OC2 (°C)		IC1 (°C)		IC2 (°C)		IC3 (°C)		RPM
	T_{db}	T_{wb}	T_{db}	T_{wb}	T_{db}	T_{wb}	T_{db}	T_{wb}	T_{db}	T_{wb}	
1	35	-	35	-	26.7	13.9	26.7	19.4	26.7	19.4	3600
2	8.3	6.1	8.3	6.1	26.7	13.9	21.1	15.6	21.1	15.6	2400
3	8.3	6.1	8.3	6.1	21.1	15.6	21.1	15.6	21.1	15.6	3600

Table 4.4 shows the energy imbalance and the simulated system performance for the 3 operating modes. For capacity, the positive value indicates cooling capacity, while the negative value indicates heating capacity. The 3 indoor coils were identical. In mode 1, less refrigerant was distributed to the indoor unit at the dry cooling condition comparing to the other two indoor units. In mode 2, the refrigerant was distributed equally between IC 2 and 3, which functioned as the condensers. And half of the refrigerant was distributed to IC 1, which served as the evaporator together with the 2 outdoor coils. In mode 3, the refrigerant was distributed equally among the 3 indoor coils. Figure 4.3 shows the P-h diagrams of the simulation results.

Table 4.4 Simulation results of the VRF-heat recovery system

Mode No.	Δ_E (%)	W (kW)	$\dot{m}$ (kg/s)	Q-IC 1		Q-IC 2		Q-IC 3	
				Q (kW)	$\dot{m}$ (g/s)	Q (kW)	$\dot{m}$ (g/s)	Q (kW)	$\dot{m}$ (g/s)
1	0.03	7.5	0.2	9.0 (dry)	56.8	11.4	71.8	11.4	71.8
2	0.04	3.5	0.103	9.5 (dry)	52.5	-11.1	51.3	-11.1	51.3
3	0.07	5.7	0.142	-10.2	47.2	-10.2	47.2	-10.2	47.2

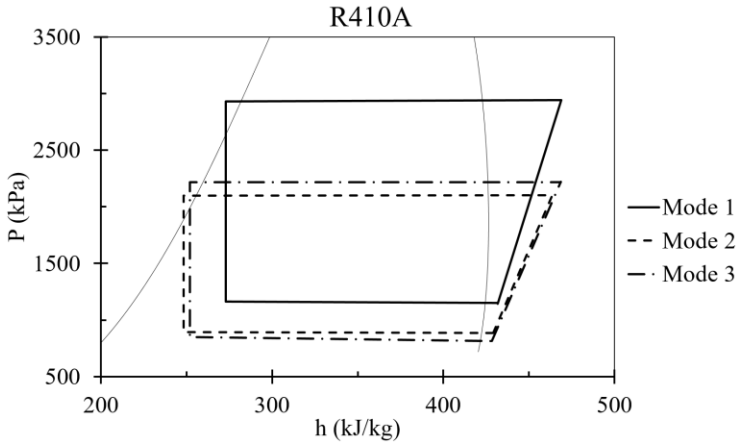

Figure 4.3 Simulated P-h diagrams of the VRF-heat recovery system at different operating modes

4.2. Simulation of two-stage vapor compression system with simultaneous vapor and liquid injection

Two-stage vapor compression systems may bring such advantages over single-stage systems as improved system performance, lower discharge temperature and less throttling loss. These systems may employ various intermediate configurations, such as liquid injection and vapor injection. Although two-stage systems were not uncommon in the commercial sectors, these systems were mostly geared toward small/medium capacity designs. Moreover, based on the literature review on two-stage system modeling in section 1.2.3.2, the modelling approach of these systems was dominantly theoretical or thermodynamic analysis.

This section presents a steady-state analysis of a R1234ze(E) two-stage compression system with simultaneous vapor and liquid injection for a large capacity application. The current simulation framework enables a detailed analysis with finite-volume HX models, which goes beyond the modeling complexity of this type of systems in the open literature. A parametric study was conducted to assess the impact of vapor injection ratio

and condenser air flow rate. Since the system is still in its early R&D stage and not yet publicized, all simulation results will be presented in their normalized values.

4.2.1.System description and equation formulation

Figure 4.4 shows the system configuration. The condenser and evaporator were microchannel air-to-refrigerant HXs. The economizer was a fluid-to-fluid HX. Port 1 and 2 of the economizer was the cold fluid end, while port 3 and 4 the hot fluid. The compressor was a turbo compressor with two injection ports, one for vapor injection while the other for liquid injection. The liquid injection served to cool down the motor and the electronics in the compressor. Port 3 of the compressor was for vapor injection, and port 4 was for liquid injection. The vapor injection was enabled by expansion valve 1 and the economizer. The vapor injection ratio of the system is given by

$$R_{vi} = \frac{\dot{m}_{valv1}}{\dot{m}_{cond}} = \frac{\dot{m}_{comp,3}}{\dot{m}_{comp,2}} \tag{11}$$

where $\dot{m}_{valv1}$ is the mass flow rate of the expansion valve 1, and $\dot{m}_{comp,3}$ is the mass flow rate of the compressor at port 3. The subcooled liquid from the economizer port 4 was expanded by expansion valve 3 before being injected into the turbo compressor. This stream of refrigerant was used for compressor motor cooling. The motor cooling liquid injection ratio is given by

$$R_{li} = \frac{\dot{m}_{comp,4}}{\dot{m}_{comp,1}} = \frac{\dot{m}_{valv3}}{\dot{m}_{eco,4}} \tag{12}$$

where $\dot{m}_{eco,4}$ is the mass flow rate of the economizer at port 4. Pipe 1 and 2 in the system are the discharge pipe and the injection pipe, respectively.

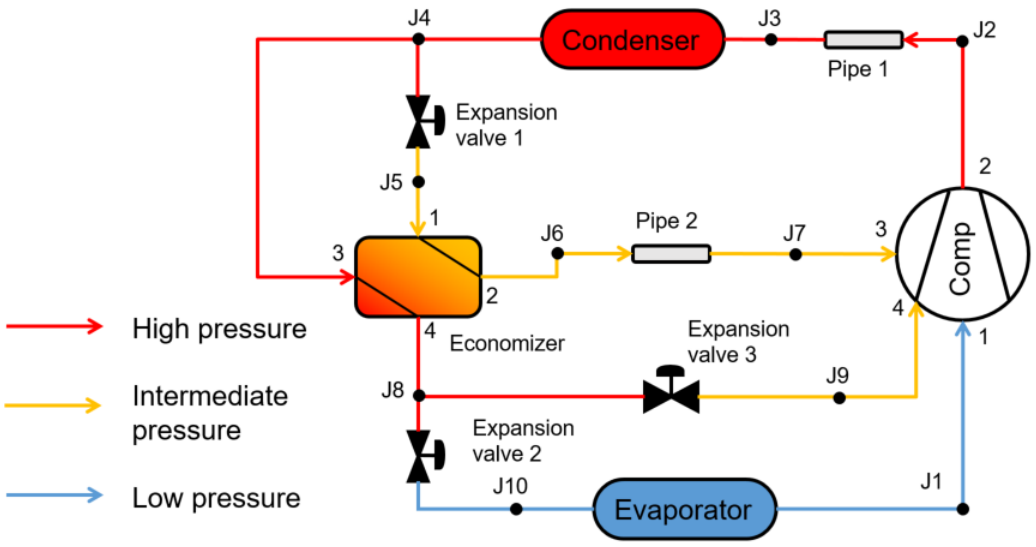

Figure 4.4 Schematic of simultaneous vapor and liquid injection system

The system refrigerant is R1234ze(E). The turbo compressor was represented with a customized performance map. The condenser and evaporator were simulated with the finite-volume model [5]. The economizer model was a lumped-effectiveness model.

The assumptions/simplifications for the system simulations are as follows:

i) All three expansion valves are presented by isenthalpic process without detailed simulation.

ii) The pressure levels at the two injection ports of the compressor (3 & 4) are equal.

iii) The motor cooling liquid injection ratio of the compressor is a constant parameter.

iv) The economizer model has a constant effectiveness of 0.93, and does not account for pressure drop.

Given these, the system equation formulations was given in Table 4.5. The algorithm identifies the need for 3 closure equations. We used the following design criteria to close the residual equations: the compressor suction superheat at J1 and the condenser outlet subcooling at J4. The third criteria was the vapor injection ratio (R_{vi}), or the compressor injection superheat at J7.

Table 4.5 Tearing variables and residual equations for the simultaneous liquid and vapor injection system

No.	Tearing variable	Residual equation
1	$P_{comp,1}$	$(\dot{m}h)_{comp,1} = (\dot{m}h)_{evap,out}$
2	$P_{comp,2}$	$(\dot{m}h)_{comp,3} = (\dot{m}h)_{pipe2,out}$
3	$P_{comp,3}$ (= $P_{comp,4}$ = $P_{eco,1}$)	$(\dot{m}h)_{comp,4} = (\dot{m}h)_{valve3,out}$
4	$h_{comp,1}$	$P_{evap,out}$ = $P_{comp,1}$
5	$h_{comp,3}$	Criterion 1: SH_{suc}
6	$h_{comp,4}$	Criterion 2: SC
7	$P_{valv2,\ out}$	Criterion 3: R_{vi} or SH_{inj}

4.2.2.Simulation tests for parametric study

Table 4.6 shows the parametric variable, the parametric range, and the test condition of the 3 simulation tests. The condenser air flow rates in the table are given in the normalized values against the minimum value. The test conditions follow the AHRI standard, and the air temperatures of each condition are shown in Table 4.7. The 3 convergence criteria were compressor suction SH = 2 K, condenser outlet SC = 3.36 K, and vapor injection ratio (R_{vi}). R_{vi} was set to 0.09 for test No.2, 100% load.

There existed no steady-state solution for test No.3, 75% load, because the subcooled liquid from the condenser could not bring the vapor injection stream to vapor phase regardless of the value of R_{vi}. Therefore, we added 1000 W of heat to the injection pipe

(pipe 2), and took it into account in the COP calculation. Also, for this particular test, we changed the convergence criterion from R_{vi} to injection SH = 1 K. For all simulation tests, the motor cooling liquid injection ratio (R_{li}) was set to 0.01.

Table 4.6 Summary of the simulation tests

Test No.	Test condition	Parametric variable	Range (Normalized)	Others
1	100% load	Vapor injection ratio	0.06 – 0.11	SH_{suc} = 2 K, SC = 3.36 K
2	100% load	Condenser air flow rate	1 – 1.5	SH_{suc} = 2 K, SC = 3.36 K, R_{vi} = 0.09
3	75% load	Condenser air flow rate	1 – 1.5	1000 W applied to injection pipe; SH_{suc} = 2 K, SC = 3.36 K, SH_{inj} =1 K

Table 4.7 100 and 75 percent load condition (AHRI340/360 (2019) [83])

Load condition	Indoor air		Outdoor
	T_{db} (K)	T_{wb} (K)	T_{db} (K)
100%	299.82	292.59	308.15
75%	299.82	292.59	300.65

4.2.3.Results and discussion

4.2.3.1.Effect of vapor injection ratio

As shown in Figure 4.5 (a), as R_{vi}, increases, capacity first increases and then decreases, while power consumption presents the opposite trend. As a result, the maximum COP occurs when R_{vi} = 0.1. To illustrate the effect of R_{vi} on Q, Figure 4.6 compares the system P-h diagram at R_{vi} = 0.06, R_{vi} = 0.1 (the optimum injection ratio),

and R_{vi} = 0.11. JX in the diagram is the junction number in Figure 4.4. Increasing R_{vi} from 0.06 to 0.1 resulted in an enhanced subcooling effect of the economizer, and thus a smaller quality at the evaporator inlet (J10). This increased unit refrigeration capacity played a more dominating role in overall system capacity, despite the fact that an increased R_{vi} also led to a smaller mass flow rate in the evaporator (or suction mass flow rate). The decrease in suction mass flow rate with increasing R_{vi} is indicated in Figure 4.5 (b). A further increase of R_{vi} to 0.11 hardly affected the location of J8, and meanwhile moved J7 from the vapor phase into the two-phase region. This indicates that the subcooling effect of the economizer has saturated, and therefore could no longer overcome the impact of the decreasing mass flow rate in the evaporator. Therefore, the system capacity decreased. The decrease in the injection quality at R_{vi} = 0.11 was also a response to the increase in the compressor power consumption.

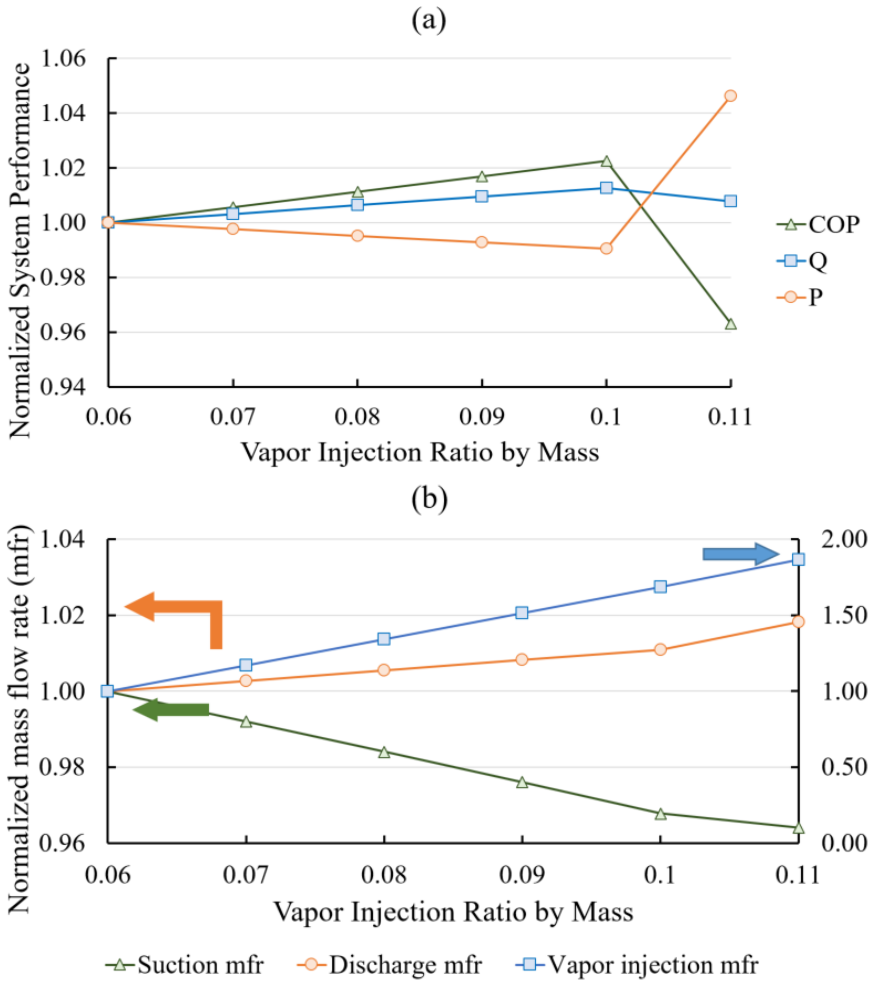

Figure 4.5 Effect of vapor injection ratio on (a): COP, capacity, and power consumption; (b): mass flow rates

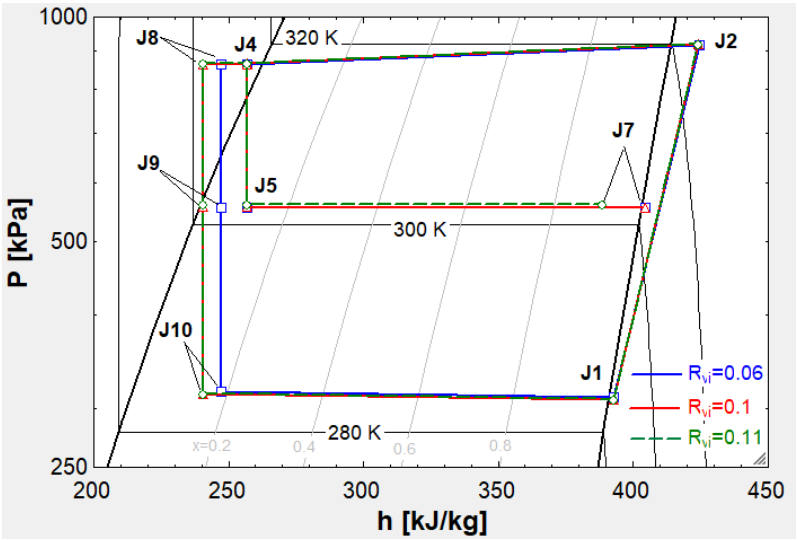

Figure 4.6 P-h diagrams at 3 vapor injection ratios (R_{vi})

It should be noted that the optimum R_{vi} =0.1 was obtained under the assumption of constant economizer effectiveness. In reality, the economizer effectiveness might differ depending on the operating conditions. Therefore, the optimum R_{vi} would largely depend on the performance of the economizer.

4.2.3.2. Effect of condenser air flow rate

Figure 4.7 (a) shows the effect of condenser air flow rate on COP, capacity, and power consumption at 100% load condition (308.15 K ambient temperature). Two sets of results are presented: the dash lines show the fan power excluded results, while the solid lines include the fan power consumption. The fan power was estimated with

$$W_{fan} = \frac{\Delta P_{air} \dot{V}_{air}}{\eta_{fan}} \tag{13}$$

where ΔP_{air} is the air-side pressure drop, $\dot{V}_{air}$ is the volumetric air flow rate of condenser, and η is the efficiency which was assumed to be 0.75.

As the flow rate increases, the system capacity increases monotonically. This increase was caused by two factors. The first is the slight increase in suction mass flow rate, as shown in Table 4.8. The second is the decreased quality at the evaporator inlet. Figure 4.8 (a) shows the P-h diagram of 100% load condition at 3 different flow rates. The P-h diagram shows that an increase in the flow rate leads a decreasing condensing pressure. This is because higher flow rate resulted in better heat transfer, and thus smaller approach temperature in the HX. As a result, the evaporator inlet was pushed toward a lower quality, as shown in the J10 zoom in the figure.

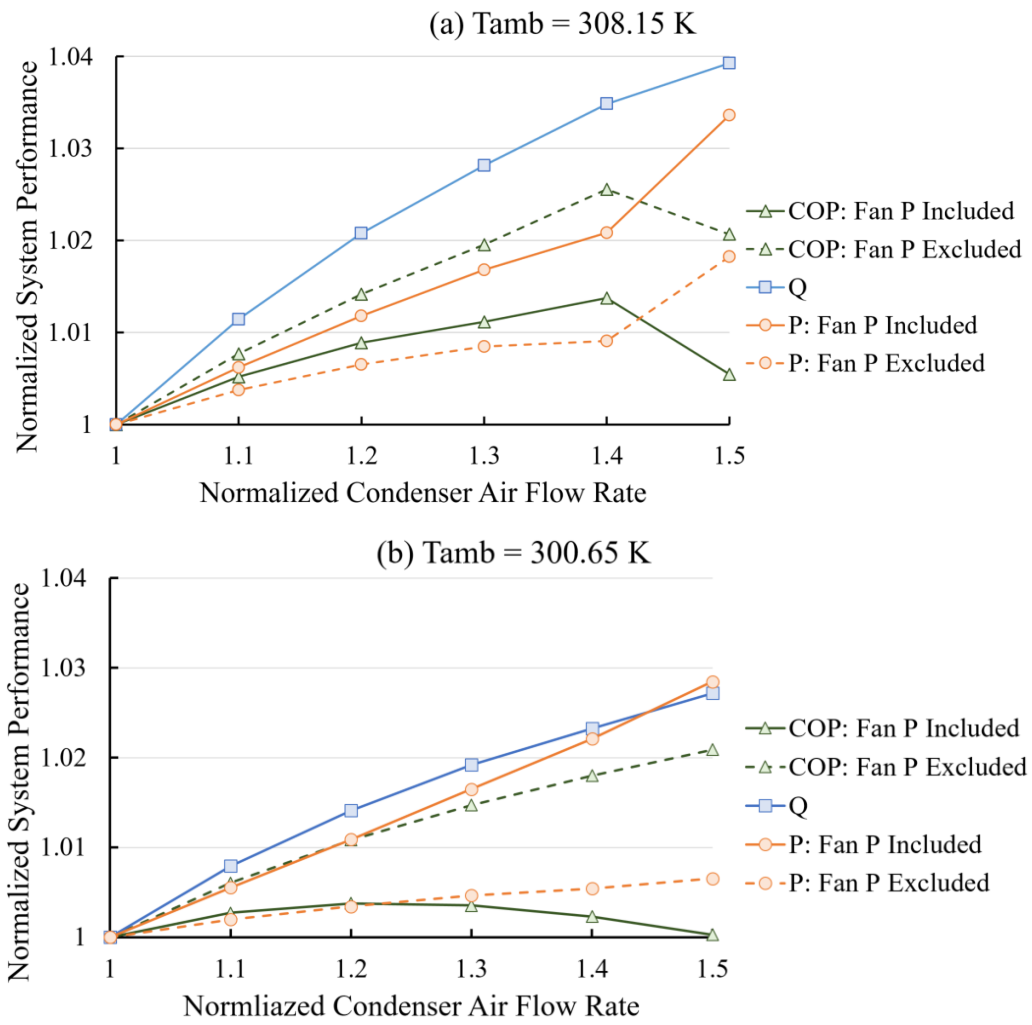

Figure 4.7 Effect of condenser air flow rate on system performance at (a) 100% load, (b) 75% load condition

As the flow rate increases, the power consumption (with and without fan) also increases monotonically. However, when the rate flow was increased by 50% ($\hat{V}$ = 1.5), the increase in power consumption was more dramatic than that at other flow rates. This was seen in both the compressor power and the total power, suggesting this behavior was mainly caused by compressor. The reason for this behavior is that, as the flow rate was increased by 50%, the quality at the injection point (J7) moved from vapor phase to two phase, as shown in J7 zoom in Figure 4.8 (a). This increase in power consumption was

more significant than the increase in capacity. Therefore, system COP (with and without the fan power) started to drop when the normalized flow rate exceeded 1.4.

Table 4.8 Effect of condenser air flow rate on the mass flow rates (normalized)

$\hat{\dot{V}}$ (-)	100% load		75% load	
	Normalized suction $\dot{m}$	Normalized Vapor injection $\dot{m}$	Normalized Suction $\dot{m}$	Normalized Vapor injection $\dot{m}$
1	1	1	1	1
1.1	1.003	1.003	1.006	0.956
1.2	1.005	1.006	1.010	0.919
1.3	1.007	1.007	1.014	0.889
1.4	1.008	1.008	1.017	0.863
1.5	1.010	1.010	1.020	0.839

Figure 4.7 (b) shows the effect of condenser air flow rate at 75% load condition (300.65 K ambient temperature). It should be noted that two things were different at 75% load condition from 100% load simulation.

First, an addition of 1000 W energy was applied to the injection pipe. This heat was added to the power consumption in COP evaluation. This addition was necessary because, when the ambient temperature decreased, the approach temperature in the economizer could no longer lead to superheated vapor injection. In Figure 4.8 (b), we compared the 100% and 75% load P-h diagrams, at a normalized flow rate of 1. The decrease of ambient temperature significantly lowered the condensing temperature. However, the injection pressure was not lowered as significantly. As a result, the approach temperature in the economizer was decreased. And the injection stream in the economizer could not be heated to superheated vapor by the subcooled liquid from the

condenser. As shown in the figure, the quality at J6 (inlet of the injection pipe) is roughly 0.9 or less.

Second, the convergence criterion was injection SH = 1 K, instead of a fixed vapor injection ratio. Because of this, the vapor injection mass flow rate decreased with an increasing flow rate (as shown in Table 4.8).

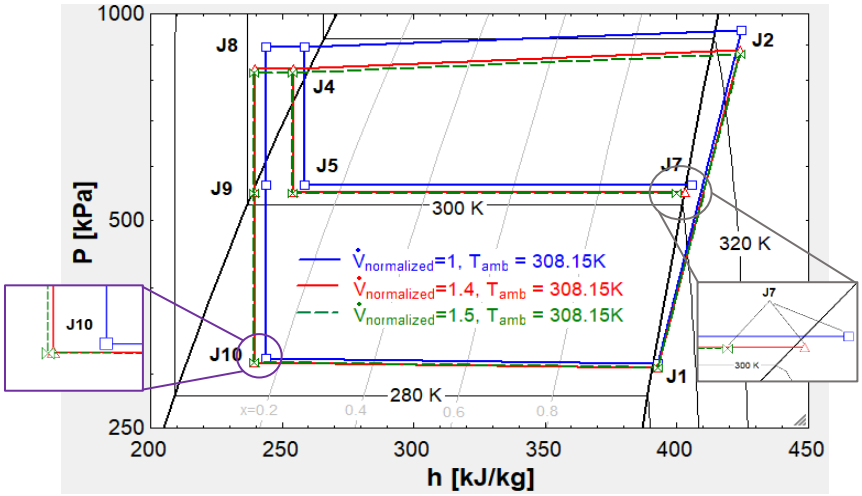

(a)

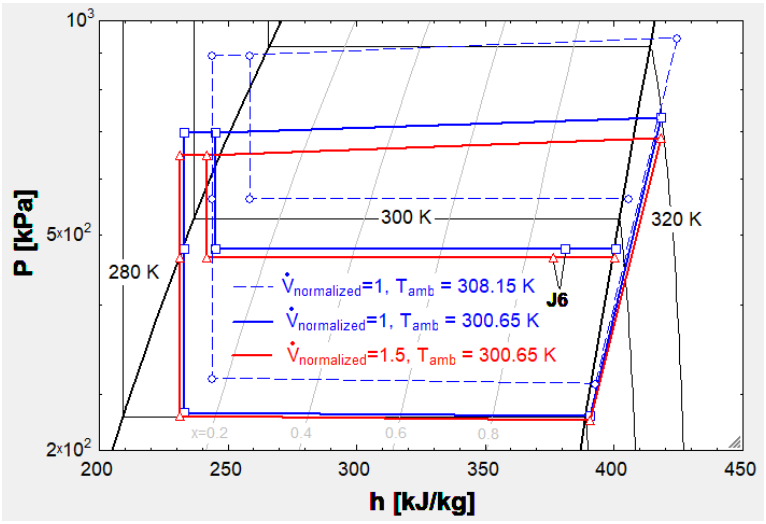

(b)

Figure 4.8 P-h diagrams at different condenser air flow rates and ambient temperatures

As the flow rate increases, the system capacity increases monotonically. This trend is similar to the 100% load. Figure 4.8 (b) shows the P-h diagram of 75% load condition at

the minimum and maximum flow rate. Due to the heat addition, the injection point would remain the superheated state at all flow rates. Thus, the power consumption did not undergo accelerated increase as in 100% load. While the system COP excluding the fan power consumption increases monotonically, the COP that considers the fan power reaches the maximum when normalized flow rate is 1.2. At this optimum flow rate, the COP improvement (considering fan power) was less than 0.5%.

4.3. Summary

This Chapter presented an extended demonstration on the capability of the general-purpose simulation framework. The solution methodology was applied for the steady-state analysis of two advanced vapor compression systems that have not been widely applied. The first system was a VRF heat recovery system with simultaneous heating and cooling. The simulation of the first system demonstrated high level of capability of the simulation framework to evaluate the steady-state performance of systems with multiple operating modes. The second system was a two-stage vapor compression system with simultaneous liquid and vapor injection. The effect of two system design variables, vapor injection ratio and condenser air flow rate, on the system performance was studied. The investigation of the second system demonstrated that the framework was able to push the steady-state analysis of a large capacity two-stage system beyond the modeling complexity of the two-stage systems in the open literature.

5. Approximation-assisted heat exchanger modeling for steady-state simulation of vapor compression systems

This Chapter aims to advance the computational efficiency for steady-state vapor compression system simulation. The study presented in this Chapter has been published in Applied Thermal Engineering (2020).

5.1. Background and motivation

In the current simulation framework, the system solver has no control over the computational and numerical behavior of the components. Among all the components, the heat exchanger (HX) model is often the most time-consuming and numerically challenging components. Therefore, an accurate, fast and robust HX model is the key to improve the computational speed for the steady-state vapor compression system simulation.

As summarized in Chapter 1, there are three approaches for HX modeling and representation: physics-based approach, hybrid approach, and black-box approach. In the engineering research disciplines, the black-box approach, also referred to as the metamodel, is a critical numerical technique to speed up the simulation.

The metamodeling methodology was first introduced in 1989 by Sacks *et al*. [84] along with the phrase “design and analysis of computer experiments”, or DACE as it has become known, to model a deterministic and computationally expensive model in computer analyses. It has been widely used in the disciplines of structural optimization [85], aerospace engineering [86] and HVAC&R applications. In HVAC&R, metamodeling has been applied to facilitate novel heat exchanger design [87] [88],

component and system analysis and optimization [89] [90] [91] [92], and building energy performance prediction [93]. Popular metamodeling techniques include the polynomial response surface, neural networks, kriging, and support vector regression among others [94]. Some researchers believe that despite the vast pool of metamodeling techniques, a clear criteria for selecting one technique over another [95] is lacking. It is also claimed that the performance of those techniques depends on both the nature of the problem and Design of Experiment [85].

For means of simplification of the finite-volume HX model, the moving-boundary (or lumped parameters) approach is a commonly used method [96, 97, 98, 99]. Pangborn et al. [97] compared finite-volume and moving-boundary approaches for one-dimensional dynamic HX modeling. They suggested the true tradeoff in these two should be speed and flexibility. Bell et al. [98] presented a generalized moving boundary approach for counter-flow HX models. Its computational time with property calculation speedup was reported to be on the order of 2.2 ms per run. However, they did not quantitatively assess the loss in the accuracy.

To sum up, efficient, accurate and robust HX performance model is of great importance to the simulation of vapor compression systems. Various means of simplification and approximation are available. However, there is little literature that comprehensively reports how much speed improvement can be achieved and how much accuracy will be sacrificed by employing approximation on the component or the system level. Therefore, this chapter aims to propose an approximation methodology to speed up steady-state vapor compression system simulation. To this end, we developed and compared three approximation-assisted HX modeling methods in terms of accuracy and

computational efficiency, with finite-volume model being the baseline. They are interpolation black-box model, Kriging black-box model, and Kriging-assisted three-zone model.

5.2.Approximation-assisted modeling methodology

The approximation-assisted modeling methodology consists of four steps. The first step is the determination of the input domain for HX approximation. The input domain is all the refrigerant inlet states to a HX, given a fixed HX geometry and HX operating context. The second step is to sample a certain number of input states from the domain. The third step is to simulate the HX performance at those sample states with the detailed HX model. The fourth step is to fit the simulation results to approximation-assisted models. The entire process is automated, and the flowchart is given in Figure 5.1.

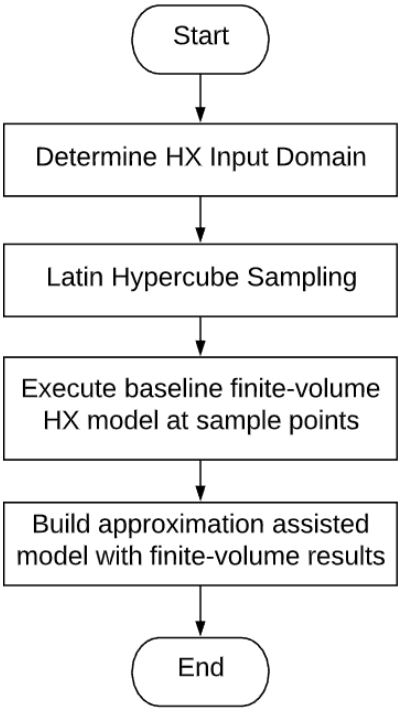

Figure 5.1 Flowchart of the approximation-assisted modeling methodology

5.2.1.Input domain and sampling

The refrigerant inlet variables to the HX are pressure, enthalpy and mass flow rate. Thus, the refrigerant input state can be defined as a three-component vector *X*, and therefore the input domain *D* is defined as

$$D = \begin{cases} D_e = \{ X = (P, h, \dot{m}) \mid evap\ inlet \} \\ D_c = \{ X = (P, h, \dot{m}) \mid cond\ inlet \} \end{cases} \tag{14}$$

To estimate the evaporator and condenser input domains, the following parameters must be provided or assumed from the user end:

1. Secondary fluid inlet temperature of the condenser and the evaporator ($T_{sec,in,c}$ and $T_{sec,in,e}$)
2. Degree of superheat (SH)
3. Difference between the lower bound of discharge dew point temperature and the condenser airside inlet temperature ($\Delta T_{dis-\sec} = \Delta T_{dis,dew,l} - \Delta T_{\sec,in,c}$)
4. Difference between the evaporator airside inlet temperature and the upper bound of suction dew point temperature ($\Delta T_{suc-\sec} = \Delta T_{\sec,in,e} - \Delta T_{suc,dew,u}$)
5. Difference between the upper and lower bound of discharge dew point temperature ($\Delta T_{dis,dew} = \Delta T_{dis,dew,u} - \Delta T_{dis,dew,l}$)
6. Difference between the upper and lower bound of suction dew point temperature ($\Delta T_{suc,dew} = \Delta T_{suc,dew,u} - \Delta T_{suc,dew,l}$)
7. Compressor model

Figure 5.2 shows the flowchart to determine the input domain *D*. Figure 5.3 shows an example of the projection of such a domain on the P-h diagram, assuming an efficiency-based compressor model.

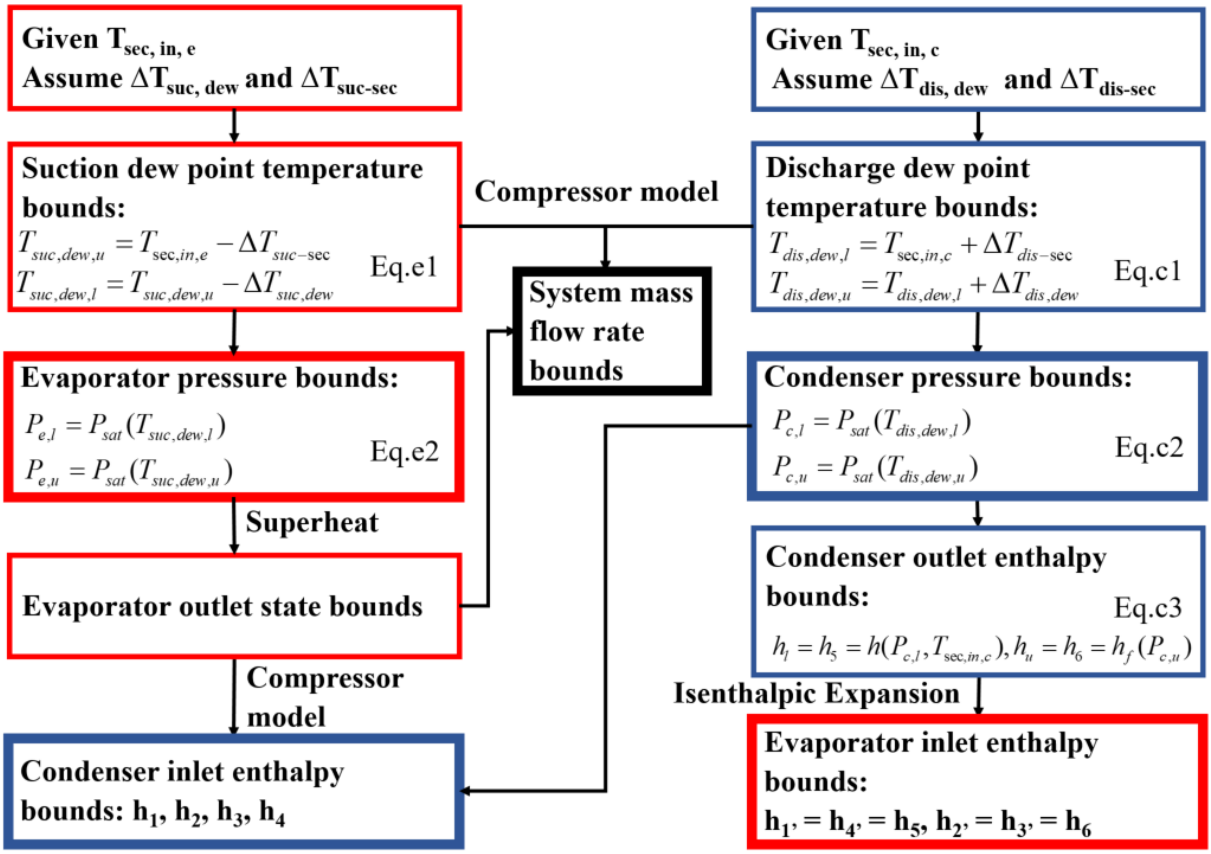

Figure 5.2 HX input domain determination method

The determination of D_e and D_c starts with the bounds of discharge dew point temperature, $T_{dis,dew}$ and the bounds of suction dew point temperature, $T_{suc,dew}$, as indicated by Eq.e1 and Eq.c1 in Figure 5.2, where subscript *l* and *u* represent the lower and upper bound, respectively. We then determine the evaporator and condenser pressure bounds using Eq.e2 and Eq.c2, and the upper and lower bound of condenser outlet enthalpy using Eq.c3. Due to isenthalpic expansion, the bounds of condenser outlet enthalpy are equivalent to the bounds of evaporator inlet enthalpy. The evaporator

pressure bounds and its inlet enthalpy bounds form the enclosure 1'-2'-3'-4'-1', which is the projection of evaporator input domain D_e on P-h diagram, as shown in Figure 5.3. It should be noted that above mentioned method assumes no piping in the system.

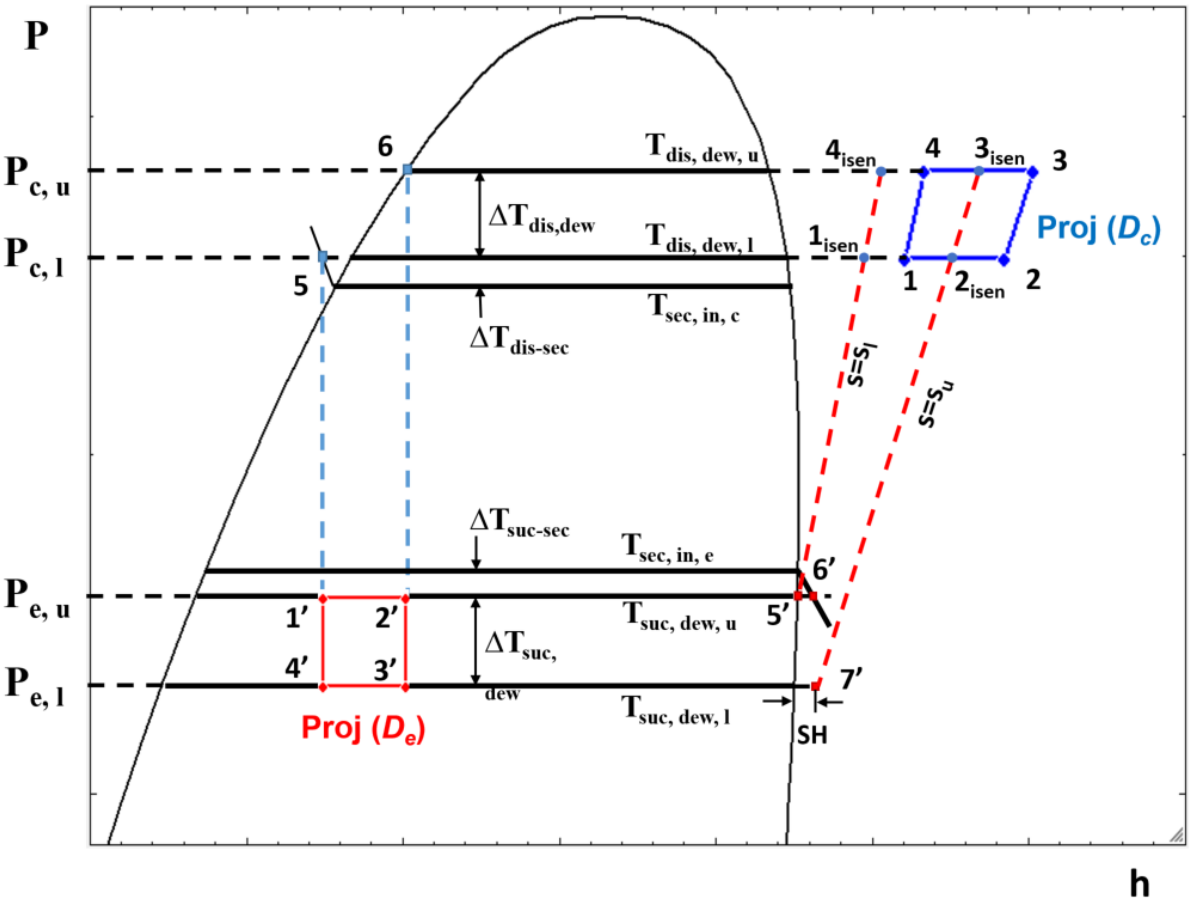

Figure 5.3 Projection of the input domains onto P-h diagram (assuming efficiency-based compressor model)

The condenser inlet enthalpy (or compressor discharge enthalpy) is bounded by the evaporator outlet states and the compressor model. E.g. in the case of efficiency-based compressor, the discharge enthalpy bounds can be determined by the bounds of evaporator outlet entropy, or suction entropy. This is because a higher suction entropy leads to a higher discharge enthalpy at a fixed discharge pressure. The lowest suction entropy occurs at 5', which is the dew point at $P_{e,u}$. The highest suction entropy,

depending on the refrigerant, may occur at 6' or 7'. The states for suction points 5', 6' and 7' are indicated in Figure 5.3. Then, the lowest discharge enthalpy corresponds to the suction point with the minimum entropy. Likewise, the highest discharge enthalpy corresponds to the suction point with the maximum entropy. The enclosure 1-2-3-4-1 in Figure 5.3 represents the projection of condenser input domain D_c. The system mass flow rate is bounded by running the compressor model at the bounds of $T_{dis,dew}$ and the bounds of evaporator outlet state.

Once the HX input domain is determined, we need to sample a certain number of points from the input domain. To have a reasonable balance between approximation accuracy and computational cost, we used 27 sample points (3 points per dimension of the input domain, or three-level full factorial design [100]) to build the approximation models. With regard to the technique to obtain the 27 points, Latin Hypercube Sampling [101] was used. The 27 sample points form the sample library *S*, which can be expressed as

$$S = \left\{ X_1, X_2, ..., X_{27} \mid X_j \in D, j = 1, 2, ..., 27 \right\} \tag{15}$$

The detailed HX models then use S to generate the result library *R*, given by

$$R = \left\{ Y_1, Y_2, ..., Y_{27} \right\} \tag{16}$$

The output in the result library Y_i (i = 1, 2, …, 27) depends on type of the approximation-assisted model. For Kriging and interpolation black-box model, the approximation output is the overall performance of the HX. For the Kriging-assisted three-zone model, the approximation output is the pressure drops and overall heat transfer

coefficients of each zone. More details of each approximation model is given in Section 5.2.2.

5.2.2.Approximation-assisted heat exchanger models

This section presents three approximation-assisted HX models: interpolation black-box model, kriging black-box model, and kriging-assisted three-zone model. Table 5.1 summarizes the three models.

Table 5.1 Summary of the approximation-assisted HX models

Approximation-assisted model	Model inputs	Approximation output (Y_i)	Approximation techniques
Interpolation black-box model	Refrigerant side P_{in}, h_{in}, $\dot{m}$	ΔP, Δh, SHR (if applicable)	Natural neighbor interpolation
Kriging black-box model	Refrigerant side P_{in}, h_{in}, $\dot{m}$	ΔP, Δh, SHR (if applicable)	Kriging
Kriging assisted three-zone model	Refrigerant side P_{in}, h_{in}, $\dot{m}$	U and ΔP meta-model for each zone, SHR (if applicable)	Kriging

5.2.2.1.Kriging black-box model

As shown in Eq.(17), the outputs in the result library are the heat exchanger pressure drop (ΔP) and enthalpy change (Δh) evaluated by the detailed HX model at each sample input state. If dehumidification needs to be accounted for, then airside sensible heat ratio (SHR) is the third output, as shown in Eq.(17),

$$Y_j = \left(\Delta P, \Delta h, SHR\right) = f\left(X_j\right), X_j \in S, Y_j \in R \tag{17}$$

where f(·) represents the input-output relation given by the detailed model. The 27 sets of inputs and outputs are fitted by Kriging with the Matlab Kriging toolbox [102] into

a meta-model $f_K(\cdot)$, as shown in Eq.(18). The metamodel provides a one-to-one relationship between the input state within *D* and the HX outputs.

$$f_K(X) = Y = (\Delta P, \Delta h, SHR), X \in D \tag{18}$$

Kriging [103] [104] is a statistical model that is widely used to approximate the computationally expensive functions in engineering design and optimization. The Kriging model can be expressed by Eq.(19),

$$f_K(X) = \mu(X) + Z(X) \tag{19}$$

which consists of two parts. The first part μ is a polynomial model, or "trend model" that approximates the global trend of the function over the entire domain. The second part *Z* is a local spatial deviation model, or "departure model" that "pulls" the predicted responses through the sample points.

The departure model $Z(\cdot)$ is normally distributed with mean zero (Eq.(20)) and variance σ^2. Moreover, it assumes that the deviations at two sample points are correlated with the distance between them. The correlation between the deviations at any two sample points is measured by the covariance, as shown in Eq.(21).

$$E(Z(X)) = 0 \tag{20}$$

$$Cov(Z(X_i), Z(X_j)) = \sigma^2 R(d_{ij}),\ d_{ij} = |X_i - X_j| \tag{21}$$

where σ^2 is the process variance of $Z(\cdot)$, and $R(\cdot)$ is a spatial correlation function. Table 5.2 lists different choices for the correlation function, and their function forms.

Table 5.2 Correlation functions in Kriging model [102]. $d_{ij} = |X_i - X_j|$

Name	$R(d_{ij})$
Gaussian	$\exp\left[-\theta\left(d_{ij}\right)^2\right]$
Cubic	$1-3\xi^2+2\xi^3,\ \xi=\min\left\{1,\theta d_{ij}\right\}$
Spline	$\begin{cases} 1-15\xi^2+30\xi^3 & for\ \ 0\le\xi\le 0.2 \\ 1.25\left(1-\xi\right)^3 & for\ \ 0.2<\xi<1\ \ ,\ \xi=\theta d_{ij} \\ 0 & for\ \ \xi\ge 1 \end{cases}$
Exponential	$\exp\left[-\theta d_{ij}\right]$

In the case of HX performance approximation, the correlation function in Gaussian form between two inlet states (X_i, X_j) is given by Eq.(22).

$$R\left(X_i, X_j\right)=\exp\left[-\theta_1\left(p_i-p_j\right)^2-\theta_2\left(h_i-h_j\right)^2-\theta_3\left(\dot{m}_i-\dot{m}_j\right)^2\right] \qquad (22)$$

The correlation function has the following intuitive properties: when the distance between two inlet states is small, the correlation is strong. When the distance is large, the correlation will approach zero. Moreover, the parameter θ in the correlation function can be interpreted as measuring the importance of each dimension of the input domain. For example, if θ_3 is large, then even a small value of $|\dot{m}_i-\dot{m}_j|$ may lead to large differences in the function values at the two inlet states X_i and X_j. This means that mass flow rate is very important. In statistical terms, this means that a small value of $|\dot{m}_i-\dot{m}_j|$ is associated with low correlation between the deviations $Z(X_i)$ and $Z(X_j)$.

Developing a Kriging model is to determine the following parameters by maximizing the Likelihood Function [105]: the form of the trend model, the variance of the departure model, the form of the spatial correlation function, and parameter θ for each dimension of

the input domain. In the rest of this Chapter, Kriging black-box model is also referred to as the Kriging metamodel.

5.2.2.2. Interpolation black-box model

In the interpolation black-box model, natural neighbor interpolation (NNI) [106] is used to approximate the HX overall pressure drop (ΔP), enthalpy change (Δh), and SHR (if required), based on the 27 sample results. In NNI algorithm, the input data of the sample library is put in the form of a Voronoi diagram [107] and/or Delaunay triangulation, which are dual structures of each other. Then the algorithm relates the outputs at a new input point mathematically to its neighboring input points. Each neighboring point contributes in a way related to its distance from the new point, as written as

$$f_{NNI}(X) = \sum_{j=1}^{n} w_j(X_j) Y_j, X_j \in S, Y_j \in R, X \in D \tag{23}$$

where X is the new input point from domain D, n is the number of natural neighbors of X, X_j and Y_j (j = 1,…,n) are the neighboring inputs and the associated outputs. w_j are the weights associated with each natural neighbors. The Voronoi region constructed around the new input will overlap the original Voronoi regions that make up the complete Voronoi diagram. Therefore, each weight is calculated as

$$w_j(X_j) = A(X_j) \cap A(X) / A(X) \tag{24}$$

where the denominator presents the total Voronoi area associated with the new input X, and the numerator represents the overlap between the Voronoi area associated with natural neighbor j and the area associated with X.

We used *scatterInterpolant* function in Matlab to perform the NNI model. This model is also referred to as the interpolation metamodel in the rest of this Chapter.

5.2.2.3. Kriging-assisted three-zone model

The following assumptions were made for this model:

i) The circuitries/flow paths in the heat exchanger are assumed to be represented by one equivalent tube with a tube length of L_{eq}.

ii) A lumped heat transfer coefficient and a lumped pressure drop is applied to each zone. And their values were approximated by Kriging from the 27 sample runs.

iii) Air-side pressure drop is neglected.

In this model, we divide the HX into one to three-zones depending on the operating conditions. Heat transfer and hydrodynamics in each zone is characterized by a lumped overall heat transfer coefficient (U) and a lumped pressure drop (ΔP), respectively. Therefore, for the three-zone model, the outputs in the result library include U and ΔP of each phase, and *SHR* if dehumidification is required,

$$Y_j = \left(\Delta P_{vap}, \Delta P_{tp}, \Delta P_{liq}, U_{vap}, U_{tp}, U_{liq}, SHR\right) = g\left(X_j\right), X_j \in S, Y_j \in R \qquad (25)$$

where g(·) represents the general input-output relationship from the detailed model. Then the inputs and outputs are fitted by Kriging into the metamodel $g_K(\cdot)$ that maps the HX input into the key HX parameters, as shown in Eq.(26).

$$g_K(X) = Y = \left(\Delta P_{vap}, \Delta P_{tp}, \Delta P_{liq}, U_{vap}, U_{tp}, U_{liq}, SHR\right), X \in D. \quad (26)$$

Phase indicator *i* is introduced to unify the case of evaporator and condenser. For the case of condenser ($T_{air,in} < T_{ref,in}$), *i* would be 1, 2 and 3 representing vapor phase, two phase and liquid phase, respectively. For the evaporator ($T_{air,in} > T_{ref,in}$), the definition of *i* is reversed. The initial value of the phase indicator would depend on the input state *X*. If *i* is 1 at the HX inlet, there may be up to three zones in the HX. If *i* is 2 at HX inlet, there may be up to two zones. If *i* is 3 at HX inlet, only one zone exists. Usually, *i* starts at 2 in the case of evaporator, and starts at 1 in the case of condenser.

Figure 5.4 shows the flow chart of the kriging-assisted three-zone model. Before the refrigerant side calculation, the value of ΔP and *U* for each phase, and SHR are determined from the parameter metamodel (Eq.(26)). So, pressure drop calculation is decoupled from energy calculation. The refrigerant side calculation begins with determining the outlet pressure of the first zone ($P_{1,o}$). The outlet enthalpy of the first zone, for the time being, is assumed to be the saturation enthalpy at $P_{1,o}$. The length for the first zone (L_1) is then estimated based on the following energy balance,

$$Q = \dot{m}(h_o - h_{in}) = U(\pi dL)\left(T_{ref} - T_{air,in}\right) \quad (27)$$

The energy balance equation is also shown by Eq.(a) in Figure 5.4, where d is either the tube inner diameter or the hydraulic diameter of the flow channel, and T_{ref} is the mean temperature of the refrigerant in the first zone. If the calculated length is longer than the total length HX (L), then the previous assumption of saturation enthalpy at the outlet is not valid. The outlet enthalpy must be re-calculated using Eq.(b) in Figure 5.4. If the length is shorter than the total length, the assumption is valid. The above calculation is

repeated to determine the length of the second zone. If the sum of the first and the second length exceeds the total length, the HX can only accommodate two zones/phases. If not, the length of the last zone would be the remaining length in the HX.

At the end of refrigerant side calculation, the model checks whether the second law of thermodynamics is violated. If the HX outlet temperature violates the second law, (e.g. lower than the secondary fluid inlet temperature in the case of condenser), its value is re-assigned to be the secondary fluid inlet temperature, and the outlet enthalpy is re-calculated based on the outlet pressure and the new outlet temperature.

In the air-source evaporator case, airside calculation is performed after refrigerant calculation, assuming no pressure drop. The outlet humidity ratio (ω_o) is given by

$$Q(1-SHR) = h_{lv}\dot{m}_{dry,air}(\omega_{in} - \omega_o). \tag{28}$$

which is also Eq.(c) in Figure 5.4, where Q is the total HX capacity resulted from the refrigerant side calculation, SHR is the sensible heat ratio determined by the parameter metamodel $g_k(\cdot)$, h_{lv} is the evaporation heat of the water, $\dot{m}_{dry,air}$ is the mass flow rate of the dry air, ω_{in} is the inlet humidity ratio, and $h_{in,air}$ is the airside inlet enthalpy. Airside outlet enthalpy ($h_{o,air}$) is given by

$$Q = \left(h_{in,air} - h_{o,air}\right)\dot{m}_{dry,air}. \tag{29}$$

which is Eq.(d) in Figure 5.4, where $h_{in,air}$ is the airside inlet enthalpy. This model is also referred to as the three-zone model.

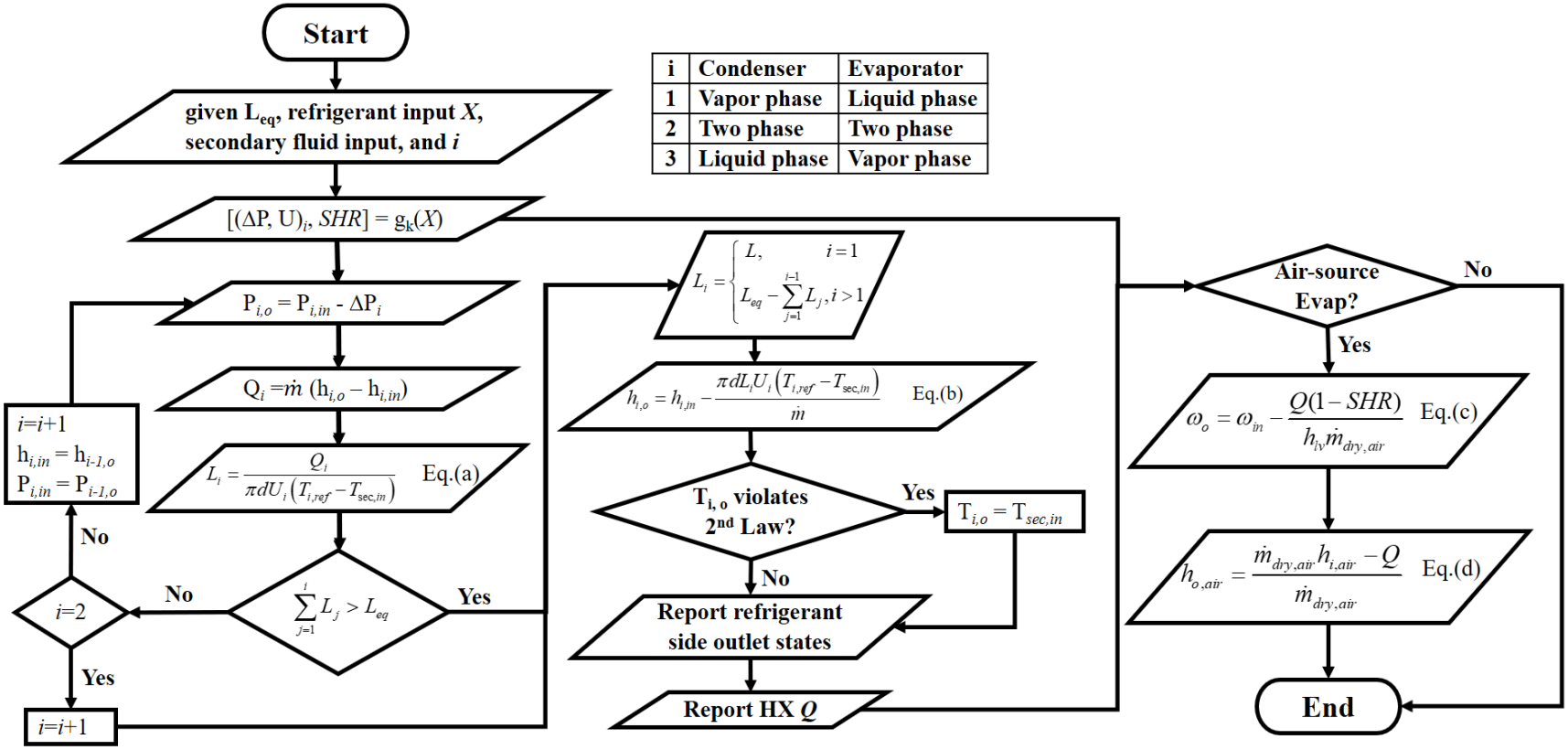

i	Condenser	Evaporator
1	Vapor phase	Liquid phase
2	Two phase	Two phase
3	Liquid phase	Vapor phase

Figure 5.4 Flowchart of the kriging-assisted three-zone HX model

5.3.Approximation-assisted model verification method

This section describes the verification method for the approximation-assisted models. We used five different HXs for verification. The corresponding geometry and simulation details are presented in section 5.3.1. We applied the approximation models to three vapor compression systems from different applications. The configurations and the simulation conditions for each system are presented in section 0. Property evaluation method and the computer specification are given in section 5.3.3.

5.3.1.HX-level verification

5.3.1.1. Verification method

In HX-level verification, two air-to-refrigerant tube-fin HXs (TFHX1 and TFHX2), two water-to-refrigerant plate HXs (PHX1 and PHX2), and a water-to-refrigerant coaxial HX (CHX1) were simulated by the baseline model and the approximation-assisted models. The refrigerant was R410A. The secondary fluid was air or water, depending on the type of HX. Table 5.3 listed the basic information of the five HXs. The geometry and the baseline HX model is elaborated in Section 5.3.1.2.

Table 5.3 Summary of the HXs

HX ID	TFHX1	TFHX2	PHX1	PHX2	CHX1
Geometry	Tube-fin	Tube-fin	Plate HX	Plate HX	Coaxial HX
Refrigerant	R410A				
Secondary fluid	Air	Air	Water	Water	Water
Baseline HX model	Finite-volume model [5]		Finite-volume model [6]		Finite-volume model [5]

For each HX, the input domain was determined as described in Section 5.2.1, from which 27 input states (3 per dimension of the input domain) were sampled by the Latin

Hypercube method. The sample points were then evaluated by the baseline model to build the Kriging metamodel, interpolation metamodel, and Kriging-assisted three zone model, respectively.

After the three approximation-assisted models were constructed, we randomly selected 10,000 input states from the HX input domain. The thermal and hydraulic performance of the HX at these 10,000 input states was evaluated by both the baseline model and the approximation models. For each input state, the error between the baseline result and the approximation-assisted result was calculated by

$$\delta_Y = \frac{Y - Y_{baseline}}{Y_{baseline}} \tag{30}$$

where Y may stand for enthalpy change Δh, pressure drop ΔP, and sensible heat ratio (SHR). Different approximation models would give different error values. The verification process was repeated for all the five HXs.

5.3.1.2. Geometric parameters and baseline model description

Geometric parameters of TFHX1 and TFHX2 can be found in [49], those of CHX1 can be found in [108], and those of PHX1 and PHX2 are listed in Table 5.4.

Table 5.4 Geometric parameters of PHX1 and PHX2

	Unit	**PHX1**	**PHX2**
Plate length	mm	420	450
Plate width	mm	240	240
Plate thickness	mm	0.3	0.3
Plate number	-	40	60
Plate HX height	mm	62.1	94.1
Plate type	-	Chevron	Chevron
Chevron angle	deg	30	30

	Unit	PHX1	PHX2
Corrugation depth	mm	5.8	5.8
Corrugation pitch	mm	9.5	9.5
Plate material	-	Stainless Steel	Stainless Steel
Plate conductivity	$W \cdot m^{-1}K^{-1}$	16.3	16.3

We used HX models that have been extensively validated as the verification baselines. For the air-to-refrigerant tube-fin HXs (TFHX1, TFHX2), we used the finite-volume HX model by Jiang et al. [5] as the baseline mode. The model adopts a network viewpoint allowing for arbitrary tube circuitry and mal-distribution of fluid inside the tube circuits. It implements a segment-by-segment approach within each tube to account for refrigerant flow pattern through the tube as well as air distribution across the heat exchanger.

The baseline model for the two plate HXs (PHX1, PHX2) was the finite-volume model by Qiao et al [6]. It divides the entire plate heat exchanger into multiple slices in the direction of fluid flow. For the channels in each slice, the wall temperatures are assumed to be constant such that each channel can be solved without the need of knowing the fluid condition in the adjacent channels. In the top level, all the slices are iterated using a successive substitution approach.

The baseline model for the water-to-refrigerant coaxial HX was the finite-volume model by Huang et al [108]. It tracks the fluid property change and the thermal and hydraulic performance variation along the length of flow channel. The entire heat exchanger length is divided into a given number of finite volumes (segments).

Table 5.5 shows the heat transfer and pressure drop correlations used for the baseline simulation of the two plate HXs. The correlations used for the two tube-fin HXs and the coaxial HX can be found in [49] and [108], respectively.

Table 5.5 Heat transfer and pressure drop correlation for plate HX simulation

	Condensation	Evaporation
Single-phase heat transfer	Muley and Manglik, 1999 [63]	Muley and Manglik, 1999 [63]
Two-phase heat transfer	Shah, 1979 [109]	Kim, 2007 [57]
Single-phase pressure drop	Muley and Manglik, 1999 [63]	Muley and Manglik, 1999 [63]
Two-phase pressure drop	Lockhart and Martinelli, 1949 [71]	Khan and Chyu, 2010 [75]

5.3.2.System-level verification method

5.3.2.1. Verification method

In the system-level verification, three vapor compression systems were used, as shown in Figure 5.5. TFHX1 and TFHX2 were used as the evaporator and the condenser for system 1, PHX1 and PHX2 for system 2, TFHX1 and CHX1 for system 3. The system refrigerant was R410A for all 3 systems. The modeling details of each system is described in 5.3.2.2.

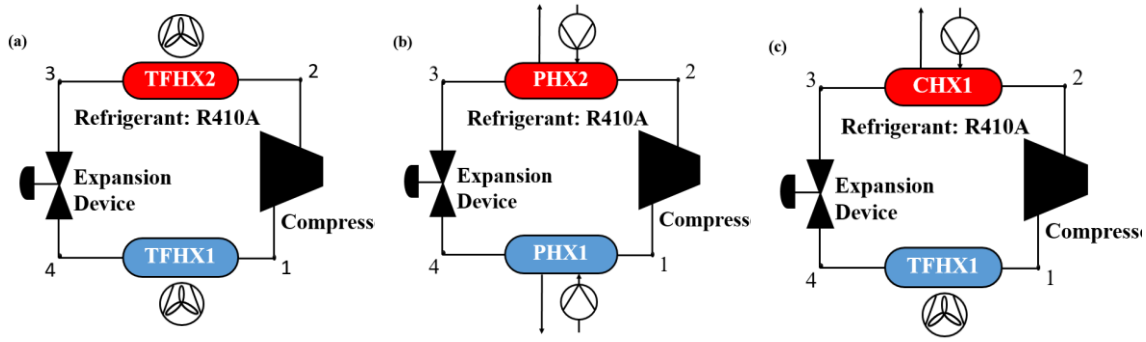

Figure 5.5: Schematics of (a) System 1: air-conditioning system, (b) System 2: water-source chiller system, (c) System 3: water-source air-conditioning system

The three systems were simulated at various testing conditions. The simulation conditions are described in Section 5.3.2.3. For each system, we first used the baseline finite-volume HX models to simulate the system performance. The results were set as the baseline. Then we simulated the system again, using the approximation-assisted models as the HX (condenser and evaporator) component model. The error between the baseline result and the approximation-assisted result is calculated by Eq.(30), where Y, in this case, stands for COP, system capacity, system power, and evaporator sensible heat ratio (SHR). The verification process was repeated for all simulation conditions.

5.3.2.2. System model details

Table 5.6 shows the modeling details of the three systems. The baseline HX models used in the system simulation were finite-volume based models, as described in Section 5.3.1.2. A ten-coefficient database compressor model was used in system 1 and system 3. The expansion device model was bypassed, and was instead represented with a simple isenthalpic process. Both compressor models were based on the coefficients of R410A supplied by the manufacturer. An efficiency-based model was used in system 2, with an isentropic efficiency of 0.85, a volumetric efficiency of 0.95, a mechanical efficiency of

1, and the displacement of 221 cc. The RPM of the efficiency-based compressor model was different at various simulation conditions. They are listed in Table 5.9.

Table 5.6 Modeling details of system 1, system 2 and system 3

	System 1	System 2	System 3
Application category	Air-source air-conditioning system	Chiller system	Water-source air-conditioning system
Nominal capacity	10 kW	60 kW	15 kW
Refrigerant	R410A	R410A	R410A
Evaporator	TFHX1	PHX1	TFHX1
Condenser	TFHX2	PHX2	CHX1
HX model (baseline)	Finite-volume model [5]	Finite-volume model [6]	Finite-volume model [5]
Compressor model	10-coefficient performance map	Efficiency-based model	10-coefficient performance map
System solution scheme	Component-based general-purpose simulation framework		

The three systems were simulated in the component-based simulation framework. The mathematical formulation of a four-component system can be found in section 3.2.1, and thus is skipped here for brevity. The design criteria for all three systems were suction superheat and condenser outlet subcooling. Their values at various simulation conditions are listed in Table 5.9. Broyden method [78] was used as the non-linear equations iteration scheme.

5.3.2.3. Simulation conditions

The simulation conditions of system 1 and system 2 follow ANSI/ASHRAE Standard 116 (2010) [110] and AHRI Standard 550/590 (2015) [111], respectively, as shown in

Table 5.7 and Table 5.8. For system 1, test A and B are wet conditions, and test C is dry condition. For system 2, outdoor EWT (entering water temperature) varies linearly from 29.4 °C at 100% load to 23.9 °C at 50% load, and is fixed at 18.3 °C for 25% load condition. The indoor LWT (leaving water temperature) and water $\dot{m}$ are kept constant for all conditions, and the indoor EWT is adjusted according to the load condition. The testing condition for system 3 follows AHRI Standard 320-98 (1998) [112]. Indoor air dry-bulb and wet-bulb temperature is 26.7 °C and 19.4 °C, respectively. Entering water temperature and leaving water temperature is 29.4 °C and 35 °C, respectively.

Table 5.7 System 1 simulation conditions (ASHRAE Standard 116 (2010) [110])

Tair (°C)	Test A	Test B	Test C (dry)
Outdoor dry-bulb	35.0	27.8	27.9
Indoor dry-bulb	26.7	26.7	27.7
Indoor wet-bulb	19.4	19.4	11.0

Table 5.8 System 2 simulation conditions (AHRI 550/590 (2015) [111])

Full- and part-load condition			100%	75%	50%	25%
Indoor	EWT	(°C)	12.22	11.23	9.71	8.19
	LWT	(°C)	6.67			
	$\dot{m}$ (kg/s)		2.268			
Outdoor	EWT	(°C)	29.44	23.89	18.33	18.33
	$\dot{m}$ (kg/s)		2.268			

Table 5.9 Design criteria and compressor RPM at different conditions

	System 1	System 2				System 3
	Test A, B, C	100%	75%	50%	25%	Test 1
Subcooling	5	9	8.0	8.4	7.4	4.61
Superheat	5	7	7.4	5.5	4.2	6.17
Compressor RPM	3600	3000	2197	1360	750	3600

5.3.3.Fluid property library and other specification

The thermophysical properties are calculated from the data library of NIST REFPROP Calculation Engine [79], augmented with curve-fits as described in [80]. The default REFPROP 9.1 settings were used to generate data and conduct property calculation. The full equation of state in REFPROP (and not pseudo-pure fluid) was used, in conjunction with the methods proposed in [80] to generate the curve-fits for the thermophysical properties.

The computer CPU on which the simulation tests were performed was Intel Xeon E3-1245 v5 @ 3.5GHz, with 4 cores and 8 logical processors. The RAM was 16 GB.

5.4.Results and discussion

5.4.1.HX-level verification results

Table 5.10 shows the input domains of the five HXs within which the 10,000 input points were generated to verify the approximation-assisted models. The air-side temperatures used to determine TFHX1 and TFHX2 domains are based on the A condition in Table 5.7. The water-side temperatures for PHX1 and PHX2 domains are based on the 100% load condition in Table 5.8. The water-side temperatures for CHX1 domain are the same as described in Section 0.

Table 5.10 HX input domains

HX ID-type		**TFHX1-Evap.**	**TFHX2-Cond.**	**PHX1-Evap.**	**PHX2-Cond.**	**CHX1-Cond.**
D	P (kPa)	863.8 ~1116.0	2537.7 ~3060.0	810.4 ~1001.7	2404.8 ~3031.3	1955.3 ~2392.9
	x (-) or T (K)	0.18~0.36	328~364	0.18~0.37	328~355	308~338

HX ID-type		**TFHX1-Evap.**	**TFHX2-Cond.**	**PHX1-Evap.**	**PHX2-Cond.**	**CHX1-Cond.**
	$\dot{m}$ (kg/s)	0.044~0.062	0.044~0.062	0.309~0.405	0.309~0.405	0.0728~0.109

5.4.1.1. Approximation accuracy

Table 5.11 and

Table 5.12 compare the statistics of HX performance approximation of the three models. Maximum absolute error (MAX) and mean absolute error (MAE) over the 10,000 trial points selected from the input domains from Table 5.10 are calculated for each model. MAE is given by

$$MAE = \frac{\sum_{i=1}^{10000} |\delta_i|}{10000} \tag{31}$$

where error δ is defined by Eq.(30).

Table 5.11 Statistics of TFHX1 and TFHX2 performance approximation for 10,000 trial points

HX domain		TFHX1 (Evap.)			TFHX2 (Cond.)		
Approximation-assisted model		Interpolation	Kriging	Three-zone model	Interpolation	Kriging	Three-zone model
ΔP	MAX(|δ|)	8.12%	7.45%	8.13%	18.66%	5.52%	11.67%
	MAE	1.6%	1.55%	1.62%	3.11%	0.61%	1.62%
Δh	MAX(|δ|)	9.22%	8.25%	21.65%	9.93%	6.22%	2.32%
	MAE	1.25%	0.86%	2.38%	0.52%	0.2%	0.25%
SHR	MAX(|δ|)	6.17%	3.43%		NA		
	MAE	0.92%	0.53%				

Table 5.12 Statistics of PHX1, PHX2 and CHX1 performance approximation for 10,000 trial points

HX Domain	Approximation-assisted model	ΔP		Δh	
		MAX(|δ|)	MAE	MAX(|δ|)	MAE
PHX1 (Evap.)	Interpolation	18.51%	3.6%	24.74%	2.24%
	Kriging	14%	3%	11.4%	1.93%
	Three-zone model	17.95%	3.43%	7.54%	0.86%
PHX2 (Cond.)	Interpolation	92.98%	15.32%	8.23%	1.06%
	Kriging	93.54%	14.27%	3.65%	0.45%
	Three-zone model	95.87%	14.23%	5.42%	0.54%
CHX1 (Cond.)	Interpolation	47.64%	3.61%	27.59%	3.79%
	Kriging	38.21%	2.87%	12.78%	1.06%
	Three-zone model	39.92%	3.10%	13.44%	1.82%

Figure 5.6 and Figure 5.7 compare the accuracy of the three models by breaking down the ten-thousand trial points into four error ranges. Each segment represents the percentage of the trial points falling within a certain error range.

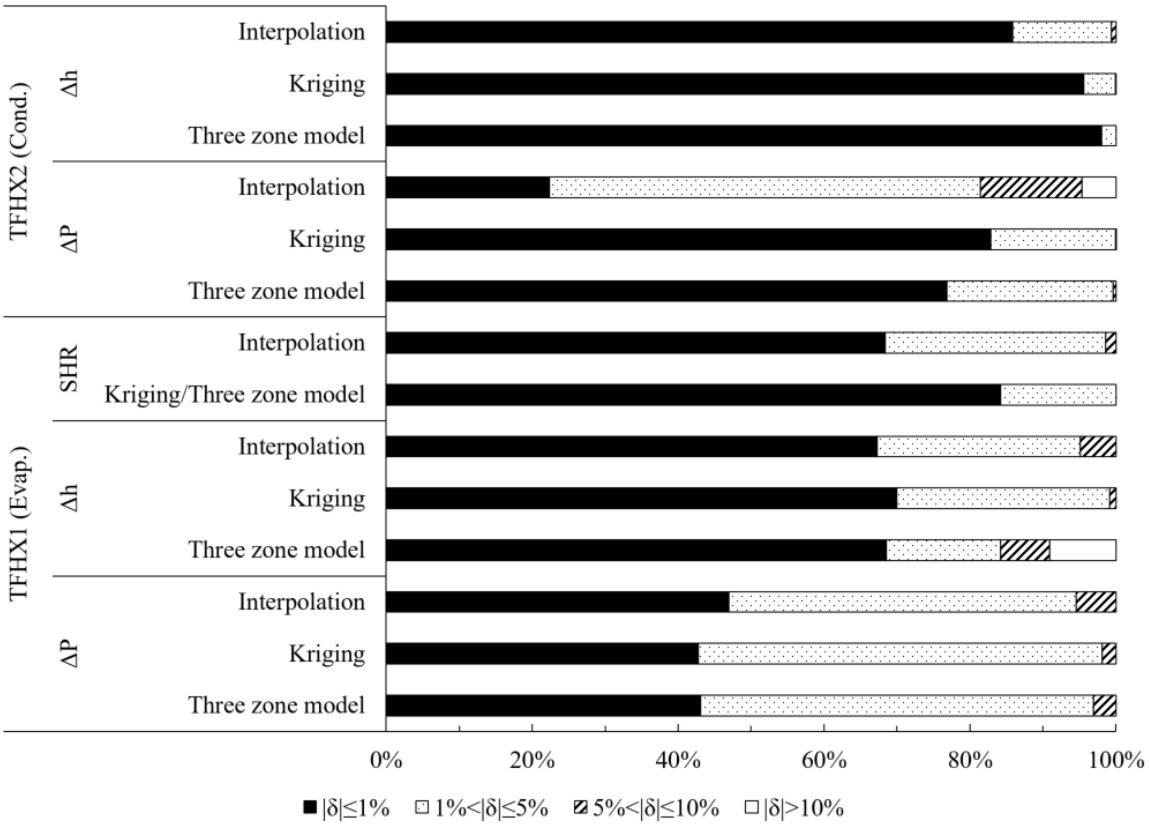

Figure 5.6 TFHX1 and TFHX2 performance approximation results at ten-thousand trial points by error range

The results show that the three models approximate Δ*P* with similar accuracy except for the tube-fin condenser (TFHX2), for which the interpolation-approximated Δ*P* has a MAE of 3.11% and MAX of 18.66%, largest among the three models. The percentage segment of the interpolation-approximated TFHX2 Δ*P* in [0, 1%] error range is notably less than that of the other two models (Figure 5.6). The similar Δ*P* approximation results by kriging black-box model and three-zone model indicate that the separate approximation of Δ*P* for each zone, though necessary for decoupling the hydraulic calculation from heat transfer calculation, does not help to increase approximation accuracy.

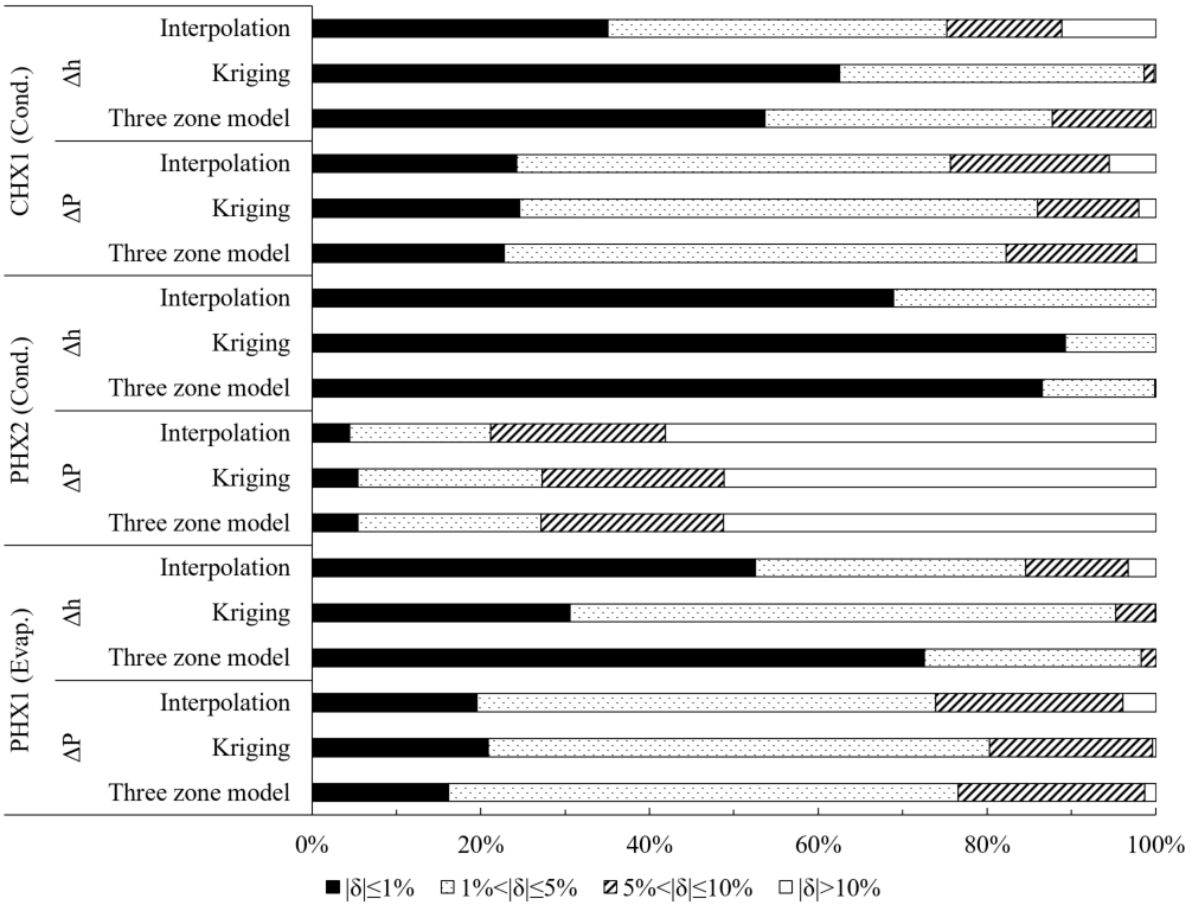

Figure 5.7 PHX1, PHX2, and CHX1 performance approximation results at ten-thousand trial points by error range

For TFHX1 SHR approximation, the kriging-approximated results (by kriging black-box model and three-zone model) are more accurate than those by interpolation. Kriging-approximated SHR has a MAE of 0.53% and MAX of 3.43%, almost half compared to the statistics of interpolation-approximated SHR. The percentage segments in Figure 5.6 also indicate the better accuracy of the Kriging-approximated SHR results.

For HX Δ*h* approximation, kriging black-box model and three-zone model have similar MAE and percentage distribution in the tube-fin condenser (TFHX2) domain and plate condenser (PHX2) domain, while the Δ*h* MAE for interpolation black-box model in these two domains is roughly twice the MAE by the other two models. In the coaxial

condenser (CHX1) domain, kriging black box model outperforms the other two models, while in plate evaporator (PHX1) domain, three-zone model outperforms the other two models. In tube-fin evaporator (TFHX1) domain, the three models have similar percentage segment within 1% error, but the three-zone model has the largest Δh MAE and an unusually large MAX.

To investigate the reason behind the large Δh error of three-zone model in TFHX1 (Evap.), its distribution in the input domain is plotted in Figure 5.8 (left). Inlet states associated with large error occurs at the light-colored region, with large P_{in}, large mass flow rate and small h_{in}. As shown in Figure 5.8(right), these inlet states lead to a two-phase condition at HX outlet. Δh approximation shows improved accuracy as the HX outlet quality increases. Finite-volume results reveal that when TFHX1 were operated at these conditions, there was vapor phase in the HX despite the two-phase outlet condition. On the other hand, if two-phase condition is arrived with no vapor coil (vap%=0), the approximation error is very small. It should be noted that TFHX1 is a multi-bank HX, where only frontal tubes will see the fresh air. This indicates that the large Δh error of three-zone model stems from the attempt to simulate a multi-bank HX with one equivalent coil.

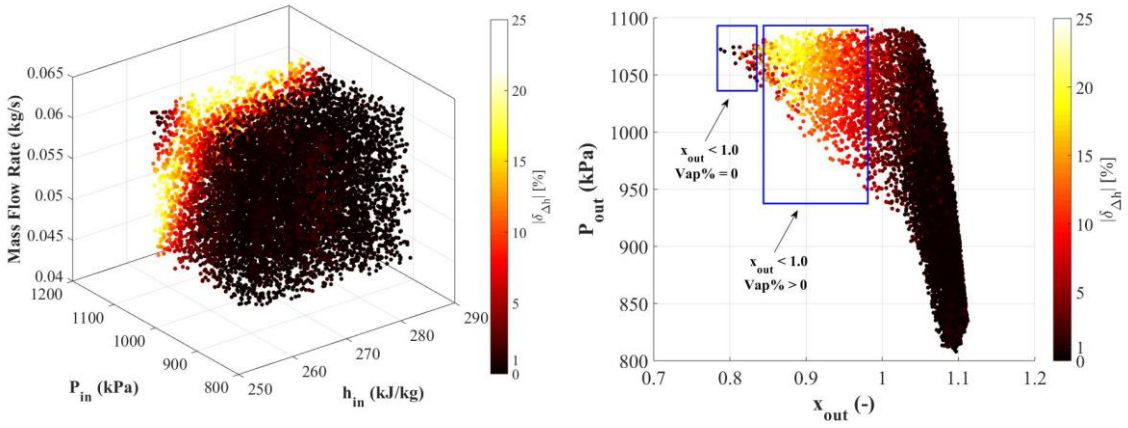

Figure 5.8 Three-zone model Δh error distribution in TFHX1 (Evap.) domains. Left: input domain, Right: output domain

Table 5.13 compares the Δ*P* and Δ*h* MAE over five HX domains of the three approximation models. The results show that among the three models, Kriging metamodel gave the most accurate approximation, with an overall Δ*P* and Δ*h* MAE of 4.46% and 0.9%, respectively.

Table 5.13 Comparison of Δ*P* and Δ*h* MAE of the three approximation models

	Interpolation	Kriging	Three-zone model
MAE (Δ*P*)	5.40%	4.46%	4.80%
MAE (Δ*h*)	1.77%	0.90%	1.18%

5.4.1.2. Computational efficiency

With the finite volume models, nearly all computational effort is spent evaluating thermodynamic properties [98]. Thus, the approximation models offers higher computational efficiency because they involve little property evaluation. For 100 HX runs, the simulation time of the finite-volume models ranges from 12s to 792s, depending on the HX geometries. It should be noted that the property calculation speedup [80] was applied to the finite-volume models. The simulation time for the 100 HX runs of the

Kriging and the interpolation metamodel model ranges from 0.07 to 0.09 s (0.7 – 0.9 ms per run). Three-zone model has more property evaluations than the other black box models, and thus its simulation time ranges from 0.2 to 0.5 s for 100 runs (2 – 5 ms per run), the longest among the three. The three approximation-assisted models could speed up the tube-fin HX simulation time by a factor of 60 to 170, and could speed up the plate HX simulation time by a factor of 1500 to 8000.

5.4.2.System-level verification results

5.4.2.1. System simulation errors

Figure 5.9 - Figure 5.11 show the simulation errors of the three systems at their respective test conditions by the three approximation-assisted models. COP, system capacity and system power simulated with the approximation models were compared against those with the baseline HX model. SHR was also compared for test condition A and B of system 1.

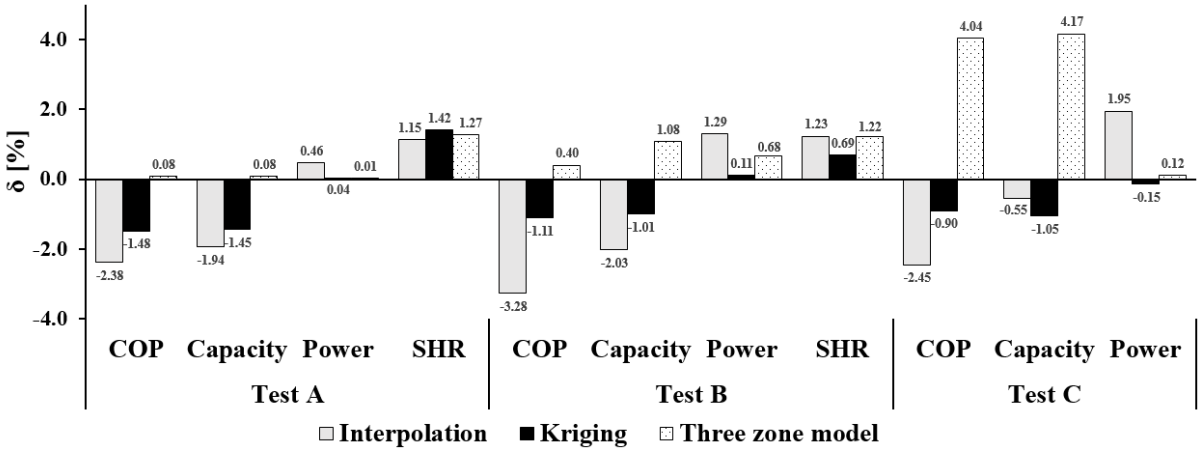

Figure 5.9 System 1 simulation errors

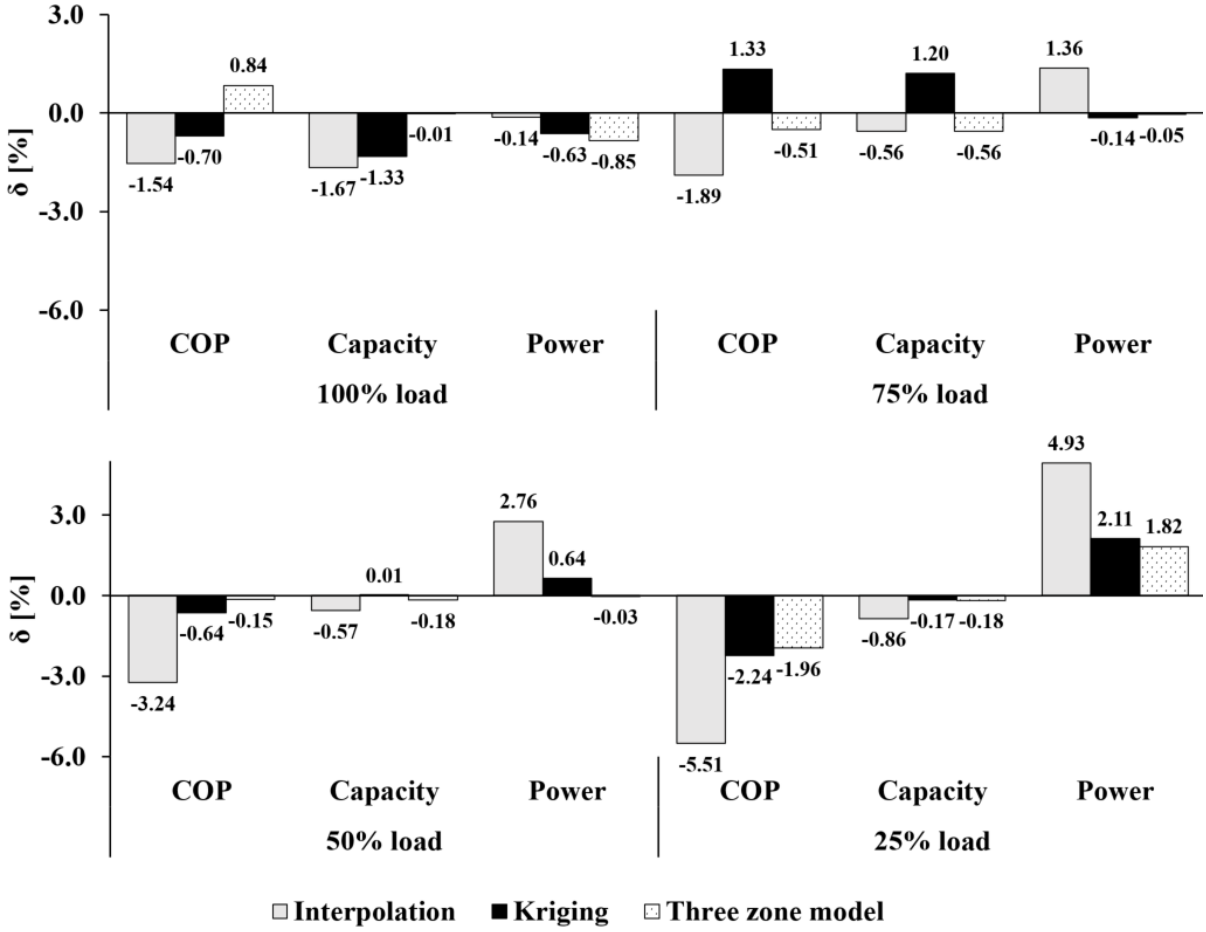

Figure 5.10 System 2 simulation errors

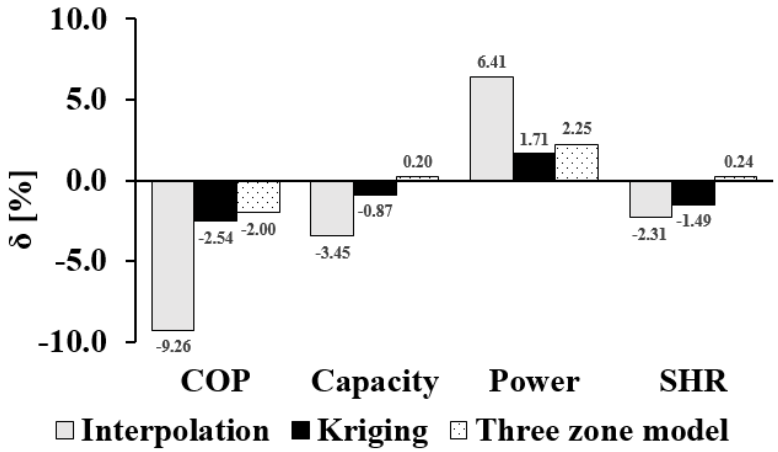

Figure 5.11 System 3 simulation errors

Table 5.14 compares the maximum absolute errors (MAX) for COP and capacity of the three approximation models. The results show that Kriging metamodel gave the most accurate results. Its largest COP and capacity errors were 2.54% and 1.45%, respectively.

Table 5.14 COP and capacity maximum absolute error of the three approximation models

	Interpolation	Kriging	Three zone model
MAX($\|\delta_{COP}\|$)	9.26%	2.54%	4.04%
MAX($\|\delta_{Q}\|$)	3.45%	1.45%	4.17%

The maximum errors of the three-zone model are those in test C of system 1 simulation. The system capacity simulated with the three-zone model has an error of 4.17%, leading to a 4.04% simulation error in COP. To understand this large error, Δh and ΔP errors of TFHX1 (Evap.) and TFHX2 (Cond.) by the three-zone model at each iteration of test C simulation were plotted in Figure 5.12. The figure shows TFHX2 (Cond.) performance approximation error was below 1% for all iterations. TFHX1 (Evap.) Δh error remained above 10% for most of the iteration path, and ended with roughly 9% at the final iteration, which must be the leading cause for the system capacity error. One should note that the 9% Δh error shown in Figure 5.12 is not equivalent to the 4.17% system capacity error shown in Figure 5.9, because the baseline simulation would take a completely different iteration path.

To investigate the reason behind the large Δh error of TFHX1 (Evap.), Table 5.15 and Figure 5.13 show the overall HX outlet quality (x_{out}) and the vapor coil percentage (vap%) by the three-zone model at each iteration, and the results by the baseline model at the same inputs. The baseline results show that at each iteration, the evaporator would arrive at two-phase outlet condition with vapor phase in the coil. This is the same

condition that leads to the unusually large Δh MAX of the three-zone model in Section 5.4.1. Therefore, the three-zone model gives large simulation error at test C because the multi-bank evaporator was subjected to insufficient heat transfer at dry condition, and the refrigerant in the rear bank was not fully vaporized.

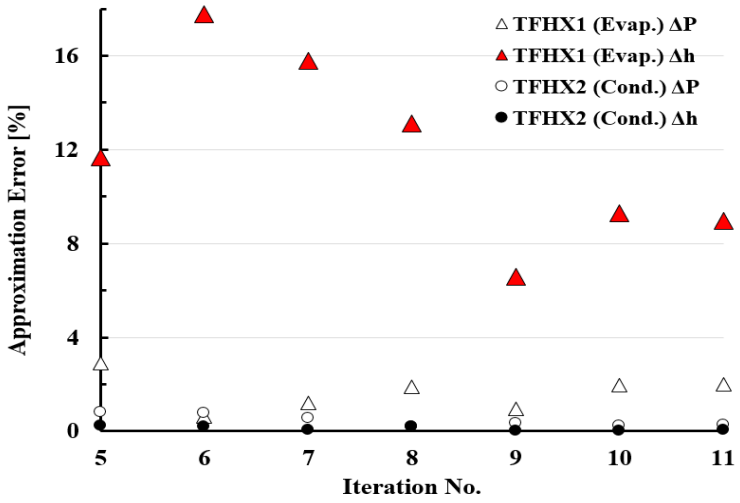

Figure 5.12 TFHX1 and TFHX2 simulation error by three-zone model along test C iteration path

Table 5.15 Comparison between TFHX1 result by three-zone model and baseline model along test C iteration path

Iteration No.	**Baseline result**		**Three-zone model**		$\lvert\delta_{\Delta h}\rvert_{TFHX1}$
	x_{out}	**vap%**	x_{out}	**vap%**	
1	0.71	15.91	0.77	0	11.66%
2	0.71	15.91	0.77	0	11.66%
3	0.71	15.91	0.77	0	11.66%
4	0.71	15.91	0.77	0	11.66%
5	0.71	15.91	0.77	0	11.66%
6	0.89	20.68	>1.0	5.78	17.78%
7	0.90	21.02	>1.0	8.44	15.79%
8	0.92	21.48	>1.0	11.99	13.10%
9	0.98	22.73	>1.0	20.77	6.59%
10	0.95	22.16	>1.0	17.05	9.27%

Iteration No.	Baseline result		Three-zone model		$\|\delta_{\Delta h}\|_{TFHX1}$
	x_{out}	vap%	x_{out}	vap%	
11	0.96	22.27	>1.0	17.35	8.96%

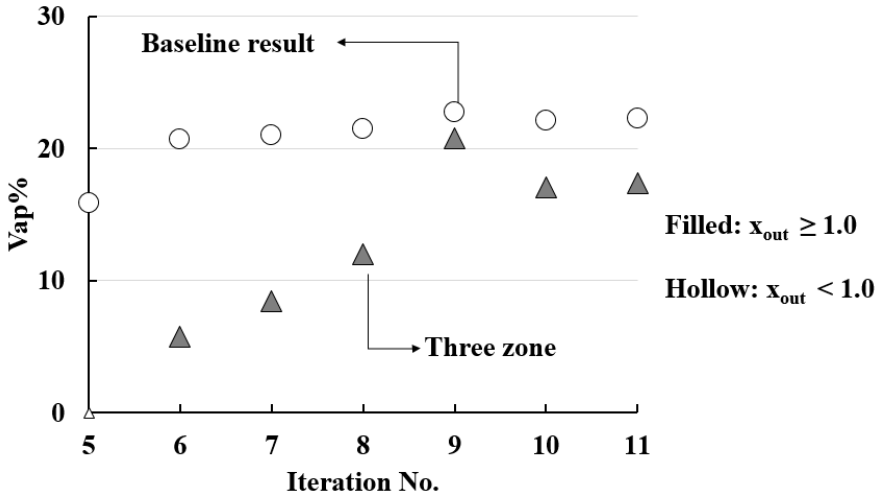

Figure 5.13 Comparison between TFHX1 result by three-zone model and baseline model along test C iteration path

5.4.2.2. Computational efficiency

Figure 5.14 - Figure 5.16 compare the simulation cost (simulation time and number of iterations) of different models for the three systems. It should be noted that the simulation time does not include the 27 sample runs. By using approximation-assisted models, the system simulation time was reduced to below one second, while the number of iterations were similar to those in the baseline simulation. At test A and B of system 1, simulation with interpolation metamodel could only be solved with carefully chosen initial guess values, therefore the corresponding number of iterations was the least among the all. Simulation of system 2 at part load with the baseline HX model required the initial guess values to be very close to the true solution. Otherwise, the iteration procedure would

terminate at correlation or property calculation failure during the baseline HX model execution. However, by using the approximation-assisted models, the simulation at these conditions could successfully converge with the default initial guess values.

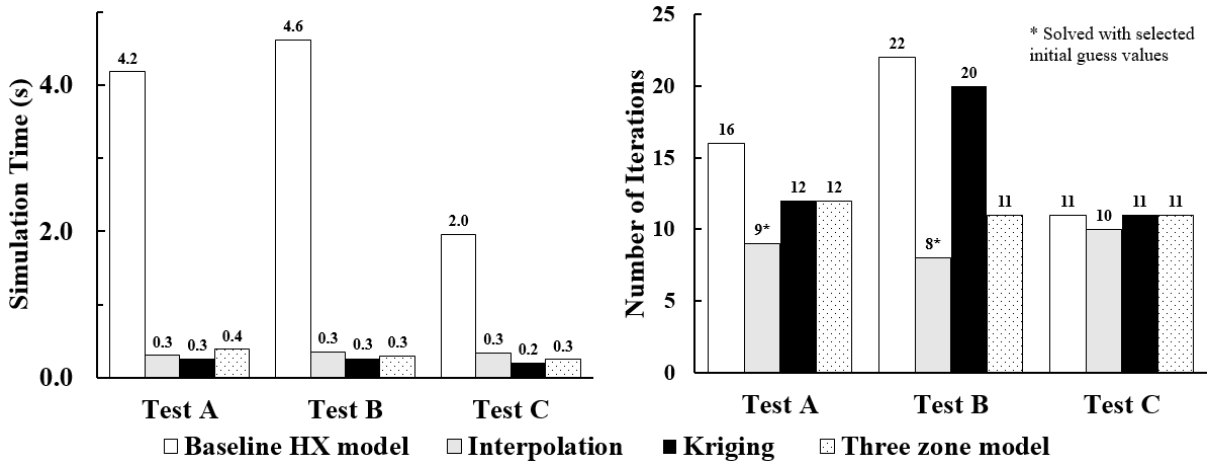

Figure 5.14 System 1 simulation cost comparison

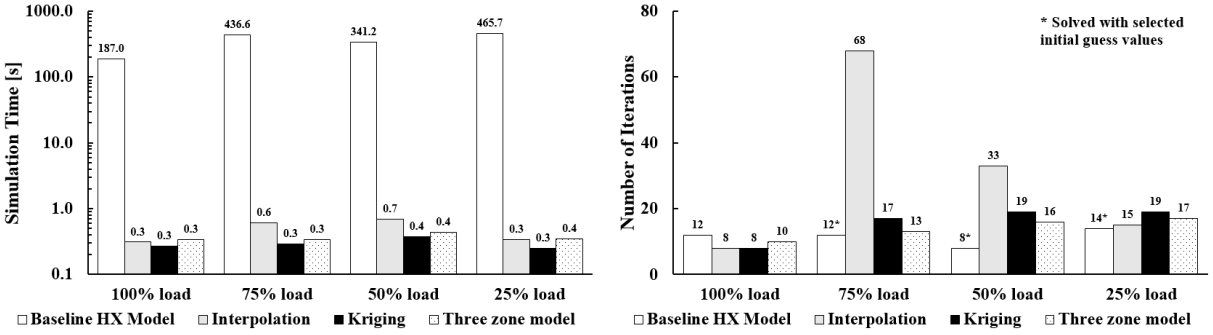

Figure 5.15 System 2 simulation cost comparison

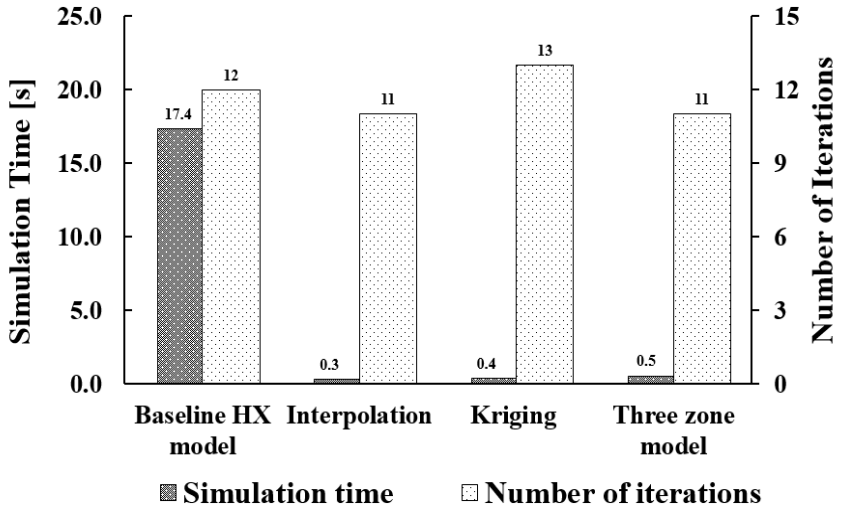

Figure 5.16 System 3 simulation cost comparison

5.5.Summary

This Chapter proposed and compared three HX performance approximation methods for steady-state vapor compression system simulation: interpolation black box model (interpolation metamodel), kriging black box model (kriging metamodel), and kriging-assisted three-zone model (three-zone model). The three approximation-assisted models were constructed using 27 samples and then verified against the baseline finite-volume HX model. On the HX-level verification, they were applied to approximate/simulate the performance of tube-fin HX, plate HX and coaxial HX at ten-thousand randomly selected inputs. On the system-level verification, the approximation-assisted HX models were used to simulate an air-source air-conditioning system, a chiller system and a water-source air-conditioning system at various conditions. The main conclusions are as follows:

a. For approximation of HX performance, Kriging metamodel gave the most accurate approximation with an overall ΔP and Δh MAE of 4.46% and 0.9%, respectively. The three-zone model predicts Δh with the least accuracy among all three models at those

operating conditions where the HX has an average two-phase outlet condition ($x_{out,avg} < 1.0$) but with refrigerant vapor existing in part of the coil (vap% > 0).

b. The approximation-assisted models sped up the tube-fin HX simulation time by a factor of 60 to 170, and sped up the plate HX simulation time by a factor of 1500 to 8000.

c. For system simulation, Kriging metamodel gave the most accurate results. Its largest COP and capacity errors were 2.54% and 1.45%, respectively. Simulation results with the three-zone model are not accurate for the simulation of system 1 at ASHRAE C condition. The reason is that at this condition (dry condition), the multi-bank evaporator was subjected to insufficient heat transfer, and therefore ended with a two-phase outlet condition ($x_{out,avg} < 1.0$), but meanwhile with superheated vapor in part of the coil (vap% > 0). This is consistent with conclusion a.

d. By using the approximation-assisted models, the system simulation time was sped up by a factor of 10 to 600, depending on testing conditions. Simulation of system 2 at part load with the baseline HX model required the initial guess values to be very close to the true solution. Simulation at these conditions with approximation-assisted models could successfully converge with the default initial guess values.

6. Investigation into steady-state simulation convergence and its improvement

This Chapter aims to explore the options to advance the robustness for the steady-state simulation of a standard four-component vapor compression system.

6.1. Background and motivation

Steady-state simulation of vapor compression systems is finding the solution of a system of nonlinear equations:

$$\text{given } F: R^n \to R^n \text{, find } \vec{x}_* \in R^n \text{ such that } F\left(\vec{x}_*\right) = 0 \tag{32}$$

Take a standard four-component system as an example (Figure 6.1) that uses subcooling and superheat as the design criteria, the unknown variables and the system of nonlinear equations are as follows.

$$\vec{x} = \left[P_{1,1}, h_{1,1}, P_{1,2}, P_{3,1}\right]^T \tag{33}$$

$$F = \begin{bmatrix} P_{1,1} - P_{4,1} \\ \left(\dot{m}h\right)_{1,1} - \left(\dot{m}h\right)_{4,1} \\ SC_{2,2} - a \\ SH_{4,1} - b \end{bmatrix} \tag{34}$$

The constants a and b are user-specified design parameters for the condenser outlet subcooling and suction superheat. The methodology to arrive at the above-mentioned formulation is elaborated in Section 2.4, and therefore is skipped here for brevity.

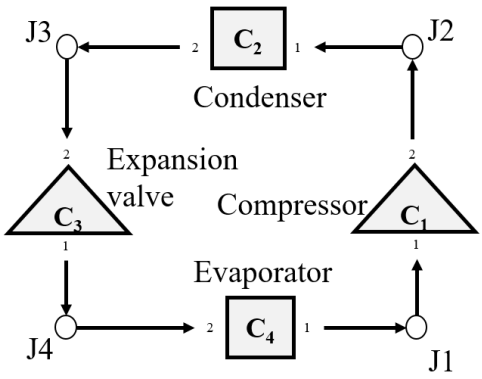

Figure 6.1 Example schematic of a standard 4-component system

Due to the nonlinear nature of the problem, the solution is almost always obtained through an iterative process: we propose an initial guess of $\vec{x}_0$, and then rely on certain methods to generate a sequence of points, $\vec{x}_i$, that we hope come increasingly close to the solution $\vec{x}_*$. Newton and quasi-Newton iteration schemes are one of these methods, in which a linear approximation to F is created by Taylor expansion at the current point,

$$\tilde{F}(\vec{x}_i + \vec{p}) = F(\vec{x}_i) + B(\vec{x}_i) \cdot \vec{p} \tag{35}$$

where B is either the Jacobian matrix or the Jacobian approximation at the current point. There are plenty of Jacobian approximation techniques, and the most well-known method is the secant update proposed by C. Broyden [78]. And then, the following schemes are applied from a starting guess point $\vec{x}_0$ until the iteration converges to the true solution.

$$\begin{aligned} B(\vec{x}_i) \cdot \vec{p}_i &= -F\left(\vec{x}_i\right) \\ \vec{x}_{i+1} &= \vec{x}_i + p_i \end{aligned} \tag{36}$$

It has been rigorously proven [78] as a fundamental theorem of numerical mathematics that Newton method and secant method (or Broyden method) are featured

with local q-quadratically convergence, provided a good starting guess $\vec{x}_0$ and nonsingular Jacobian at the true solution $\vec{x}_*$. The theorem can also be interpreted such that the radius of convergence of these methods is inversely proportional to the relative nonlinearity of F at $\vec{x}_*$ [78]. However, the theorem does not provide practical guidance to evaluate, assess, and predict the 'radius of convergence'. Calculating the Lipschitz constant of the Jacobian matrix (or its approximation) is one option in theory. However, in practice it is virtually always more work to estimate the Lipschitz constant accurately than to just try one of these methods and see whether it converges [78]. Moreover, the theorem does not shed light on what properties comprise a 'good starting guess' for a particular problem. And getting close enough constitutes the major part of the computational effort in practice.

Based on the aspects mentioned above, the rigorously proven theorem on Newton and quasi-Newton methods alone does not guarantee the successful implementation of these methods in the real-world problems. There is little literature on the methods or insights to fill the gap between the theorem and vapor compression system simulation. Therefore, this chapter aims to explore the options of convergence improvement on the basis of the fundamentals of Newton's method, and to understand the convergence characteristics of a standard four-component vapor compression system simulation.

6.2. Development and assessment of convergence improvement approaches

In general, there are three assumptions underlying Newton's and quasi-Newton methods for nonlinear equations **F**:

i. The initial guess $\vec{x}_0$ is within the radius of convergence of **F** at the true solution $\vec{x}_*$;

ii. $J(\vec{x}_*)$ is not singular;

iii. $J(\vec{x}_i)$ is not singular nor ill-conditioned.

Based on the above-mentioned assumptions, there are two potential options to improve the convergence of vapor compression system simulation. First, although evaluating i and ii seems almost impossible in practice, iii offers a viable starting point: to evaluate the Jacobian matrix at the initial guess point. Second, we can resort to the basic idea of any nonlinear algorithm: combine a global convergent strategy with a fast local strategy. The global strategy serves to reach the vicinity of the true solution. The local strategy accomplishes the eventual convergence.

6.2.1.Initial guess screening with Jacobian matrix analysis

As shown in Eq.(35), at each iterate, the Newton's or quasi-Newton method uses the linear portion of the Taylor series expansion to approximate the nonlinear equations **F** at the current point. However, if **F** is subjected to high nonlinearity at the current point, the error between the true **F** and the linear portion of the Taylor series around the current point will be large, nullifying the effectiveness of these methods.

One efficient way to evaluate the nonlinearity of the problem at the current step is to calculate the condition number of the Jacobian matrix of the current point [78, 113],

$$\kappa(J_i) = \left\| J\left(x_i\right) \right\| \cdot \left\| J^{-1}\left(x_i\right) \right\| \tag{37}$$

where $\|\cdot\|$ is the matrix Euclidean norm. The larger the condition number, the nearer of the Jacobian matrix to singularity, and the higher nonlinearity of the problem at the current step.

Thus, the first approach uses the condition number of the first Jacobian matrix as the starting screening criterion. We calculate the Jacobian condition number at different initial guess points, and reject those associated with large condition numbers.

6.2.2. Approximation-assisted (AA) global convergence with finite-volume (FV) local convergence

In the simulation of vapor compression systems, the HX model is usually the most numerically challenging component. The investigation of the approximation-assisted HX models in Chapter 5 shows that, not only did these models speed up the system simulation time, they solved cases that were unsolvable with the finite-volume models. This suggests that, using AAHX model decreases the nonlinearity of the system of nonlinear equations, and thus increases the radius of convergence. Therefore, the iteration can achieve convergence with a guess point relatively further from the true solution.

To take advantage of this characteristics, the second approach employs AAHX in the global iteration process, and switches to finite-volume HX for final convergence. It uses the solution from the approximation-assisted simulation as the initial guess for the finite-volume based iteration.

6.2.3. Assessment method

As mentioned in the summary of Chapter 5, simulation of system 2 (water-source chiller system) at part load with the baseline HX model required the initial guess values to be very close to the true solution. Simulation at these conditions with approximation-assisted models could successfully converge with the default initial guess values.

Due to its unique convergence characteristics, the water-source chiller system was used to assess the efficacy of the two convergence improvement approaches in the

current Chapter. For the simulation condition, we selected the 75% part load condition. The system description, component modeling approach, and the simulation condition of the chiller system are elaborated in section 5.3.2, and thus are skipped here for brevity.

In the first approach, the system simulation was repeated at a series of initial guess point. The equation formulation of a 4-component system is given in Eq.(33) and (34). There are 4 unknown variables. However, we only need to provide estimations for the initial suction pressure, $(P_{1,1})_0$, and the initial discharge pressure, $(P_{1,2})_0$. They can be given in the form of saturated suction temperature (SST) and saturated discharge temperature (SDT). The initial guess for the rest two can be estimated based on basic thermodynamic relations and vapor compression system knowledge.

The initial suction pressure $(P_{1,1})_0$ was varied from SST of 274 to 284 K, with an increment of 1 K per run. The initial discharge pressure $(P_{1,1})_0$ was varied from SDT of 300 to 320 K, with an increment of 2 K per run. The initial $P_{3,1}$ would use the same value as $(P_{1,1})_0$, since they are both low-side pressures. The initial $h_{1,1}$ was calculated based on $(P_{1,1})_0$ and the user-defined superheat value. It should be noted that these dependent relations only apply to the initial guesses. During the iteration, the values of the 4 variables will be adjusted by the nonlinear equation schemes.

In each simulation, the condition number of the initial Jacobian matrix was recorded, as well as the normalized energy balance which is given in Eq.(7). So we could observe the correlation between the magnitude of the Jacobian condition number and the simulation convergence. The results would be further used to evaluate the efficacy of the first approach.

In the second approach, the initial suction pressure and initial discharge pressure were randomly selected from their respective saturated temperature window. The total number of test runs is 50. For each initial guess point, the procedures were as follows.

i) First, conduct the baseline simulation using finite volume HX models.

ii) Switch the HX models to approximation-assisted models. Conduct the simulation at the same initial guess point as step i.

iii) Switch the HX models back to finite volume models. Use the solution from step ii as the new guess point. Conduct the simulation again for the local convergence.

The normalized energy balance and the simulation time of step i and iii were recorded separately. In addition, we categorize the solutions of step iii into 3 sets.

$$S_1 = \left\{ x_* \,|\, \left|\Delta_{E,iii}\right| < 0.5 \right\} \tag{38}$$

$$S_2 = \left\{ x_* \,|\, \left|\Delta_{E,iii}\right| < \left|\Delta_{E,i}\right| \right\} \tag{39}$$

$$S_3 = \left\{ x_* \,|\, t_{iii} < t_i \right\} \tag{40}$$

S_1 represent the well-converged solutions by using the second approach. S_2 represents the solutions with improved convergence comparing to the baseline simulation. S_3 represents the solutions with reduced computational time comparing to the baseline. When a solution is in the intersection of S_1 and S_2 ($S_1 \cap S_2$), the simulation is considered to be effectively improved by the second approach in terms of convergence. When a solution is in the intersection of all 3 sets ($S_1 \cap S_2 \cap S_3$), the simulation is considered to be strictly improved in terms of both convergence and computational time.

6.3. Results and discussion

6.3.1. Testing results of the improvement approaches

Ideally in the first approach, we want to use the condition number of the Jacobian matrix at the initial point, $\kappa(J_0)$, as a criteria to filter out certain initial guess points. We know that the larger the condition number, the higher nonlinearity at the current point. However, we do not exactly know the threshold of this number above which we shall reject the initial guess point.

To gain a better insight into the correlation between the magnitude of $\kappa(J_0)$ and the simulation convergence, Table 6.1 compares the convergence rate at different threshold value of $\kappa(J_0)$. When we selected the threshold value as 50, there were 57 test runs in total with $\kappa(J_0)$ less than this threshold value, and there were 41 successfully converged cases out of these 60 test runs. So the convergence rate was 72%. The total number of the test runs with $\kappa(J_0)$ larger than the threshold was 41. Out of these 44 test runs, only 8 successfully converged. The convergence rate was 20%. As we increased the threshold value from 50 to 600, the convergence rate of the below-threshold test runs dropped from 72% to 54%, and that of the above-threshold test runs dropped from 20% to 0%. This trend is more vividly reflected in the bar chart of Figure 6.2.

Table 6.1 Simulation convergence rate under different $\kappa(J_0)$ thresholds

$\kappa(J_0)$ threshold	Test runs with $\kappa(J_0)$ below threshold			Test runs with $\kappa(J_0)$ above threshold		
	Total number	Number of converged cases	Convergence rate	Total number	Number of converged cases	Convergence rate
50	57	41	72%	41	8	20%
100	71	43	61%	27	3	11%
150	76	44	58%	22	2	9%
200	79	44	56%	19	2	11%
500	83	45	54%	15	1	7%
600	85	46	54%	13	0	0%

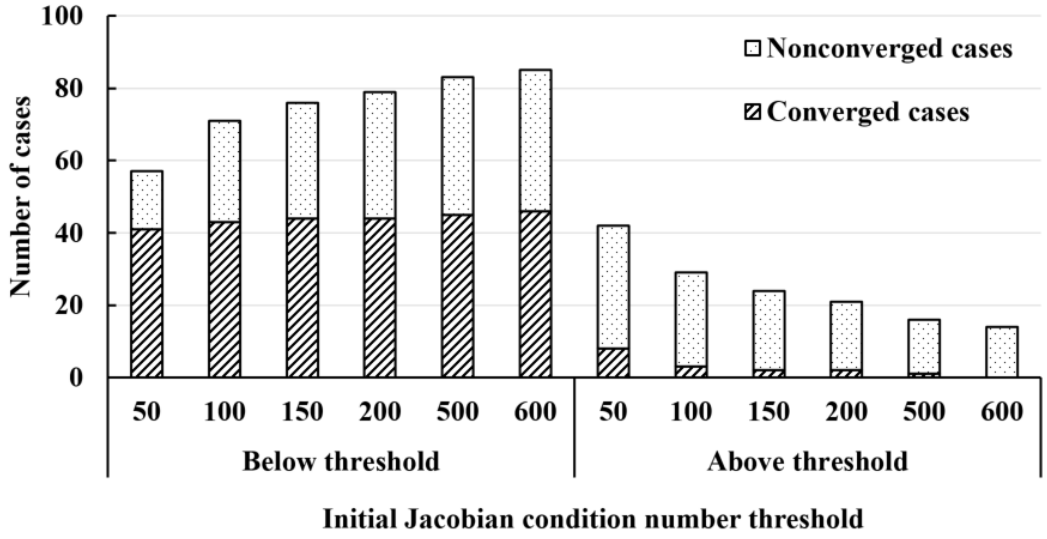

Figure 6.2 Simulation test runs breakdown at different $\kappa(J_0)$ thresholds

There are 3 messages that we can draw about the first approach from the testing results. First, the smaller the $\kappa(J_0)$, the higher chance of successful convergence at the current initial guess point. However, small value of $\kappa(J_0)$ did not necessarily guarantee simulation convergence. Second, the larger the $\kappa(J_0)$, the less chance of successful

convergence at the current initial guess point. When an initial guess point presents a large $\kappa(J_0)$, although it still has a certain chance of the successful convergence, from a practical point of view, it is more worthwhile to try a different initial guess point. Third, when $\kappa(J_0)$ was neither too small nor too large (in the range of 100 - 500), the simulation convergence rate was in the range between 50% and 60%, so it is difficult to draw a conclusion on the correlation between $\kappa(J_0)$ and simulation convergence in this particular range. This suggests that initial guess screening based on $\kappa(J_0)$ alone is not enough, and other screening criteria may be needed.

Table 6.2 summarizes the testing results for the second approach: approximation-assisted global convergence and finite-volume based local convergence. The definition of each set in the table is given in section 6.2.3. The results show that out of the 50 test runs, only 19 were effectively improved by the second approach in terms of convergence. The success rate was 38%. If we take into account the computational time, the success rate was further decreased to 28%. The results suggest that the second approach does not lead to convergence improvement as expected.

Table 6.2 Testing results of the 2nd convergence improvement approach

S_1	S_2	S_3	$S_1 \cap S_2$	Percentage	$S_1 \cap S_2 \cap S_3$	Percentage
27	27	37	19	38%	14	28%

6.3.2.Analysis and diagnostics of a typical test run

In the previous section, we have learned that the magnitude of $\kappa(J_0)$ does not provide the full picture about the convergence characteristics of the system simulation.

Therefore, in this section, we will take a more micro approach to understand the factors that influence the simulation convergence. Table 6.3 lists the detailed testing results of the first approach at a fixed initial suction pressure. We noticed that test No. 7 in the table was a unique case. It had a very small $\kappa(J_0)$, and yet it failed to converge, while its neighboring test run (test No. 6) successfully converged. Therefore, we decided to pick No. 7 for a more detailed analysis and diagnostics.

Table 6.3 Testing results of the first approach at initial SST = 274 K

Test No.	$(P_{1,1})_0$	$(P_{1,2})_0$	$\kappa(J_0)$	Δ_E
1	P_{sat}(T = 274 K)	P_{sat}(T = 300 K)	24	-0.04%
2	P_{sat}(T = 274 K)	P_{sat}(T =302 K)	21	0.02%
3	P_{sat}(T = 274 K)	P_{sat}(T =304 K)	19	-0.09%
4	P_{sat}(T = 274 K)	P_{sat}(T =306 K)	16	-0.05%
5	P_{sat}(T = 274 K)	P_{sat}(T =308 K)	96	0.01%
6	P_{sat}(T = 274 K)	P_{sat}(T =310 K)	11	-0.05%
7*	P_{sat}(T = 274 K)	P_{sat}(T =312 K)	5	9.01%
8	P_{sat}(T = 274 K)	P_{sat}(T =314 K)	7	6.38%
9	P_{sat}(T = 274 K)	P_{sat}(T =316 K)	56	Failed
10	P_{sat}(T = 274 K)	P_{sat}(T =318 K)	9	-0.06%

We first compared the paths of the 4 unknown variables at 3 different iterations (1st, 2nd, and final) against those in test No.6. As shown in Table 6.4, the two low side pressures, $P_{1,1}$ and $P_{3,1}$, did not take consistent directions at the 2nd iteration. Comparing to the initial value at the 1st iteration, the suction pressure at the 2nd iteration ($P_{1,1}$) went up slightly, while the evaporator inlet pressure ($P_{3,1}$) went for an opposite direction, so that $P_{3,1}$ was lower than $P_{1,1}$ at the 2nd iteration. However, these inconsistent pressure directions does not conform to the basics of vapor compression system, since the pressure drop in any HX cannot be lower than zero. In test No. 6, as a contrary, the low side

pressures were adjusted in a much more thermodynamically-reasonable manner. Both $P_{1,1}$ and $P_{3,1}$ went up at the 2nd iteration, and $P_{3,1}$ was slightly higher than $P_{1,1}$, allowing for a non-zero pressure drop in the evaporator. The inconsistent direction of the low side pressures indicates that the numerical behavior of some component(s) at the initial point of SST = 274 and SDT = 312 K is sending confusing messages to the iteration schemes.

Table 6.4 Iteration path comparison between test No. 6 and 7

Test No.	Iteration No.	Unknown variables			
		$P_{1,1}$ (kPa)	$h_{1,1}$ (kJ/kg)	$P_{1,2}$ (kPa)	$P_{3,1}$ (kPa)
7	1	820	431	2352	820
	2	849 (↑)	431	2337	797 (↓)
	Final	820	431	2352	820
6	1	820	431	2239	820
	2	899 (↑)	432	2401	903 (↑)
	Final	901	432	2358	907

To further visualize the component numerical behavior in test 7, we performed a component sensitivity analysis on the two HXs. We retrieved the HX input parameters, which are mass flow rate, inlet enthalpy, and inlet pressure, at the 1st iteration. Then we perturbed the three parameters individually to find out how the HX performance would respond to the input parameters. Figure 6.3 shows how the pressure drop over the evaporator and condenser varied with respect to one of the three input parameters, with the other two held constant. The values of the x- and y-axis were normalized as follows,

$$y^* = \frac{y - y_b}{y_b}, y = \Delta P_{HX}$$
$$x^* = \frac{x - x_b}{x_b}, x = \dot{m}, P_{in}, h_{in} \quad (41)$$

where y_b and x_b represents the baseline values from test No.7.

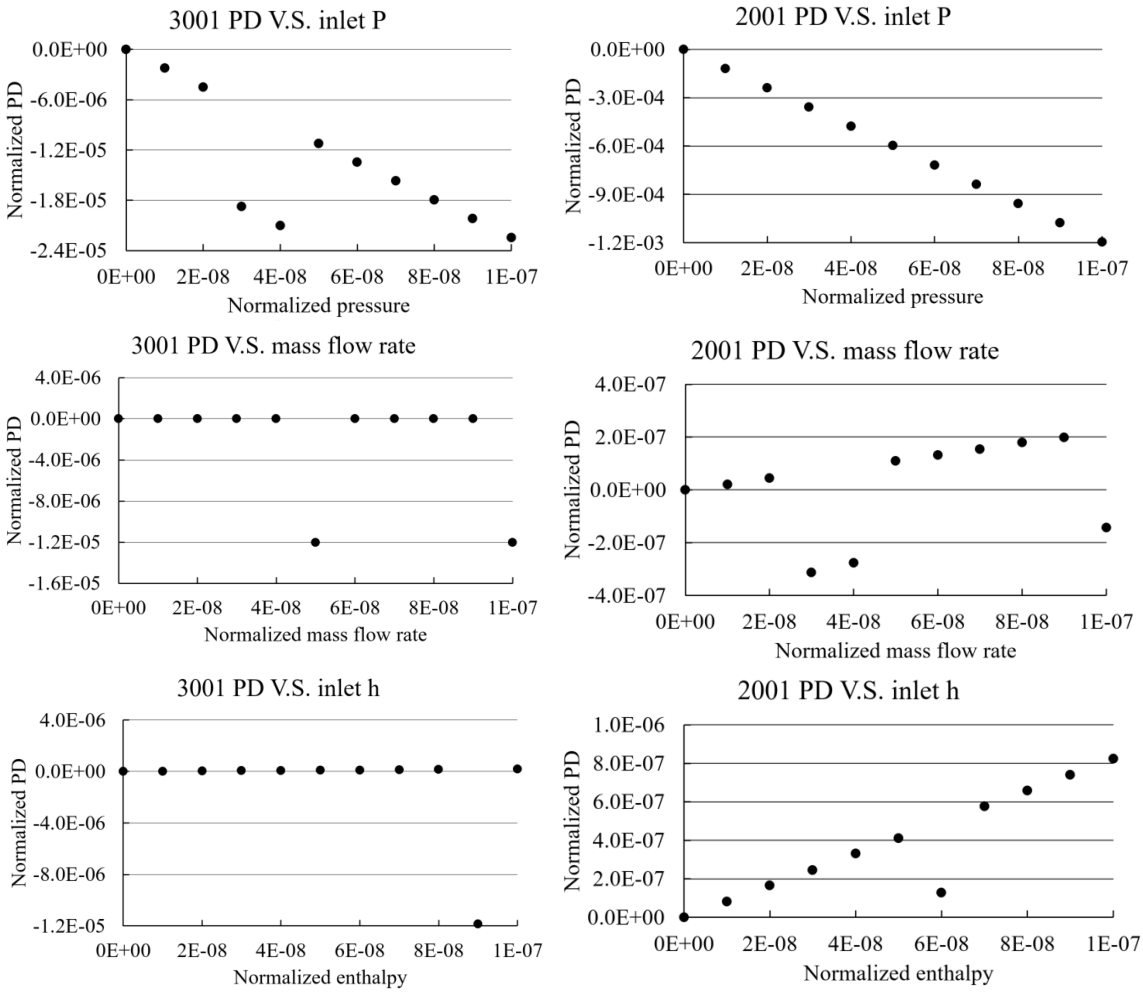

Figure 6.3 Sensitivity analysis results of the ΔP with respect to evaporator (3001) and condenser (2001) input parameters

The evaporator ΔP presented nonlinearity with respect to all the three input parameters at the initial point: it has a variable partial derivative with respect to each input parameter in a very small region ($1\times10^{\wedge-7}$). The condenser ΔP also presented nonlinearity with respect to the input parameters, except for the inlet pressure. The enthalpy change of the two HXs presented the exactly same curves with respect to the HX input parameters, and thus are not shown.

The sensitivity analysis results support the implication that the numerical behavior of some component(s) is sending confusing messages at the 1st iteration to the derivative-

based iteration scheme. Therefore, we performed 2 additional tests with the initial point at test No.7, in which we changed the pressure drop calculation method in the HX. The results are shown in Table 6.5. The results show that for test No. 7, by using fixed value ΔP in the evaporator, the low-side pressures no longer undertook inconsistent directions at the 2nd iteration. And the simulation successfully converged. On the other hand, using fixed value ΔP in the condenser was not effective measures.

Table 6.5 Test 7 results with alternative HX ΔP calculation method

No.	Condenser ΔP calculation method	Evaporator ΔP calculation method	Low-side pressure direction consistency at 2nd iteration	Successul convergence
7	Correlation	Correlation	Not consistent	No
7.a	Correlation	Fixed value pressure drop	Consistent	Yes
7.b	Fixed value pressure drop	Correlation	Not consistent	No

The analysis and diagnostics of test No.7 suggest that the simulation convergence failure may have a strong correlation with nonlinear behaviors of the component models at the initial guess point. Moreover, the simulation convergence may be improved by using a different approach to characterize the HX performance.

6.3.3.Applying a diagnostics procedure to the non-converged cases

From the microscopic analysis of a typical test run, we drew the conclusion that the simulation convergence may be correlated with the nonlinearity of the component models, in particular HX models at the initial guess point. Therefore, we summarized the test run results from the first approach, as shown in Figure 6.4. There were 98 test runs in total, in which 47 cases successfully converged and 51 cases failed to converge. Out of

the 51 non-converged cases, 42 cases (82%) presented HX nonlinearity at the initial guess point $\vec{x}_0$. Moreover, there were 63 cases associated with HX nonlinearity at $\vec{x}_0$, of which 66% failed to converge. And there were 34 cases free from HX nonlinearity at $\vec{x}_0$, of which 74% successfully converged.

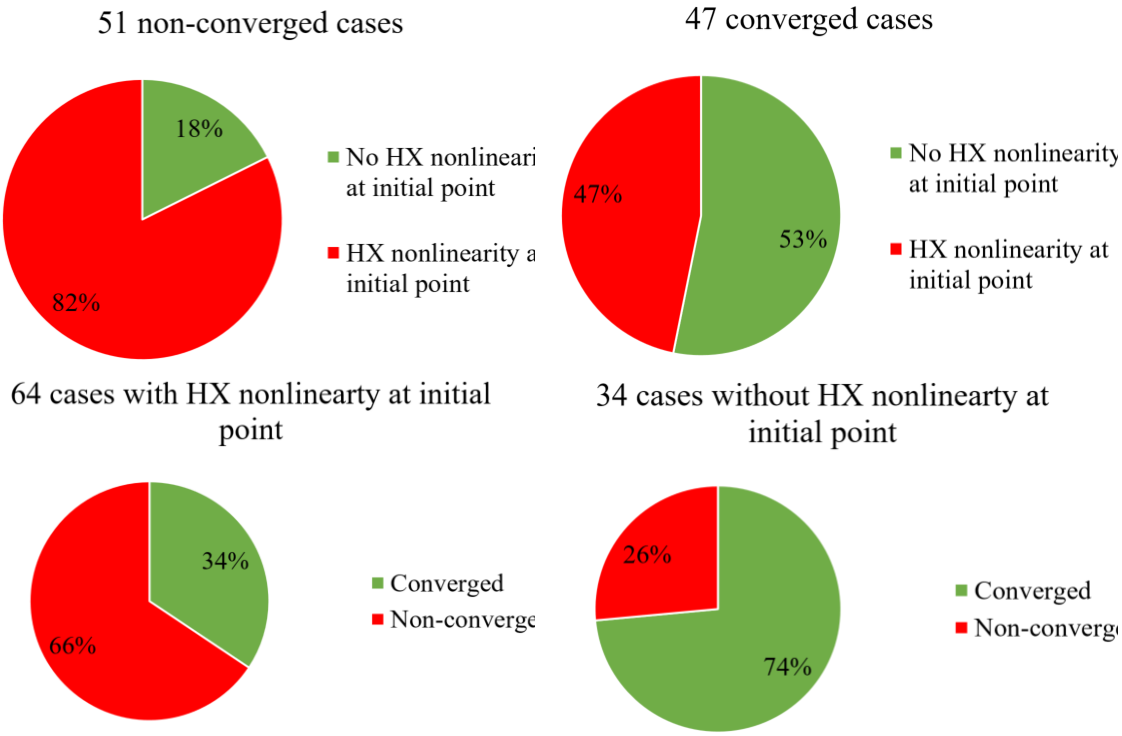

Figure 6.4 Statistics of the 98 test runs in the first approach

The statistics of the 98 test runs also supports the correlation between component nonlinearity and simulation convergence. Based on the analysis results, we proposed a standard diagnostics procedure to the 51 non-converged cases, as listed in Table 6.6. In this procedure, we first changed the pressure drop calculation method in the evaporator. The evaporator was the last component to be executed in each iteration, and the change in HX pressure drop is expected to have small impact on the system solution. If this was not effective, we would go one step further to change the heat transfer correlation (HTC) for

the evaporator. If not effective, we would change the pressure drop calculation method in the condenser, and then the heat transfer correlation. The last step in the procedure is to change the correlations in both the condenser and evaporator.

Table 6.6 Standard diagnostics procedure and the diagnostic results

Diagnostics procedure step	Description	Number of converged cases
1	Using fixed value for evaporator ΔP calculation	16
2	Using fixed value ΔP and/or alternative HTC for evaporator	24
3	Using fixed value for condenser ΔP calculation	6
4	Using fixed value ΔP and/or alternative HTC correlation for condenser	1
5	Changing hydraulic and heat transfer characterization methods for both evaporator and condenser	0
	Total number	47

As shown in Table 6.6, 16 cases successfully converged with step 1, and 24 cases with step 2. Six cases converged with step 3, and 1 case with step 4. Step 5 was not effective for any of the cases that were not solved in the previous steps. The diagnostics procedure eventually helped 47 cases achieve eventual convergence. And 4 cases were not solved by the procedure. The results show that by changing the characterization methods in the evaporator, 40 out of 51 non-converged cases could successfully converge. This suggests that for the current test system, the evaporator model was the main cause for the convergence failure.

We further compared these cases before and after the diagnostics procedure was applied. Table 6.7 listed the number of cases associated with HX nonlinearity at $\vec{x}_0$

before and after each procedure. The results show that for the 16 cases converged after step 1, there were 12 and 9 cases presenting nonlinearity in the evaporator performance before and after step 1 was applied, respectively. For the 24 cases that converged after step 2, 21 cases presented nonlinearity evaporator performance at $\vec{x}_0$, none of which was associated with nonlinearity anymore after step 2 was applied. For the 6 cases that converged after step 3, there were 5 and 3 cases presenting nonlinearity in the condenser performance before and after step 3 was applied, respectively. For step 4, the condenser nonlinearity still existed before and after the diagnostics.

Table 6.7 Number of cases presenting HX performance nonlinearity at the initial point before and after the diagnostics procedure

Diagnostics procedure step		Evaporator nonlinearity at $\vec{x}_0$			Condenser nonlinearity at $\vec{x}_0$		
		Total	ΔP	Δh	Toal	ΔP	Δh
1	Before	12	12	12	7	3	7
	After	9	0	9	7	3	7
2	Before	21	19	21	3	2	3
	After	0	0	0	3	2	3
3	Before	2	2	2	5	5	5
	After	2	1	2	3	0	3
4	Before	0	0	0	1	1	1
	After	0	0	0	1	1	1

In summary, the diagnostics procedure helped 47 out of 51 originally non-converged cases reached convergence. Out of the 47 cases, 40 cases converged by changing the characterization methods in the evaporator. The comparison before and after the procedure shows that the simulation could still converge when the HX model was associated with nonlinearity. This suggests that simulation convergence has correlation with, but is not entirely constrained by component nonlinearity.

6.4. Summary

This Chapter proposed and tested two convergence improvement approaches on the basis of nonlinear equation fundamentals. The first approach was approximation-assisted global convergence with finite-volume local convergence. The second approach was initial guess screening with initial Jacobian condition number. A water-source chiller system was used as the test system to assess the efficacy of the two approaches. The main conclusions are as follows:

a. The success rate of the first approach was 38%, indicating that it did not lead to improvement as expected.
b. For the second approach, a small value of $\kappa(J_0)$ presents a convergence rate as high as 72%. On the other hand, a large $\kappa(J_0)$ presents low probability of final convergence. The smaller the $\kappa(J_0)$, the higher chance of successful convergence at the current initial guess point. However, initial guess screening based on $\kappa(J_0)$ alone is not enough, and other screening criteria may be needed.
c. Analysis and diagnostics of a non-converged case with a small value of $\kappa(J_0)$ suggests that the convergence failure may have a strong correlation with the nonlinear behaviors of the component models at the initial guess point.
d. A diagnostics procedure was applied and helped 47 out of 51 originally non-converged cases reach convergence. Out of the 47 cases, 40 cases converged by changing the characterization methods in the evaporator. However, the diagnostics results show that the simulation could still converge in the presence of HX model

nonlinearity. This suggests that simulation convergence is not entirely determined by component nonlinearity.

7. Conclusion, contribution and future work

7.1. Summary and conclusions

This dissertation fulfills three research objectives to advance the state of the art in steady-state simulation of vapor compression systems. The key conclusions from the current research are summarized as follows.

1. Flexibility: Developed and validated a novel solution methodology for arbitrary vapor compression cycles

- A generalized residual equation formulation methodology with a tripartite graph-based tearing algorithm was developed and implemented. The methodology was applied to 15 vapor compression systems and the resulting equations were verified for thermodynamic correctness. The solution approach was further validated by simulating four different test systems and comparing the predictions with measured data. These included residential and commercial air-conditioning and supermarket refrigeration systems, and used conventional as well as natural refrigerants, with capacities ranging from 10 to 100 kW. In the validation tests, the maximum simulation energy imbalance ($|\Delta_E|$) was 0.91%, and the maximum system performance deviation ($|\delta|$) was 8.94%.
- The solution methodology was also used to investigate two novel and proprietary vapor compression systems that are not yet commercialized. Across the two systems, 15 operating points were analyzed, followed by a parametric analysis to evaluate design sensitivities. This demonstrates the efficacy of the proposed methodology to accelerate early stage research and development.

2. Computational efficiency: Development of on-the-fly approximation-assisted component modeling

- Three approximation-assisted HX models were developed and compared for accuracy and computational speed. The Kriging metamodel was found to be the most accurate approximation model. The mean absolute errors in HX pressure drop (ΔP) and heat capacity prediction (Δh) were 4.46% and 0.9%, respectively. For system simulations, the highest deviations in COP and capacity of the Kriging metamodel were 2.54% and 1.45%, respectively.
- Simulations were sped up by a factor of 10 to 600 for a total of 8 test points for three different systems.
- The use of the approximation models also facilitates convergence by smoothing out the nonlinearities arising from the use of empirical correlations for heat transfer and pressure drop evaluation in the component models. Several cases that failed with finite-volume HX models could converge successfully with the approximation models.

3. Robustness: Developed a diagnostics framework to identify root cause for convergence failures and proposed improvement approaches

- Over 95 different initial conditions were analyzed for the solutions of a standard vapor compression-based commercial AC system. The analysis revealed that the condition number of Jacobian matrix was correlated to convergence failures. Higher the conditioner number, greater the chance of convergence failure for the given initial point.

- At the same time, it was observed for a certain number of cases that a well-conditioned Jacobian matrix also led to convergence failures. A systematic monotonicity analysis was used to trace this to mathematically non-smooth behavior of the component models that resulted from empirical heat transfer and pressure drop correlations.
- Two mitigation measures were proposed as follows: (i) modification of correlations used in component models, especially in heat exchangers, and (ii) leveraging on-the-fly approximation of component model performance. These aided 47 out of 51 non-converged cases to reach convergence, resulting in a 90% convergence improvement rate.

7.2. Contributions

The main contributions from this research are as follows:

1. Flexibility – A solution methodology using a tripartite graph-based tearing algorithm.

- Allows for the steady-state performance evaluation and design optimization of existing and novel vapor compression systems
- Facilitates the transition of the HVAC&R industry towards new lower-GWP refrigerants, paving the path for more sustainable heat pumping and refrigeration technology.
- Accelerates time to market, by providing a single platform for early stage R&D, detailed design and performance rating of vapor compression based air-conditioners, heat pumps and refrigeration systems.

2. Computational efficiency – An on-the-fly speed improvement methodology using component approximation.

- Achieved system simulation speedup of 10X – 600X, with a less than 3% penalty in solution accuracy.
- Substantial improvement in usability and stability of third-party component models; which in turn facilitates the widespread adoption of the proposed methodology as an industry standard.

3. Robustness – New insights into steady-state simulation convergence.

- Assisted end-users in identifying the root cause of simulation failures and proposing corrective measures, thereby improving simulation efficiency
- Laid the foundations for the next-generation multi-start and intelligent solvers that would proactively monitor convergence and require little to no user intervention to converge.

The related publications are listed as follows:

- **R. Huang**, J. Ling, V. Aute, “A component-based methodology for steady-state solution of generalized vapor compression systems with multiple operating modes,” *Applied Thermal Engineering (Under revision)*
- **R. Huang**, J. Ling, V. Aute, "Comparison of approximation-assisted heat exchanger models for steady-state simulation of vapor compression system," *Applied Thermal Engineering*, vol. 166, no. 5, p. 114691, 2020

- **R. Huang**, Z. Huang, J. Ling, V. Aute, "Simulation and optimization of water-based hybrid VRF systems with bifurcating bare-tube heat exchangers," in *25th IIR International Congress of Refrigeration*, Montreal, 2019
- Z. Huang, **R. Huang**, J. Ling, V. Aute, Y. Hwang, "Application of bifurcated bare-tube heat exchanger on water-based hybrid VRF System," in *17th International Refrigeration and Air Conditioning Conference*, West Lafayette, 2018.
- **R. Huang**, J. Ling, V. Aute, "Comparison of approximation-assisted component modeling methods for steady state vapor compression system simulation," in *17th International Refrigeration and Air Conditioning Conference*, West Lafayette, 2018.

7.3. Recommendation for future work

This dissertation aims to deliver effective solutions to the key aspects of the steady-state simulation technologies for vapor compression systems. The following features and directions would further advance the proposed simulation framework and increase its impact on the HVAC&R research and industry community.

1. Additional features that may be desired during the practice of the simulation framework.

- Characterizing the uncertainty propagation from the component model to the system results. For example, the selection of hydraulic and heat transfer correlations in the HXs are a major source of accuracy uncertainties. It would be helpful to understand how much of a 20% uncertainty in the refrigerant two-phase

correlation would eventually be propagated to system capacity, power consumption and other metrics for the system of interest.

- On-the-fly nonlinearity smoother of the component model. The current research shows that changing the pressure drop or heat transfer correlations in the HX models was effective to reach convergence. However, changing correlation might not always be a desirable option for the end user. Therefore, it would be helpful to provide localized approximation to smooth out the component nonlinearity around those numerical 'black holes' that would otherwise fail the entire iteration.

2. Future research directions enabled by the general-purpose steady-state solution approach

- Intelligent system design and optimization framework. The overall goal is to help find the optimal energy solution, given a set of objectives (maximum efficiency, minimum cost, minimum environmental impact, etc.) and constraints (material cost, emission, local climate, etc.). This may include two levels. On the manufacturer level, this framework can be used for integrated component sizing and optimization. On the building level, the framework can be used to determine the optimal system configuration, considering grid interaction, non-vapor compression alternatives, thermal storage options, etc.

References

[1] U.S. Energy Information Administration, "Table CE3.1 Annual household site end-use consumption in the U.S. - totals and averages, 2015," 2015. [Online]. Available: https://www.eia.gov/consumption/residential/data/2015/c&e/pdf/ce3.1.pdf.

[2] U.S. Energy Information Administration, "Table E1. Major fuel consumption (Btu) by end use, 2012," 2016. [Online]. Available: https://www.eia.gov/consumption/commercial/data/2012/c&e/pdf/e1.pdf.

[3] "United Nations framework convention on climate change, adoption of the Paris Agreement," United Nations, Paris, 2015.

[4] J. Winkler, V. Aute and R. Radermacher, "Comprehensive investigation of numerical methods in simulating a steady-state vapor compression system," *International Journal of Refrigeration,* vol. 31, no. 5, pp. 930-942, 2008.

[5] H. Jiang, V. Aute and R. Radermacher, "CoilDesigner: a general-purpose simulation and design tool for air-to-refrigerant heat exchangers," *International Journal of Refrigeration,* vol. 29, no. 4, pp. 601-610, 2006.

[6] H. Qiao, V. Aute, H. Lee, K. Saleh and R. Radermacher, "A new model for plate heat exchangers with generalized flow configurations and phase change," *International Journal of Refrigeration,* vol. 36, no. 2, pp. 622-632, 2013.

[7] V. Aute, "A review of state of the art in modeling of air-to-refrigerant heat exchangers for HVAC&R applications," in *International Refrigeration and Air Conditioning Conference*, West Lafayette, 2016.

[8] Z. Li, L. Shao and C. Zhang, "Fin-and-tube condenser performance modeling with neural network and response surface methodology," *International Journal of Refrigeration,* vol. 59, pp. 124-134, 2015.

[9] "Standard for performance rating of positive displacement refrigerant compressors and compressor units," AHRI, Arlington, 2015.

[10] X. Ding, W. Cai, L. Jia and W. Changyun, "Evaporator modeling–A hybrid approach," *Applied Energy,* vol. 86, no. 1, pp. 81-88, 2009.

[11] H. Qiao, R. Radermacher and V. Aute, "A review for numerical simulation of vapor compression systems," in *International Refrigeration and Air Conditioning Conference at Purdue,* Lafayette, 2010.

[12] P. Domanski and D. Didion, "Computer modeling of the vapor compression cycle with constant flow area expansion device," National Bureau of Standards, Washington, DC, 1983.

[13] S. Fischer and C. Rice, "Oak Ridge heat-pump models. I. A steady-state computer design model for air-to-air heat pumps," Oak Ridge National Lab, TN (USA), 1983.

[14] G. Ding, "Recent developments in simulation techniques for vapor-compression refrigeration systems," *International Journal of Refrigeration,* vol. 30, no. 7, pp. 1119-1133, 2007.

[15] P. Domanski and M. McLinden, "A simplified cycle simulation model for the performance rating of refrigerants and refrigerant mixtures," *International Journal of Refrigeration,* vol. 15, no. 2, pp. 81-88, 1992.

[16] M. de Lemos and E. Zaparoli, "Steady-state numerical solution of vapor compression refrigeration units," in *International Refrigeration and Air Conditioning Conference*, West Lafayette, 1996.

[17] Browne and Bansal, "Steady-state model of centrifugal liquid chillers," *International Journal of Refrigeration*, vol. 21, no. 5, pp. 343-358, 1999.

[18] D. Robinson and E. Groll, "Theoretical Pprformance comparison of CO2 transcritical cycle technology versus HCFC-22 technology for a military packaged air conditioner application," *HVAC&R Research*, vol. 6, no. 4, pp. 325-348, 2000.

[19] H. Jin and J. Spitler, "A parameter estimation based model of water-to-water heat pumps for use in energy calculation programs," in *ASHRAE Transactions*, Atlanta, 2002.

[20] P. Zhao, G. Ding, C. Zhang and L. Zhao, "Simulation of a geothermal heat pump with non-azeotropic mixture," *Applied Thermal Engineering*, vol. 23, no. 12, pp. 1515-1524, 2003.

[21] J. Sarkar, S. Bhattacharyya and R. Gopal, "Simulation of a transcritical CO2 heat pump cycle for simultaneous cooling and heating applications," *International Journal of Refrigeration*, vol. 29, no. 5, pp. 735-743, 2006.

[22] D. Blanco, K. Nagano and M. Morimoto, "Steady state vapor compression refrigeration cycle simulation for a monovalent inverter-driven water-to-water heat pump with a desuperheater for low energy houses," *International Journal of Refrigeration*, vol. 35, no. 7, pp. 1833-1847, 2012.

[23] J. Heo, R. Yun and Y. Kim, "Simulations on the performance of a vapor-injection heat pump for different cylinder volume ratios of a twin rotary compressor," *International Journal of Refrigeration*, vol. 36, no. 3, pp. 730-744, 2013.

[24] R. Sánta, L. Garbai and I. Fürstner, "Optimization of heat pump system," *Energy,* vol. 89, pp. 45-54, 2015.

[25] G. Zsembinszki, A. de Gracia, P. Moreno, R. Rovira, M. González and L. Cabeza, "A novel numerical methodology for modelling simple vapour compression refrigeration system," *Applied Thermal Engineering,* vol. 115, pp. 188-200, 2017.

[26] H. Sun, G. Ding, H. Hu, T. Ren, G. Xia and G. Wu, "A general simulation model for variable refrigerant flow multi-split air conditioning system based on graph theory," *International Journal of Refrigeration,* vol. 82, pp. 22-35, 2017.

[27] D. Richardson, "An object oriented simulation framework for steady-state analysis of vapor compression refrigeration systems and components. Ph.D. Dissertation," University of Maryland, College Park, 2006.

[28] S. Shao, W. Shi, X. Li and Q. Yan, "Simulation model for complex refrigeration systems based on two-phase fluid network–Part I: Model development," *International Journal of Refrigeration,* vol. 31, no. 3, pp. 490-499, 2008.

[29] T. Herbas, E. Berlinck, C. Uriu, R. Marques and J. Parise, "Steady-state simulation of vapour-compression heat pumps," *International Journal of Energy Research,* vol. 17, no. 9, pp. 801-816, 1993.

[30] T. Rossi, "Detection, diagnosis, and evaluation of faults in vapor compression equipment. Ph.D. Dissertation," Purdue University, West Lafayette, 1997.

[31] Y. Hwang and R. Radermacher, "Theoretical evaluation of carbon dioxide refrigeration cycle," *HVAC&R Research,* vol. 4, no. 3, pp. 245-263, 1998.

[32] J. Corberán, J. Gonzálvez, P. Montes and R. Blasco, "'ART' a computer code to assist the design of refrigeration and A/C equipment," in *International Refrigeration and Air Conditioning Conference,* West Lafayette, 2002.

[33] J. Winkler, "Development of a component based simulation tool for the steady state and transient analysis of vapor compression systems. Ph.D. Dissertation," University of Maryland, College Park, 2009.

[34] M. Beshr, "Steady state modeling and optimization for performance and environmental impact of advanced vapor compression systems. PhD. Dissertation," University of Maryland, College Park, 2016.

[35] M. Ruz, J. Garrido, F. Vázquez and F. Morilla, "A hybrid modeling approach for steady-state optimal operation of vapor compression refrigeration cycles," *Applied Thermal Engineering,* vol. 120, pp. 74-87, 2017.

[36] L. Zhang, Y. Jiang, J. Dong and Y. Yao, "Advances in vapor compression air source heat pump system in cold regions: A review," *Renewable and Sustainable Energy Reviews,* vol. 81, pp. 353-365, 2018.

[37] E. Torrella, J. Larumbe, R. Cabello, R. Llopis and D. Sanchez, "A general methodology for energy comparison of intermediate configurations in two-stage vapour compression refrigeration systems," *Energy,* vol. 36, no. 7, pp. 4119-4124, 2011.

[38] S. Jiang, S. Wang, X. Jin and T. Zhang, "A general model for two-stage vapor compression heat pump systems," *International Journal of Refrigeration,* vol. 51, pp. 88-102, 2015.

[39] S. Jiang, S. Wang, X. Jin and Y. Yu, "The role of optimum intermediate pressure in the design of two-stage vapor compression systems: A further investigation," *International Journal of Refrigeration,* vol. 70, pp. 57-70, 2016.

[40] G. Grossman and A. Zaltash, "ABSIM—modular simulation of advanced absorption systems," *International Journal of Refrigeration,* vol. 24, no. 6, pp. 531-543, 2001.

[41] B. Shen and C. Rice, "HVAC system optimization with a component based system model–new version of ORNL heat pump design model," Purdue HVAC/R Optimization short course, International Compressor & refrigeration conferences, Lafeyette, 2014.

[42] P. Domanski, J. Brown and E. Lemmon, "CYCLE_D: NIST vapor compression cycle design program, version 6.0; User's Guide," National Institute of Standards and Technology, Gaithersburg, 2018.

[43] D. Bruck, H. Elmqvist, H. Olsson and S. Mattsson, "Dymola for multi-engineering modeling and simmulation," in *2nd International Modelica Conference*, Oberpfaffenhofen, Germany, 2002.

[44] E. Carpanzano and C. Maffezzoni, "Symbolic manipulation techniques for model simplification in object-oriented modelling of large scale continuous systems," *Mathematics and Computers in Simulation,* vol. 48, no. 2, pp. 133-150, 1998.

[45] H. Elmqvist and M. Otter, "Methods for tearing systems of equations in object-oriented modeling," in *Proc. European Simulation Multiconference*, Barcelona, 1994.

[46] F. Cellier and H. Elmqvist, "Automated formula manipulation supports object-oriented continuous-system modeling," *IEEE Control Systems Magazine,* vol. 13, no. 2, pp. 28-38, 1993.

[47] R. Tarjan, "Depth first search and linear graph algorithms," *SIAM Journal on Computing,* vol. 1, no. 2, pp. 146-160, 1972.

[48] A. Baharev, H. Schichl and A. Neumaier, "Tearing systems of nonlinear equations I. $ A survey," University of Vienna, Vienna, 2016.

[49] A. Alabdulkarem, R. Eldeeb, Y. Hwang, V. Aute and R. Radermacher, "Testing, simulation and soft-optimization of R410A low-GWP alternatives in heat pump system," *International Journal of Refrigeration,* vol. 60, pp. 106-117, 2015.

[50] X. Wang, Y. Hwang and R. Radermacher, "Two-stage heat pump system with vapor-injected scroll compressor using R410A as a refrigerant," *International Journal of Refrigeration*, vol. 32, no. 6, pp. 1442-1451, 2009.

[51] J. Bush, M. Beshr, V. Aute and R. Radermacher, "Experimental evaluation of transcritical CO2 refrigeration with mechanical subcooling," *Science and Technology for the Built Environment,* vol. 23, no. 6, pp. 1013-1025, 2017.

[52] W. Dittus and K. Boelter, "Heat transfer in automobile radiators of the tubular type," *International Communications in Heat and Mass Transfer,* vol. 12, no. 1, pp. 3-22, 1985.

[53] D. Jung, M. McLinden, R. Radermacher and D. Didion, "A study of flow boiling heat transfer with refrigerant mixtures," *International Journal of Heat and Mass Transfer,* vol. 32, no. 9, pp. 1751-1764, 1989.

[54] C. Wang, Y. Tsai and D. Lu, "Comprehensive study of convex-louver and wavy fin-and-tube heat exchangers," *Journal of Thermophysics and Heat transfer,* vol. 12, no. 3, pp. 423-430, 1998.

[55] A. Cavallini, G. Censi, D. Del Col, L. Doretti, G. Longo, L. Rossetto and C. Zilio, "Condensation inside and outside smooth and enhanced tubes—a review of recent research," *International Journal of Refrigeration,* vol. 26, no. 4, pp. 373-392, 2003.

[56] V. Gnielinski, "New equations for heat and mass transfer in turbulent pipe and channel flow," *International Journal of Chemical Engineering,* vol. 16, no. 2, pp. 359-368, 1976.

[57] I.-K. Kim, J.-H. Park, Y.-H. Kwon and Y.-S. Kim, "Experimental study on R-410a evaporation heat transfer characteristics in oblong shell and plate heat exchanger," *Heat Transfer Engineering,* vol. 28, no. 7, pp. 633-639, 2007.

[58] H. Kumar, "The plate heat exchanger: construction and design," *Institute of Chemical Engineering Symposium Series,* vol. 86, pp. 1275-1288, 1984.

[59] M. Shah , "General correlation for heat transfer during condensation in plain tubes: further development and verification," *ASHRAE Transactions,* vol. 19, pp. 3-11, 2013.

[60] H. Kim, B. Youn and L. Webb, "Air-side heat transfer and friction correlations for plain fin-and-tube heat exchangers with staggered tube arrangements," *Journal of Heat Transfer,* vol. 121, no. 3, pp. 662-667, 1999.

[61] C. Wang, C. Lee, C. Chang and S. Lin, "Heat transfer and friction correlation for compact louvered fin-and-tube heat exchangers," *International journal of heat and mass transfer,* vol. 42, no. 11, pp. 1945-1956, 1999.

[62] D. Bacellar, V. Aute and R. Radermacher, "CFD-based correlation development for air side performance of finned and finless tube heat exchangers with small diameter tubes," in *International Refrigeration and Air Conditioning Conference at Purdue,* West Lafeyette, 2014.

[63] A. Muley and R. Manglik, "Experimental study of turbulent flow heat transfer and pressure drop in a plate heat exchanger with chevron plates," *Journal of Heat Transfer,* vol. 121, no. 1, pp. 110-117, 1999.

[64] Y. Yan, H. Lio and T. Lin, "Condensation heat transfer and pressure drop of refrigerant R-134a in a plate heat exchanger," *International Journal of Heat and Mass Transfer,* vol. 42, no. 6, pp. 993-1996, 1999.

[65] M. Schlager, B. Pate and E. Bergles, "Heat transfer and pressure drop during evaporation and condensation of R22 in horizontal micro-fin tubes," *International Journal of Refrigeration* , vol. 12, no. 1, pp. 6-14, 1989.

[66] M. Shah, "Comprehensive correlations for heat transfer during condensation in conventional and mini/micro channels in all orientations," *International journal of refrigeration,* vol. 67, pp. 22-41, 2016.

[67] S. Bhatti, "Turbulent and transition flow convective heat transfer in ducts," in *Handbook of Single-Phase Convective Heat Transfer*, Wiley, 1987.

[68] S. Jung and R. Radermacher, "Prediction of pressure drop during horizontal annular flow boiling of pure and mixed refrigerants," *International Journal of Heat and Mass Transfer,* vol. 32, no. 12, pp. 2435-2446, 19891.

[69] W. Churchill, "Friction factor equations spans all fluid-Flow regimes," *Chemical Engineering Journal,* vol. 84, pp. 91-92, 1977.

[70] L. Friedel, "Improved friction pressure drop correlation for horizontal and vertical two-phase pipe flow," in *European Two Phase Flow Group Meeting*, Ispra, Italy, 1979.

[71] R. Lockhart and R. Martinelli, "Proposed correlation of data for isothermal two-phase, two-component flow in pipes," *Chemical Engineering Progress,* vol. 45, no. 1, pp. 39-48, 1949.

[72] C. Wang, K. Chi and C. Chang, "Heat transfer and friction characteristics of plain fin-and-tube heat exchangers, part II: Correlation," *International Journal of Heat and mass transfer,* vol. 43, no. 15, pp. 2693-2700., 2000.

[73] P. Incropera and P. DeWitt, Introduction to heat transfer, 3rd ed., New York: John Wiley & Sons, 1996.

[74] S. Koyama, C. Kondou and K. Kuwahara, "An experimental study on condensation of CO2 in a horizontal micro-fin tube," in *International Conference of Refrigeration at Purdue*, West Lafeyette, 2008.

[75] M. Khan and M. Chyu, "Evaporation in flooded corrugated plate heat exchangers with ammonia and ammonia/miscible oil, RP-1352," in *American Society of Heating, Refrigerating and Air-Conditioning Engineers*, Atlanta, 2010.

[76] S. Koyamas and R. Yonemoto, "Experimental study on condensation of pure refrigerants in horizontal micro-fin tube–proposal of correlations for heat transfer coefficient and frictional pressure drop," in *International Conference of Refrigeration at Purdue*, West Lafeyette, 2006.

[77] X. Wang, "Performance investigation of two-stage heat pump system with vapor-injected scroll compressor (PhD Diss.)," University of Maryland, College Park, 2008.

[78] J. Dennis and R. Schnabel, Numerical methods for unconstrained optimization and nonlinear equations, SIAM, 1996.

[79] E. Lemmon, M. Huber and M. McLinden, "NIST Standard reference database 23: reference fluid thermodynamic and transport properties-REFPROP, Version 9.1, standard reference data program," National Institute of Standards and Technology, Gaithersburg, MD, 2015.

[80] V. Aute and R. Radermacher, "Standardized polynomials for fast evaluation of refrigerant thermophysical properties," in *International Refrigeration and Air Conditioning Conference at Purdue*, Lafeyette, 2014.

[81] "Performance rating of unitary air-conditioning & air-source heat pump equipment," AHRI, Arlington, 2017.

[82] R. Zhang, K. Sun, T. Hong, Y. Yura and R. Hinokuma, "A novel Variable Refrigerant Flow (VRF) heat recovery system model: Development and validation," *Energy and Buildings,* vol. 168, pp. 399-412, 2018.

[83] "Performance rating of commercial and industrial unitary air-conditioning condensing units," AHRI, Arlington, 2019.

[84] J. Sacks, W. Welch, T. Mitchell and H. Wynn, "Design and analysis of computer experiments," *Statistical Science,* vol. 4, no. 4, pp. 409-423, 1989.

[85] F. Viana, T. Simpson, V. Balabanov and V. Toropov, "Special section on multidisciplinary design optimization: metamodeling in multidisciplinary design optimization: how far have we really come?," *AIAA Journal,* vol. 52, no. 4, pp. 670-690, 2014.

[86] T. Simpson, J. Poplinski, P. Koch and J. Allen, "Metamodels for computer-based engineering design: survey and recommendations," *Engineering with Computers,* vol. 17, no. 2, pp. 129-150, 2001.

[87] O. Abdelaziz , V. Aute, S. Azarm and R. Radermacher, "Approximation-assisted optimization for novel compact heat exchanger designs," *HVAC&R Research,* vol. 16, no. 5, pp. 707-728, 2010.

[88] D. Bacellar, V. Aute, Z. Huang and R. Radermacher, "Design optimization and validation of high-performance heat exchangers using approximation assisted optimization and additive manufacturing," *Science and Technology for the Built Environment,* vol. 23, no. 6, pp. 896-911, 2017.

[89] M. Mohanraj, S. Jayaraj and C. Muraleedharan, "Applications of artificial neural networks for thermal analysis of heat exchangers – A review," *International Journal of Thermal Sciences,* vol. 90, pp. 150-172, 2015.

[90] M. Mohanraj, S. Jayaraj and C. Muraleedharan, "Applications of artificial neural networks for refrigeration, air-conditioning and heat pump systems—a review," *Renewable and Sustainable Energy Reviews,* vol. 16, no. 2, pp. 1340-1358, 2012.

[91] J. Wen, H. Yang, G. Jian, X. Tong, K. Li and S. Wang, "Energy and cost optimization of shell and tube heat exchanger with helical baffles using Kriging metamodel based on MOGA," *International Journal of heat and Mass transfer*, vol. 98, pp. 29-39, 2016.

[92] N. Li, S. Cheung, X. Li and J. Tu, "Multi-objective optimization of HVAC system using NSPSO and Kriging algorithms—A case study," *Building Simulation,* vol. 10, no. 5, pp. 769-781, 2017.

[93] A. Foucquier, S. Robert, F. Suard, L. Stéphan and A. Jay, "State of the art in building modelling and energy performances prediction: A review," *Renewable and Sustainable Energy Reviews,* vol. 23, pp. 272-288, 2013.

[94] G. Wang and S. Shan, "Review of metamodeling techniques in support of engineering design optimization," *Journal of Mechanical Design,* vol. 129, no. 4, pp. 370-380, 2007.

[95] A. Aijazi and L. Glicksman, "Comparison of regression techniques for surrogate models of building energy performance," in *Proceedings of SimBuild*, Salt Lake City, 2016.

[96] L. Bell, "ACHP component models: condenser," 2011. [Online]. Available: https://achp.readthedocs.io/en/latest/ACHPComponents/Condenser.html.

[97] H. Pangborn, A. Alleyne and N. Wu, "A comparison between finite volume and switched moving boundary approaches for dynamic vapor compression system modeling," *International Journal of Refrigeration,* vol. 53, pp. 101-114, 2015.

[98] L. Bell, S. Quoilin, E. Georges, J. Braun, E. Groll, H. Travis and V. Lemort, "A generalized moving-boundary algorithm to predict the heat transfer rate of counterflow heat exchangers for any phase configuration," *Applied Thermal Engineering,* vol. 79, pp. 192-201, 2015.

[99] H. Qiao, C. Laughman, V. Aute and R. Radermacher, "An advanced switching moving boundary heat exchanger model with pressure drop," *International Journal of Refrigeration,* vol. 65, pp. 154-171, 2016.

[100] R. Myers, D. Montgomery and C. Anderson-Cook, Response surface methodology: process and product optimization using designed experiments, John Wiley & Sons, 2016.

[101] M. McKay, R. Beckman and W. Conover, "Comparison of three methods for selecting values of input variables in the analysis of output from a computer code," *Technometrics,* vol. 21, no. 2, pp. 239-245, 1979.

[102] S. Lophaven, H. Nielsen, J. Sondergaard and A. Dace, "A matlab kriging toolbox," Technical University of Denmark, Kongens Lyngby, 2002.

[103] N. Cressie, "The origins of kriging," *Mathematical Geology,* vol. 22, no. 3, pp. 239-252, 1990.

[104] J. Martin and T. Simpson, "Use of kriging models to approximate deterministic computer models," *AIAA Journal,* vol. 43, no. 4, pp. 853-863, 2005.

[105] D. Jones, M. Schonlau and W. Welch, "Efficient global optimization of expensive black-box functions," *Journal of Global Optimization,* vol. 13, no. 4, pp. 455-492, 1998.

[106] R. Sibson, "A brief description of natural neighbour interpolation," in *Interpreting Multivariate Data,* John Wiley & Sons, 1981.

[107] A. Okabe, B. Boots, K. Sugihara and S. Chiu, Spatial tessellations: concepts and applications of Voronoi diagrams, John Wiley & Sons, 2009.

[108] L. Huang, V. Aute and R. Radermacher, "A finite volume coaxial heat exchanger model with moving boundaries and modifications to correlations for two-phase flow in fluted annuli," *International Journal of Refrigeration,* vol. 40, pp. 11-23, 2014.

[109] M. Shah, "A general correlation for heat transfer during film condensation inside pipes," *International Journal of Heat and Mass Transfer,* vol. 22, no. 4, pp. 547-556, 1979.

[110] "Methods of testing For rating seasonal efficiency of unitary air conditioners and heat pumps," ASHRAE, Atlanta, 2010.

[111] "Performance rating of water-chilling and heat pump water-heating packages using the vapor compression cycle," AHRI, Arlington, 2015.

[112] "Standard for water-source heat pumps," AHRI, Arlington, 1998.

[113] D. Bindel and J. Goodman, Principles of scientific computing, New York: New York University, 2009.